# Preparing for an Unbiased Study of the H $\rightarrow \gamma\gamma$ Background with the ATLAS Experiment at LHC

Lillian Smestad

Department of Physics

University of Oslo

Norway

Thesis presented for the Master of Science degree

in Experimental Particle Physics

December 2008

# Abstract

The Higgs mechanism is the best candidate theory for explaining how elementary particles obtain masses, but the Higgs boson predicted by this theory is as of today not observed. The H → $\gamma\gamma$ channel is one of the most promising decay channels for finding a light Higgs boson with the ATLAS detector at CERN. ATLAS is one of four detectors at the Large Hadron Collider. In this thesis, a study of this channel with emphasis on a background study has been made using full simulation. A search for a signal-free area has been made, in order to study the background without being disturbed or biased by the signal. A test was carried through of whether the invariant mass distribution of the signal and/or the background was distorted by the choice of region in the parameter plane of the missing transverse momentum versus non-planarity of the $\gamma\gamma$-pair. The ideal case, what is desired, is that the signal and background distributions remain unaffected by the choice of parameter regions. Testing this, fits of the signal alone using a Gaussian description and a fit of the background alone using an exponential description have been made. In addition, a combined fit of the signal and the irreducible background together has been made using three combinations of a polynomial or exponential description of the background together with a Gaussian or Crystal Ball description of the signal.

## Acknowledgements

I want to give warm thanks to my supervisor Alex Read for his great support, guidance and good words. Throughout this process I have been proud to state that he has been my supervisor. Bjørn Hallvard Samset deserves all the thanks I can give, for his priceless, endless help, for always cheering me on and brightening my view. I also want to thank him for boosting the musical side of me, giving me musical inspiration and input. I count myself lucky to have had Håvard Gjersdal, Eirik Gramstad, Gunn Kristine Elisabeth Holst Larsen and Maiken Pedersen as my fellow (or semi-fellow) Master students. All their extensive help has been invaluable, their good mood catching and the atmosphere they have created unique. I also want to thank the EPF group as a whole for the great environment, jokes and discussions and for giving me the possibility to go to CERN, which has proven to be very important for my understanding and feeling (dare I say love?) for the field of experimental particle physics. I have loved being a part of this group. Last, but not least, a praise to my family and friends, my loved ones, for supporting me throughout this process, always being there in times of despair and resignation, always being prepared to take my mind off the world of particle physics when I needed it[1].

---

[1] Above all this I would like to thank my sister, Bente - the best sister in the world - for spell checking my acknowledgements. Without her this Master thesis would not have been finished and would not have become the success it is. I love her and dedicate this whole piece of Nobel prize worthy work to her. In addition she is modest, shy and never exaggerates... [Editorial note; internal joke].

# Contents

# Chapter 1

# Introduction

There is a problem; we do not know why elementary particles have mass. From measurements we know that they do *have* mass, but we do not know *why* - this needs to be accounted for in some way. There are different ways of explaining this phenomenon of mass - one way (and the only one we will go more into detail on in this thesis) is through the Higgs mechanism, which will be described in Chapter 2. One alternative way of generating mass for elementary particles is through technicolor, see Section 2.3.2 for a crude description of this mechanism.

The Higgs mechanism is an integral part of the Standard Model (often abbreviated SM). More details on the Standard Model can be found in Chapter 2. The only particle included in the SM which is not yet discovered is the Higgs boson, and the only free (that is to say undetermined) parameter left in the SM is the Higgs boson mass. What we want to do, is of course to find the Higgs boson, to confirm whether this is the right way of describing the mechanism of mass. There are many different ways to achieve this, assuming that the Higgs boson exists at all, all depending on its mass. In this thesis, we will have a closer look at a search for the Higgs boson through the channel $H \rightarrow \gamma\gamma$, which is one of the most promising decay channels for finding a light Higgs boson. The conditions for this analysis are determined by the initial 10 TeV proton-proton collisions, followed by the full 14 TeV proton-proton collisions, taking place at the Large Hadron Collider (LHC), using the ATLAS detector. A brief overview of the LHC and the ATLAS detector is given in Chapter 3.

What will be done, is to make an analysis based on a study of Monte Carlo (from now on abbreviated MC) simulations of the signal and background, taking the detector into account, including even effects like mis-alignment and all material (such as for instance cryostat material, cables and services in addition to the detecting elements). A brief description of the full chain of physics event[1] generation through the detector simulation and subsequent reconstruction as well as an overview over the datasets used in this analysis can be seen in Chapter 5. A full simulation of the detector for all processes has been used in this analysis, whereas in the analysis done in the so-called ATLAS CSC (Computing System Commissioning) note [1], the background was generated using a fast simulation for the detector description. The effects of pile-up[2] and the

---

[1] An event is what happens in the detector as a result of one bunch-crossing of protons.

[2] The term pile-up is used for signals in our detector coming from a different bunch-crossing than the one of interest (things really belonging to a different event) as well as multiple minimum bias events in the same bunch crossing.

spread and displacement of the vertex are not included, neither in this thesis nor in the CSC note. See Chapter 6 for more information on the analysis performed.

The plan was to try to use the same analysis code on the first, real data taken with the ATLAS detector (this would have been collisions at a low luminosity, so it would only be a study of the background) but as there was an accident, causing the data-taking at LHC to be delayed beyond the deadline of this thesis, this was impossible to carry out [2].

A search for a signal free area in the background (see Chapter 4 for more details on the background) will be performed, as to be unbiased from the signal during background studies, in order not to depend on that the MC simulations are perfect (this defines a data driven analysis). This is something which is not mentioned in the CSC note [1] and will be a sort of guideline for this thesis. We will have a look at some key variables with different masses of the Higgs boson, to check whether these variables are independent of the mass of the Higgs boson - which would help us in the search of a signal free area in the background. We will also reconstruct an invariant mass plot from simulated Higgs data and make a fit of this and part of the background, and investigate whether a choice of the background parameterization influences the fit to the signal.

The results found in the CSC note state an expected significance of 2.6 (4.6) with 10 (30) fb$^{-1}$ of data, using the $H \rightarrow \gamma\gamma$ channel for the ATLAS detector and an inclusive analysis[3] [1]. The variable "significance" is used to give a measure of how sure one is that the observed deviations (from what was expected had there been no new physics) are not due to statistical fluctuations. A significance of $\sigma \sim 3$ gives the status of "evidence" and a significance of $\sigma \sim 5$ gives the status of "discovery". At full design luminosity, that is $1.0 \cdot 10^{34}$cm$^2$s$^{-1}$ one expects somewhere between 80 fb$^{-1}$ and 120 fb$^{-1}$ per year (all depending on the time it takes to inject and ramp up the beam) [3]. Before the accident occurred, it was expected that the LHC would run with 5 TeV beams in 2008, train for 7 TeV early 2009, and run first with a bunch gap of 75 ns in mid 2009, then with a 25 ns bunch gap towards the end of 2009. The design luminosity was expected to be reached after three years of running, that is to say in 2012, by which time a total integrated luminosity of 48 fb$^{-1}$ of data was expected to be collected [4]. All in all, this would mean that we would not expect to have good enough statistics to state a discovery before approximately two and a half years had passed. Now, the plans for the year 2009 are still not settled, the discussion whether to start at 10 TeV, or go straight to 14 TeV collisions, is still on-going.

It is possible to separate the analysis into different regions (which could be called categories) according to pseudorapidity, $\eta$ - different regions of pseudorapidity in the detector have different resolution on the diphoton invariant mass, $m_{\gamma\gamma}$, so a division of this kind leads to a higher sensitivity to the result (in this way, one does not mix broad and narrow peaks together). This approach has been used in the CSC note [1]. As there was no time to perform this kind of separation of pseudorapidity regions, it will not be included in this thesis. The author is fully aware that this could be done better. It is also not a goal of this thesis to improve the way the $\gamma\gamma$ pair is selected. See Chapter 4 for more information on the selection of the two photons which will be used.

Finally, the conclusions will be made in Chapter 7.

---

[3] An inclusive analysis means that you do not limit through which mechanism your Higgs boson was created.

# Chapter 2

# Theory

In this chapter, an introduction to the so-called Standard Model of particle physics will be made, together with a closer look at the Higgs mechanism. Some of the theories describing physics not included in the Standard Model, so-called beyond Standard Model physics, will be mentioned. Some of the more important production mechanisms of the Higgs boson at the LHC as well as the experimental limit on the mass of the Higgs boson will also be discussed.

## 2.1 The Standard Model

The Standard Model (from now on abbreviated SM) is a successful, although not complete, description of the nature of elementary particles, which is expected to be an effective theory, that means that it is valid up to a certain energy, but will break down at smaller distances (which is equivalent to higher energies) [5]. It contains the smallest constituents of matter that have been seen and three of the four known forces (the SM does not include gravity), and how they relate to each other. The Standard Model is based on relativistic quantum field theory.

The term 'relativistic' means that the speeds described by the theory are close to the speed of light, c[1], so a relativistic representation of the equations has to be used, in order to prevent them from depending on the frame of reference. 'Quantum' means that the different states are quantized, that is to say there is not a continuous transition between the different physical states the particles can be in, a transition from one state to another is carried through sudden jumps[2]. A world built up in this way is something we as humans have poor intuition for - in the macroscopic world we live in, things are mostly taking place continuously[3]. The word 'field' points to the fact that the system of particles and their quantization is taken to a continuous system, that is a field [6], which is to say an infinite collection of wave functions, permeating all of space [7], and, finally, 'theory' to the fact that, well - it is a theory.

---

[1] $c \approx 3.0 \cdot 10^8 m/s$, but in particle physics the convention is to use units of c=1, which also will be used throughout this thesis.

[2] So called quantum leaps.

[3] For instance, to imagine that your friend could either be at work or at the pub, but never anywhere in between, is something we cannot really relate to.

Lorentz invariant quantities have a very central role in relativistic quantum field theory - that is quantities that do not change under ’rotations’ in space-time (this is equivalent to the Lorentz transformations of special relativity; rotations, boosts[4] or a combination of these) [7]. Equations of these properties we can handily write using four-vectors - vectors including a time component in addition to three space components.

In the SM there are twelve matter particles, which have spin-$\frac{1}{2}$ and are thus fermions. These are the six quarks - up and down, charm and strange, top and bottom - and the six leptons - the electron, the muon and the tau, and their respective neutrinos. These fermions are placed in generations of families, ranging from one to three, after the time of their discovery, and their characteristics. As an example, the up- and down quark, the electron and the electron-neutrino are all members of generation one. All the fermions also have a sibling in the Standard Model - the anti-fermions, which mainly differ from the fermions through the fact that they have the opposite electric charge of their respective fermion (for instance $Q/|e|_d = -\frac{1}{3}, Q/|e|_{\bar{d}} = \frac{1}{3}$). The anti-quarks and anti-neutrinos are indicated by writing a bar over them, for instance $\bar{d}$ and $\bar{\nu}_\tau$. For the charged leptons, it is normal to indicate the antiparticles by their electric charge: $e^+, \mu^+, \tau^+$.

The electric charges of the up-type quarks are $+\frac{2}{3}$ and the electric charges of the down-type quarks are $-\frac{1}{3}$. The electric charges of the up-type leptons are -1 and the electric charges of the down-type leptons (the neutrinos) are zero. The particles having electric charge feel the electromagnetic force (interact with the photon) - this means all fermions except the neutrinos. The quarks, which are affected by the strong force, have color charge - each quark can have the color red, green or blue[5]. The charges corresponding to the weak force (the weak charges) are weak isospin $I_3^W$ (the third component of weak isospin $I^W$) and weak hypercharge $Y^W$. All of the fermions interact with the weak bosons. See Table 2.1 as well as Table 2.2 for some of the properties and quantum numbers of the fermions in the Standard Model and Figure 2.2 for an overview of the interactions between the particles of the SM[6].

When it comes to the force particles in the SM, they are the photon, $\gamma$, representing the electromagnetic force, the gluon, $g$, the strong force, the $W^+, W^-, Z$-bosons the weak force. Gravitation is not included in the Standard Model, as a renormalizable[7] quantum field theory of this is not yet found, since the graviton (the quantum of the gravitational field) has spin two [5].

The gluons carry color charge, the W± carries both weak isospin and electric charge, whereas the $Z^0$ boson does not carry any of the mentioned charges. However, the $Z^0$ boson does have weak isospin (although $I_3^W$=0), being in a weak isospin triplet with $W^+$ and $W^-$, which makes it able to interact with particles carrying weak isospin. The gluons and the weak bosons all belong to non-abelian groups ($SU(3)_C$ and $SU(2)_L$ respectively) and can therefore in principle interact with themselves, but in order for them to do this, they need to carry the charge of the force they

---

[4] Transformation to a frame with parallel axes, but moving in an arbitrary direction [8]

[5] This ’color’ has nothing to do with real-life color, it is just a set of quantum numbers. The names of the colors are chosen merely due to convention. These colors are experimentally indistinguishable. A state with all three colors (baryons) can be considered colorless, or "white", the same goes for a state with color and anti-color (mesons).

[6] This figure, found on http://en.wikipedia.org/wiki/Standard_Model, was altered due to a comment the author sent in about that the W self-coupling was missing.

[7] In a renormalizable theory you can calculate whatever you want, without having to include new constants for every higher-order correction included.

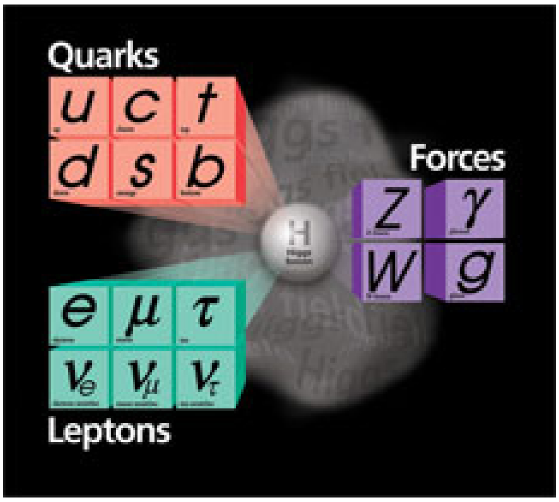

Figure 2.1: A sketch of the constituents of the Standard Model [from Fermilab].

represent. Therefore, all of these bosons interact with themselves, except for the Z$^0$ boson (Z$^0$ couple to the other weak bosons, only not with itself, due to the fact that it has $I_3$=0 and $Y^W$=0). Finally, the photon carries no charge at all, and so it cannot interact with itself, not having the charge of the force it represents, and belonging to the abelian group $U(1)$. See Table 2.1 for quantum numbers of the bosons and Figure 2.2 for a sketch over which particles of the SM interact with each other.

See Figure 2.1 for a overview of the constituents of the Standard Model. The fermions are placed to the left with the quarks in red on top and the leptons in green on the bottom, and they are all grouped in columns according to their generation. The force carriers, the gauge bosons, are placed in purple to the right, and the Higgs ghost field is sketched as a fog in the back, giving matter to some of the constituents of the SM. Please note that the spin-0 Higgs boson, although included in this figure, is not yet observed.

See Table 2.1 for the constituents of the SM and some of their quantum numbers.

| Type | Name | Mass [GeV] | Spin | $Q/\|e\|$ | Color charge | $Y^W$ | $I_3^W$ |
|---|---|---|---|---|---|---|---|
| Quark | u, c, t | $1.9{\cdot}10^{-3}$, 1.32, 173 | 1/2 | +2/3 | yes | See Table 2.2 | |
| | d, s, b | $4.4{\cdot}10^{-3}$, 0.087, 4.24 | 1/2 | -1/3 | yes | | |
| Lepton | $e^-, \mu^-, \tau^-$ | $5.11{\cdot}10^{-4}$, 0.106, 1.78 | 1/2 | -1 | no | See Table 2.2 | |
| | $\nu_e, \nu_\mu, \nu_\tau$ | all $\approx 0$ | 1/2 | 0 | no | | |
| Boson | $\gamma$ | 0 | 1 | 0 | no | 0 | 0 |
| | $W^+, W^-, Z^0$ | 80.4, 80.4, 91.2 | 1 | +1, -1, 0 | no | 0 | +1,-1,0 |
| | $g_i, i = 1, 8$ | 0 | 1 | 0 | yes | 0 | 0 |
| | $H^0$ | unknown | 0 | 0 | no | +1 | -1/2 |

Table 2.1: Elementary particles of the Standard Model, and some of their quantum numbers. $Q$ is electric charge, $Y^W$ and $I_3^W$ are weak hypercharge and third component of weak isospin as given in equation 2.1.

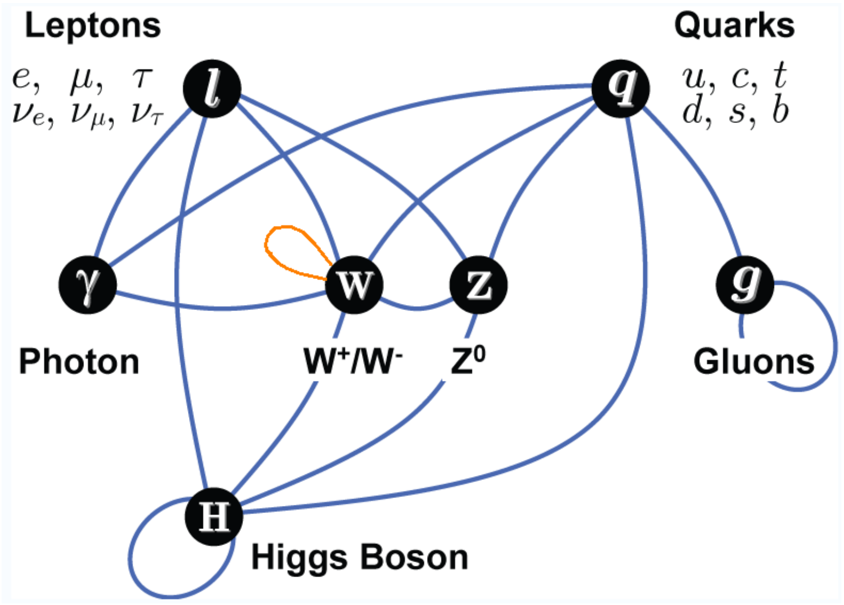

Figure 2.2: A sketch of the interactions between the particles of the Standard Model [from Wikipedia]. W self-coupling (orange) added by author.

| *Helicity* | *Generation* 1. | 2. | 3. | $Q/\lvert e\rvert$ | $I_3^W$ | $Y^W$ |
|---|---|---|---|---|---|---|
| $L$ | $\begin{pmatrix} \nu_e \\ e^- \end{pmatrix}_L$ | $\begin{pmatrix} \nu_\mu \\ \mu^- \end{pmatrix}_L$ | $\begin{pmatrix} \nu_\tau \\ \tau^- \end{pmatrix}_L$ | $0$<br>$-1$ | $\frac{1}{2}$<br>$-\frac{1}{2}$ | $-1$<br>$-1$ |
| | $\begin{pmatrix} u \\ d' \end{pmatrix}_L$ | $\begin{pmatrix} c \\ s' \end{pmatrix}_L$ | $\begin{pmatrix} t \\ b' \end{pmatrix}_L$ | $\frac{2}{3}$<br>$-\frac{1}{3}$ | $\frac{1}{2}$<br>$-\frac{1}{2}$ | $\frac{1}{3}$<br>$-\frac{1}{3}$ |
| $R$ | $e_R$ | $\mu_R$ | $\tau_R$ | $-1$ | $0$ | $-2$ |
| | $u_R$ | $c_R$ | $t_R$ | $\frac{2}{3}$ | $0$ | $\frac{4}{3}$ |
| | $d_R$ | $s_R$ | $b_R$ | $-\frac{1}{3}$ | $0$ | $-\frac{2}{3}$ |

Table 2.2: The three generations of fermions in the standard model. The left handed (L) particles are grouped in weak isospin doublets and the right handed ones (R) are isosinglets of weak isospin $I^W$. The quantum numbers $Q$, $I_3^W$ and $Y^W$ are respectively the electric charge, the third component of weak isospin and the weak hypercharge. Please note that no right-handed neutrinos (singlets) are included as this is not part of the (minimal) Standard Model (right-handed neutrinos will exist when the neutrinos have mass).

|  | $B$ | $C$ | $S$ | $T$ | $B^*$ | $Q/\|e\|$ | $Y^S$ | $I_3^S$ |
|---|---|---|---|---|---|---|---|---|
| u | 1/3 | 0 | 0 | 0 | 0 | 2/3 | 1/3 | 1/2 |
| d | 1/3 | 0 | 0 | 0 | 0 | -1/3 | 1/3 | -1/2 |
| c | 1/3 | 1 | 0 | 0 | 0 | 2/3 | 4/3 | 0 |
| s | 1/3 | 0 | -1 | 0 | 0 | -1/3 | 4/3 | 0 |
| t | 1/3 | 0 | 0 | 1 | 0 | 2/3 | 4/3 | 0 |
| b | 1/3 | 0 | 0 | 0 | -1 | -1/3 | 4/3 | 0 |

Table 2.3: Overview of the quarks of the SM and the quantum numbers baryon number $B$, strangeness $S$, charm $C$, topness $T$, bottomness $B^*$, strong hypercharge and third component of strong isospin.

The SM is of the gauge group $SU(3)_C \times SU(2)_L \times U(1)_Y$, where "$C$" stands for color, "$L$" indicates that only left-handed (see footnote number 15 in this chapter) fermions carry this quantum number and "$Y$" refers to the weak hypercharge $Y^W$ - which is connected to electric charge $Q$ and third component of weak isospin $I_3^W$ in this manner [9]:

$$\frac{Q}{|e|} = I_3^W + \frac{Y^W}{2}\,. \tag{2.1}$$

There is also a strong hypercharge, $Y^S$, only valid for quarks, which is linked to to electric charge $Q$ and third component of strong isospin $I_3^S$ and also baryon number $B$, strangeness $S$, charm $C$, bottomness $B^*$ and topness $T$ in this manner [10]:

$$\frac{Q}{|e|} = I_3^S + \frac{Y^S}{2} \tag{2.2}$$

$$Y^S = B + S + C + B^* + T\,. \tag{2.3}$$

Keep in mind that the up and down quarks are the only ones having third component of strong isospin, $I_3^S$, because strong isospin is defined from the nucleons, and the up and the down quarks are the only quarks "firmly" (ignoring the sea of quarks) sitting in the nucleons. See Table 2.3 for a overview of the quarks and these quantum numbers. The strong hypercharge is seen to be conserved under strong interactions, in contrast to weak hypercharge, which can be altered in certain weak interactions.

The Lagrangian of the SM tells us how the dynamics of the theory is - how the particles move in 4-space, what kind of interactions they have. It is built up as follows, listing only the main components (leaving out three and four boson vertices) [9, 11, 12, 13]:

$$\mathcal{L}_{\text{SM}} = \mathcal{L}_{\text{matter}} + \mathcal{L}_{\text{gauge}} + \mathcal{L}_{\text{Higgs}} + \mathcal{L}_{\text{Yukawa}} + \cdots$$

The matter Lagrangian, $\mathcal{L}_{\text{matter}}$, describes the interactions of fermions and gauge bosons;

$$\mathcal{L}_{\text{matter}} = i \sum_{j=1}^{3} \bar{\psi}^j \gamma^\mu D_\mu \psi_j\,,$$

where $\psi_j$ are the spinors describing the matter doublets, $j$ runs over the three generations, the gamma matrices $\gamma^\mu$ (most commonly written in the Pauli-Dirac representation, as a function of the Pauli matrices, see under) satisfy the anticommutation relations

$$[\gamma^\mu, \gamma^\nu]_+ = 2g^{\mu\nu},$$

$g^{\mu\nu}$ being the Minkowski matrix. The covariant derivative $D_\mu$ is given by

$$D_\mu = \partial_\mu - igW^a_\mu \frac{\tau^a}{2} - ig' B_\mu \frac{Y^W}{2} \ ,$$

where $\tau^a$ with $a = \{1, 2, 3\}$ denotes the 2×2 Pauli matrices

$$\tau^1 = \begin{pmatrix} 0 & 1 \\ 1 & 0 \end{pmatrix} \qquad \tau^2 = \begin{pmatrix} 0 & -i \\ i & 0 \end{pmatrix} \qquad \tau^3 = \begin{pmatrix} 1 & 0 \\ 0 & -1 \end{pmatrix} .$$

The couplings $g$ and $g'$ give the mixing angle $tan\theta_w = \frac{g'}{g}$. $W_\mu$ and $B_\mu$ are the fields containing the gauge bosons $W^\pm, Z$ and $\gamma$ (the two latter are the true matter eigenstates we observe; they come from a mixing of $B_\mu$ and the neutral component of $W_\mu$ with mixing angle $\theta_w$). $Y^W$ is weak hypercharge, as given in equation 2.1.

The gauge Lagrangian, $\mathcal{L}_{\text{gauge}}$, contains the kinetic part of the gauge bosons, as well as the interaction of the (mixed) gauge fields themselves;

$$\mathcal{L}_{\text{gauge}} = -\frac{1}{4} W^a_{\mu\nu} W^{a,\mu\nu} - \frac{1}{4} B_{\mu\nu} B^{\mu\nu} \ ,$$

where the field tensors are given by

$$W^a_{\mu\nu} = \partial_\mu W^a_\nu - \partial_\nu W^a_\mu - g\epsilon^{abc} W^b_{\mu\nu} W^c_\nu$$

$$B_{\mu\nu} = \partial_\mu B_\nu - \partial_\nu B_\mu \ ,$$

where $\epsilon^{abc}$ are the structure constants of the $SU(2)_L$ group (giving $+$ if the indices are in a cyclic order, $-$ if not).

The contribution from the Higgs field is given by

$$\mathcal{L}_{\text{Higgs}} = (D^\mu \phi)^\dagger (D_\mu \phi) - V(\phi^\dagger \phi) \ ,$$

where the potential V is given in Equation 2.14.

The last term, $\mathcal{L}_{\text{Yukawa}}$, gives mass to the fermions through the interactions between the Higgs field (the complex doublet $\phi$) and the fermions:

$$\mathcal{L}_{\text{Yukawa}} = \sum_{i=1}^{3} (f^l_i \bar{l}_{iL} \phi e_{iR} + f^u_i \bar{q}_{iL} \tilde{\phi} u_{iR} + f^d_i \bar{q}_{iL} \phi d_{iR}) \ , \tag{2.4}$$

where $f$ are the Yukawa couplings and it is again summed over number of generations through $i$. Note that the neutrinos are not given mass here.

## 2.2 The Higgs Mechanism

So, there is the problem - what is really the reason for the mass of the elementary particles? Peter W. Higgs was a smart guy who proposed a solution to this problem through his article in 1964 [14] (well, really, F. Englert and R. Brout [15] as well as G. S. Guralnik, C. R. Hagen, and T. W. B. Kibble [16] also wrote articles on the same topic the same year). This solution had its basis in spontaneous symmetry breaking, which will be explained in Section 2.2.1.

To explain the Higgs field in a populistic matter we can use the analogy proposed by David Miller (University College London) which is illustrated in Figure 2.3;

Picture a very crowded room, full of people. If a famous person enters the room, the people near him or her will gather around, eager to get a glimpse of him or her, or a chance to indulge in a conversation with the celebrity. The famous person will then have a hard time trying to cross the room, he or she will be slowed down by the eager crowd. We can say that he or she gains mass. This is the way fermions are thought to become massive, travelling through the Higgs field (all the people filling up the room) permeating all space.

Another thought experiment of the same analogy will be that no famous person enters the room, but a rumor of that a celebrity soon will do so spreads out. The persons talking about this rumor will gather together to a higher density around the rumor than elsewhere in the room. This analogy represents the Higgs boson itself [17].

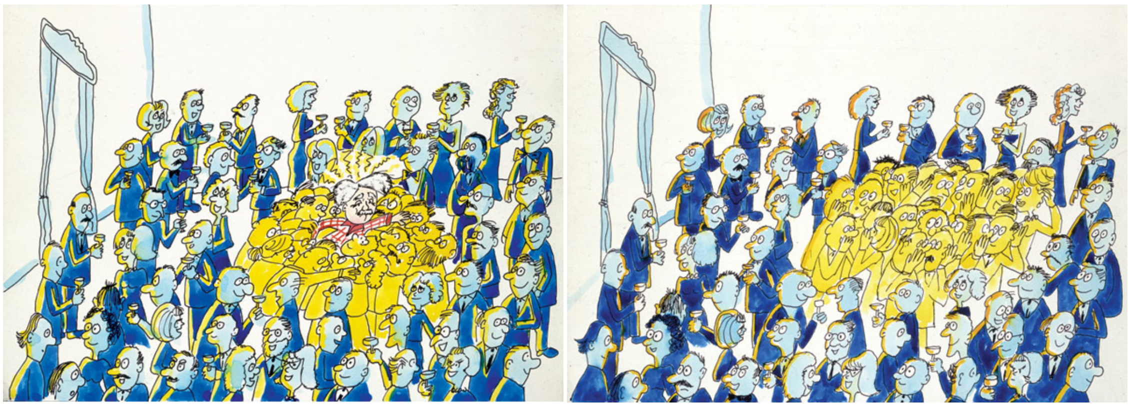

Figure 2.3: Analogy for the Higgs field. To the left; the analogy of how fermions gain mass. To the right; the analogy of the Higgs boson itself [from Nature 448, 297-301].

As mentioned in Section 2.1, the masses of the fermions are due to the Yukawa couplings to the Higgs field (which are parameters of the SM). In the strict view of the SM (called the minimal SM), there are no right-handed neutrinos, or left-handed anti-neutrinos. As a consequence, the simple Higgs mechanism cannot give mass to the neutrinos. In this case, the SM has 19 parameters. There are persistent indirect indications of neutrino masses, so the minimal SM seems not to be sufficient [5].

15 of the parameters of the Standard Model come from the part of the Lagrangian having to do with the Higgs field (ten masses, the Higgs self-coupling and four Kobayashi-Maskawa angles) [9]. In this way, we can say that $\mathcal{L}_{\text{Higgs}}$ contains most of our lack of knowledge and is the part of the theory which is least understood.

It is good to have this simplified picture to grasp the concept, but what does this mean in terms of physics and hard equations? Let us have a look at this now[8].

### 2.2.1 Spontaneous Symmetry Breaking

In order to keep the SM theory renormalizable (i.e calculable) while introducing mass terms, a mechanism that retains the gauge invariance of the Lagrangian is needed. It is not an option to simply add mass terms by brute force, since this will break symmetries that need to be fulfilled. If we add a mass term for the weak bosons, $\frac{1}{2}M_V^2 W_\mu W^\mu$ ($V$ indicating the mass of the vector boson), the $SU(2) \times U(1)$ symmetry is violated. This can be illustrated by the case of the photon, where adding a mass term leads to that the $U(1)$ symmetry is broken (see next section for information on the $U(1)$ symmetry):

$$\frac{1}{2}M_A^2 A_\mu A^\mu \to \frac{1}{2}M_A^2 \left[A_\mu + \partial_\mu \theta(x)\right] \left[A^\mu + \partial^\mu \theta(x)\right] \neq \frac{1}{2}M_A^2 A_\mu A^\mu. \tag{2.5}$$

One mechanism that can introduce mass terms without breaking the gauge invariance of the theory is spontaneous symmetry breaking.

Spontaneous symmetry breaking can only occur when the state of the lowest energy of a system, the ground state, is not unique, but degenerate. Then there is no state alone that can fully describe the ground state of the system. To describe the ground state, the whole “sum” of all states making the ground state is needed. If one of the states is chosen to represent the ground state, the symmetry is spontaneously broken. This is because this one state that has been chosen does not have the symmetry transformations that the Lagrangian of the system has. This spontaneous symmetry breaking is not dependent on which state is chosen, but the mere act of choosing one state above the others.

To get a more tangible picture of the spontaneous symmetry breaking, one can imagine a pencil balancing on its tip, and suddenly falling in one arbitrary direction. Before it fell, it could turn around the axis running through the middle of it orthogonal to the table, and we could not have told the difference. But after it has fallen, this is no longer the case. The symmetry is broken.

In field theory, the vacuum is the ground state of a system. Thus, for spontaneous symmetry breaking to take place, we need a vacuum expectation value that is non-zero (the ground state would not have been degenerate, had it been zero). This is expressed in the equation

$$< 0|\phi(x)|0 >= c \neq 0 \;, \tag{2.6}$$

---

[8] The three following subsections are mainly based on Chapter 13 in [6].

where $\phi(x)$ is a scalar field and c is a constant.

We will now use the Higgs Model to explain more about the mechanism of spontaneous symmetry breaking.

### 2.2.2 The Higgs Model

In this section, the Higgs mechanism for the case of the photon field is illustrated, where the photon becomes massive through the mechanism of spontaneous symmetry breaking. It is only included as a study of the effect of the Higgs mechanism, shown in the easiest scenario (only having one force field - that of the photon). As we end up with a massive photon, this model does not represent nature.

In the Higgs Model, a field $\phi(x)$ which exhibits spontaneous symmetry breaking is introduced. In addition to this complex scalar field $\phi(x)$,

$$\phi(x) = \frac{1}{\sqrt{2}}\{\phi_1(x) + i\phi_2(x)\}\ , \tag{2.7}$$

we add another free gauge field $A_\mu$ - the electromagnetic field.

The Lagrangian density is then given by

$$\mathcal{L} = [D^\mu\phi(x)]^*[D_\mu\phi(x)] - \mu^2|\phi(x)|^2 - \lambda|\phi(x)|^4 - \frac{1}{4}F_{\mu\nu}(x)F^{\mu\nu}(x)\ , \tag{2.8}$$

where $\mu^2$ and $\lambda$ are real parameters and $D_\mu$ is the covariant derivative

$$D_\mu = \partial_\mu + ieA_\mu(x). \tag{2.9}$$

The last term in (2.8) is the Lagrangian density of the free gauge field $A_\mu(x)$, where

$$F_{\mu\nu}(x) = \partial_\nu A_\mu(x) - \partial_\mu A_\nu(x). \tag{2.10}$$

This Lagrangian is invariant under $U(1)$ gauge transformations, i.e we have the transformations

$$\phi(x) \to \phi(x)' = \phi(x)e^{-ie\theta(x)}\ , \tag{2.11}$$

$$\phi^*(x) \to \phi^*(x)' = \phi^*(x)e^{ie\theta(x)}\ , \tag{2.12}$$

$$A_\mu \to A'_\mu = A_\mu + \partial_\mu\theta(x). \tag{2.13}$$

This is the symmetry which will be spontaneously broken.

The potential energy density of the field $\phi(x)$ is

$$V(\phi(x)) = \mu^2|\phi(x)|^2 + \lambda|\phi(x)|^4. \tag{2.14}$$

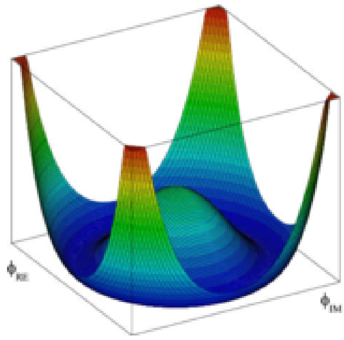

Figure 2.4: The Higgs potential, as a function of $\phi_1(x)$ and $\phi_2(x)$. Note the circle of minimum potential energy [from Wikipedia.org].

Now, all dependent on the signs of $\mu^2$ and $\lambda$, we get different scenarios. For the energy to be bounded from below (in order to have a state of minimum energy), we demand $\lambda$ to be positive, $\lambda > 0$. If also $\mu^2 > 0$, the potential $V(x)$ has a unique minimum at $\phi(x) = 0$, and so spontaneous symmetry breaking cannot occur. This situation is, in other words, uninteresting for us. However, if $\mu^2 < 0$ instead, the situation is quite different. We get a potential with no unique minimum, as shown in Figure 2.4. The state of the lowest energy is degenerate, the potential has a circle of minima;

$$\phi_0(x) = \sqrt{\frac{-\mu^2}{2\lambda}} e^{i\theta}\,, 0 \le \theta \le \pi\,. \tag{2.15}$$

Spontaneous symmetry breaking occurs, as already mentioned, through the act of choosing one state over the others to represent the ground state (the vacuum). Because the Lagrangian (equation 2.8) is invariant under the $U(1)$ gauge transformations (equations 2.11-2.13), it does not matter which value of $\theta$ we choose. We choose $\theta = 0$, and get

$$\phi_0(x) = \sqrt{\frac{-\mu^2}{2\lambda}} = \frac{v}{\sqrt{2}}\,. \tag{2.16}$$

Just because we can, and it turns out to be quite useful, we expand the $\phi(x)$ field around the vacuum by introducing two real fields $\sigma(x)$ and $\eta(x)$ according to the equation

$$\phi(x) = \frac{1}{\sqrt{2}}[v + \sigma(x) + i\eta(x)]\,, \tag{2.17}$$

where $\sigma(x)$ and $\eta(x)$ measure the deviation of the field $\phi(x)$ from the ground state $\phi_0(x)$, $\sigma(x)$ in the radial direction and $\eta(x)$ in the longitudinal direction. As we will see later, $\sigma(x)$ corresponds to the Higgs field and $\eta(x)$ is an unphysical field which gives rise to mass of the photon.

When inserting this the Lagrangian becomes

$$\begin{aligned}\mathcal{L} \;=\; & \frac{1}{2}[\partial^\mu\sigma(x)][\partial_\mu\sigma(x)] - \frac{1}{2}(2\lambda v^2)\sigma^2(x) \\ & - \frac{1}{2}F_{\mu\nu}(x)F^{\mu\nu}(x) + \frac{1}{2}(ev)^2 A_\mu(x)A^\mu \\ & + \frac{1}{2}[\partial\eta^\mu(x)][\partial\eta_\mu(x)] \\ & + evA^\mu(x)\partial_\mu\eta(x) + \text{'interaction terms'}\,,\end{aligned} \tag{2.18}$$

where the ’interaction terms’ are cubic and quartic in the fields, and a constant term has been discarded.

The interpretation of this equation is not straight forward; the mixed $A, \eta$-term is confusing and unphysical (it represents a vector field abruptly turning into a scalar field, which is forbidden). It is tempting to say that by expanding $\phi(x)$ around the vacuum, the $A_\mu(x)$ field has gained another degree of freedom, but because the $A_\mu(x)$ and $\eta(x)$ fields are mixed, one cannot say that the fourth and the fifth term in equation (2.18) represent a massive vector boson field and a massless scalar boson field respectively.

There is more trouble ahead; when realizing that this Lagrangian is the same as equation (2.8) - it expresses the same physics only in other variables - and counting degrees of freedom, we see that equation (2.18) has five degrees of freedom, and equation (2.8) has only four. Thus, it seems like an unphysical field (not describing any real particles) has been gained, contributing with a degree of freedom. Correct - this is the field $\eta(x)$, which has the unphysical, massless Goldstone boson associated with it. This field has to be eliminated in order to make the system physical again. The way to do this is to choose a unitary gauge; through a $U(1)$ gauge transformation $\phi(x)$ is turned into a real field

$$\phi(x) = \frac{1}{\sqrt{2}}[v + \sigma(x)] \,. \tag{2.19}$$

Substituting (2.19) into equation (2.8) we get

$$\begin{aligned} \mathcal{L} &= \frac{1}{2}[\partial^\mu \sigma(x)][\partial_\mu \sigma(x)] - \frac{1}{2}(2\lambda v^2)\sigma^2(x) \\ &\quad - \frac{1}{2}F_{\mu\nu}(x)F^{\mu\nu}(x) + \frac{1}{2}(ev)^2 A_\mu(x)A^\mu \\ &\quad + \text{'interaction terms'}. \end{aligned} \tag{2.20}$$

Since there no longer are any mixing terms, we are free to interpret the last term in equation (2.20) as a massive vector boson field. Thus, through the expansion of $\phi(x)$ and this gauge transformation, the problems are solved.

So, looking from the start at the Lagrangian (2.8), we can say that the photon (which has two degrees of freedom) has “eaten” the Goldstone boson (associated with the $\eta(x)$ field) and gotten its degree of freedom, which is the same as saying that the photon has become massive (it has the ’freedom not to move at the speed of light’).

This mechanism - that a gauge boson gains mass (through that the vector field eats a scalar one) without spoiling the gauge invariance is called the Higgs mechanism. This mechanism removes the unphysical Goldstone boson(s) that are created through the spontaneous symmetry breaking. The massive spin-0 particle associated with the real $\sigma(x)$-field is called the Higgs boson, and its mass is given by the curvature of the potential.

So, now we are happy that we have have found a mechanism that creates mass without spoiling the gauge invariance of the Lagrangian. However, we are not too pleased with the fact that the photon has gained a mass, since this is not the case in nature. But when the Higgs mechanism is applied to $SU(2) \times U(1)$ gauge theory and the choice of the ground state is made in such a way that conservation of electric charge is retained (in order to keep the photon massless), we can achieve that the W and Z bosons gain mass, while the photon stays massless as electromagnetism is unbroken.

### 2.2.3 The Standard Electroweak Theory

The Higgs mechanism will now be applied to $SU(2) \times U(1)$ gauge theory, which together makes up the Electroweak theory. Since $SU(2)$ invariance shall be broken, a scalar field with at least three components needs to be applied (in order to give mass to the three $W^{\pm}, Z$ bosons) with a non-zero weak isospin. The easiest solution is an $SU(2)$-doublet

$$\Phi(x) = \begin{pmatrix} \phi^{+} \\ \phi^{0} \end{pmatrix} . \tag{2.21}$$

The wish is to include a Higgs scalar field in the Lagrangian and still continue to be $SU(2) \times U(1)$ gauge-invariant.

The Lagrangian for the scalar field,

$$\mathcal{L} = [D^{\mu}\Phi(x)]^{*}[D_{\mu}\Phi(x)] - \mu^{2}|\Phi(x)|^{2} - \lambda|\Phi(x)|^{4} , \tag{2.22}$$

is added to the total Lagrangian of the Electroweak theory, where $D_{\mu}$ is the covariant derivative of the standard Electroweak theory[9].

For $\lambda > 0$ and $\mu^{2} < 0$, the symmetry is as usual broken. The vacuum expectation value is chosen to be non-zero in the neutral part of the Higgs doublet $\Phi(x)$ in order to keep electromagnetism unbroken (as the photon must stay massless). This vacuum expectation value is

$$< 0|\Phi(x)|0 >= \begin{pmatrix} 0 \\ v/\sqrt{2} \end{pmatrix} , \tag{2.23}$$

with $v$ as in (2.16).

We use the same tricks as for the $U(1)$ Higgs model - $\Phi(x)$ is written in terms of four real fields to describe the deviation from the vacuum state

$$\Phi(x) = \frac{1}{\sqrt{2}} \begin{pmatrix} \eta_{1}(x) + i\eta_{2}(x) \\ v + \sigma(x) + i\eta_{3}(x) \end{pmatrix} , \tag{2.24}$$

and a gauge transformation is made to make $\Phi(x)$ go to the unitary gauge, because the fields $\eta_{i}(x), i = 1, 2, 3$ are unphysical. These fields “give” their degree of freedom to the $W^{\pm}$ and $Z$ bosons, which thus become massive, and all is well.

---

[9] See for example equation (13.29) in Quantum Field Theory, Revised Edition by F.Mandl & G.Shaw [6] for the total Lagrangian of the electroweak theory, and equation (13.33) in the same book for $D^{\mu}$.

The mechanism for giving the leptons and quarks masses is also included in the standard Electroweak theory. This happens through the interaction of leptons and quarks with the Higgs scalar field, see Equation 2.4. If masses are given to the neutrinos (as is done in the non-minimal SM, not included in Equation 2.4), neutrino mixing will occur. This is due to the fact that the mass eigenstate neutrinos in the model are not the same as the leptonic neutrinos that are observed.

## 2.3 Beyond the Standard Model

As mentioned, the SM is not a complete theory. Some of the fundamental questions unanswered by the SM are [8, 18]:

- what is the dark energy and dark matter we know 96% of the universe is built up of [19]?
- why is QCD confined?
- why is there such a huge asymmetry between matter and antimatter in the universe?
- is it possible to unify all the forces to one?
- do the constituents have a inner structure themselves?
- how does gravity fit into all of this?
- are the parameters of the SM really independent?

There are many models for so-called exotic physics, or physics beyond the Standard Model, some of them giving answers to questions the Standard Model cannot answer. We will now have a short look at some of the most important models, that is supersymmetry and technicolor.

### 2.3.1 Supersymmetry (SUSY)

Here we give a very brief introduction of the simplest of the supersymmetric scenarios, the MSSM - the Minimal Supersymmetric Standard Model[10].

Supersymmetry introduces a new symmetry between force and matter particles - a connection of integer-spin particles and half integer-spin particles. By introducing supersymmetry, one gets a lot of new parameters to juggle with (compared to the SM). In the MSSM one takes the least extension possible of the SM[11], which results in the vast number of parameters of 124 [20].

SUSY is a good means of solving some issues the SM cannot, as the fine-tuning problem, the hierarchy problem, unification of the forces and it also includes a good candidate for dark matter[12].

---

[10] This section is mainly based on the article "The Anatomy of Electro-Weak Symmetry Breaking, Tome II: The Higgs bosons in the Minimal Supersymmetric Model" by Abdelhak Djouadi [18].

[11] Other theories, making a larger extension of the SM also exist, as for instance NMSSM - the Next to Minimal Supersymmetric Standard Model.

[12] If R-parity conservation is assumed, the lightest supersymmetric particle is absolutely stable.

In the following we briefly explain these issues.

First, the fine-tuning problem: If we choose the cut-off $\Lambda$[13] to be at the GUT[14] scale, the mass of the Higgs boson will prefer to be at a very high scale, unless we do an unnatural fine-tuning of parameters. This is what is called the fine-tuning problem, and it is a problem because we know from fits to precision electroweak measurements that the mass of the Higgs boson should be less than 260 GeV at the 95% confidence level [21]. The quantum instability of elementary scalar masses can be overcome through supersymmetry because quantum corrections of fermions and bosons have different sign - therefore many of them cancel [5].

The hierarchy problem is that there is no satisfactory answer in the SM as to why $\Lambda >> v$. If SUSY exists, then the cut-off scale $\Lambda$ will most likely be at around the TeV scale, which is far closer to the vacuum expectation value $v \approx 260$ GeV than the GUT scale.

When it comes to the unification of the forces - using only the SM as it is, the three gauge couplings (the electromagnetic, the weak and the strong) do not meet at any one point. The new SUSY particle spectrum alters the slope of these three coupling constants so that they meet at an energy scale of about $10^{16}$ GeV.

In SUSY, two complex Higgs doublets are needed. This is due to the fact that it is not allowed to introduce a right-chiral[15] superfield in a superpotential [20]. Since we need something to give mass to the down-type quarks and charged leptons, a *second* left-chiral scalar doublet superfield must be introduced, with weak hypercharge $Y^W = 1$. The pattern of breaking the symmetry is the same as for the Standard Model, but since there are two complex doublets, we end up with eight degrees of freedom (two for each of the components in the doublets). Three of the degrees of freedom will be dedicated to giving $W^{\pm}$ and $Z$ mass, and thus we are left with five Higgs bosons. One of these five Higgs bosons, the $\mathrm{h}^0$, is almost indistinguishable from the Standard Model Higgs.

The mass limits of superparticles (given that they have not been observed at experiments yet) indicate that this is a broken symmetry (or else we would have seen these particles at the energy scale the existing experiments are probing). Since the MSSM has this large number of parameters, it is impossible to do phenomenology with it, so the approach is normally to choose a way of breaking the symmetry (for instance gravity mediated symmetry breaking, or gauge mediated symmetry breaking), which reduces the number of parameters. As an example mSUGRA (the minimal SUperGRAvity model) has five parameters at the GUT scale [20].

---

[13] The cut-off scale $\Lambda$ is where the theory stops being valid and new physics enters [18].

[14] Grand Unified Theory, the scale at which the three gauge couplings of the SM seem to unify and become one - all three forces are described by a single, larger gauge group, such as SU(5) or SO(10). This happens at an energy scale of about $10^{16}$ GeV [5, 18].

[15] Chirality, or handedness, is whether a particle transform into a right- and left-handed representation of the Poincaré group. A particle can be right-handed, or left-handed. A closely related, but not equivalent, term is helicity. Helicity is the component of the spin in relation to the momentum. A particle with spin and momentum pointing in the same direction have negative helicity, a particle that have them pointing in opposite directions have positive helicity. Chirality is linked to helicity - for massless particles this is the same - because a particle of zero mass will travel at the speed of light, and chirality is invariant under Lorentz transformations, whereas helicity is not. Both are interchanged under parity transformations [7].

### 2.3.2 Technicolor

As described by the fine-tuning problem, the Higgs scalar field gives us some trouble - there are large corrections to the Higgs boson mass due to the presence of physics of higher energy scales. One way of "solving" (that is, avoiding) this problem, is simply to find a solution where you do not need to have a scalar field at all. One way to get rid of the need of a scalar field, is a theory called technicolor. The idea of it goes as follows: A quark-antiquark condensate will also contribute to electroweak symmetry breaking, but if this were the only mechanism for breaking the symmetry, the weak bosons, W and Z, would be predicted to have masses of about 30 MeV. This is clearly not the case, as measurements have shown these bosons to have masses in the order of ∼100 GeV. To correct for that the weak bosons gain too small a mass (if this was the only mechanism breaking the symmetry), one introduces a new gauge interaction called technicolor. Fermions with technicolor charge will condense at scale $v \sim \frac{1}{4}$TeV, spontaneously breaking a chiral and the EW gauge symmetry. This theory predicts a wealth of new composite particles at the TeV scale. It is, though, difficult to create such a theory which is consistent with all the current data [5].

## 2.4 Production Mechanisms of the Higgs Boson at the LHC

We will now have a look at some of the more important production mechanisms for the Higgs boson in the high energy proton-proton collisions at the LHC.

There are several different ways the Higgs boson can be produced. How important these different production mechanisms are, depends on the mass of the Higgs boson, which is, as previously mentioned, not known (but searches done at LEP and EW calculations suggest that it is light, see Section 2.5 for more information).

The gluon-gluon fusion production mechanism dominates in a large range of possible masses, as seen in Figure 2.5. As the Higgs boson couples to mass, and the gluons are massless, this is a higher order process, going through a loop of heavy particles (mostly the top-quark). The feynman diagram of this process can be seen in Figure 2.6. Please note that the colors of Figure 2.5 and Figure 2.6 are correlated. The feynman diagram of the second most important production mechanism, vector boson fusion, is also displayed in Figure 2.6.

Associated production, that is when something besides only the Higgs boson is produced, has a much lower cross-section - about a factor 10-100 less than gluon-gluon fusion (see Figure 2.5). Examples of feynman diagrams for these kinds of processes can also be seen in Figure 2.6 (in this figure, gluon-gluon fusion is the only feynman diagram not displaying associated production). Even though associated production processes are much rarer than gluon-gluon fusion, they might turn out to be useful, to avoid our signal being drowned in the enormous QCD background. The production cross-section is lower, but the backgrounds are also much smaller than the vast QCD background.

It is a point to be able to study the Higgs boson produced in many different ways - to measure its coupling to as many particles as possible (given that it exists at all, of course). In addition, different

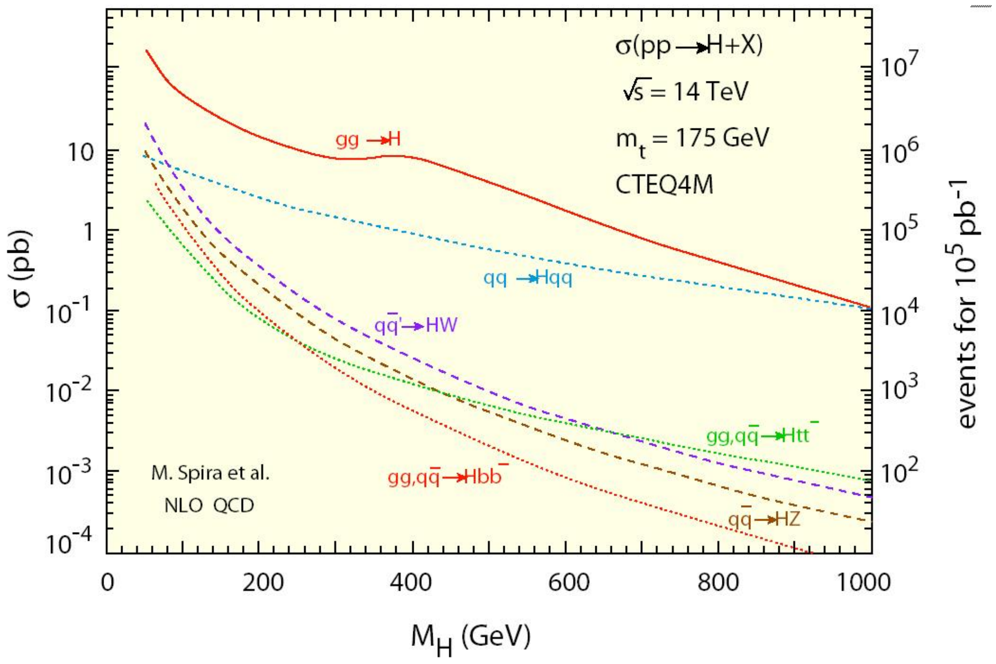

Figure 2.5: The production rates for the Higgs boson [from www.hep.ph.ic.ac.uk].

production mechanisms give us different signals to look for, which all have their advantages and disadvantages. As an example, the Htt associated production is interesting because it reduces the background and at the same time it will tell us something about the coupling of the Higgs boson to the top quark (which should be rather strong, since the coupling goes proportional to the mass). If the Higgs boson is not heavy enough to decay into a pair of top quarks, we need this associated production process to explore the coupling of the Higgs to the top. As mentioned earlier, only an inclusive analysis will be considered in this thesis - that is an analysis that does not care about the way the Higgs boson was produced.

As one can see from Figure 2.7, the $H \rightarrow \gamma\gamma$ decay is a rare one - it has a branching ratio of around 0.2% or less, but it is still interesting because the signature is simple and clear and because

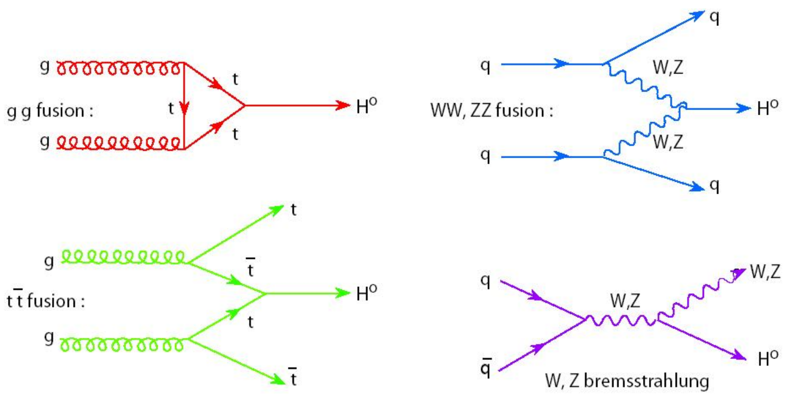

Figure 2.6: Some feynman graphs for production of the Higgs boson in p-p collisions [from www.hep.ph.ic.ac.uk].

of the (relatively) small amount of background contributing to this decay channel. See Chapter 4 for more information on the background to this channel.

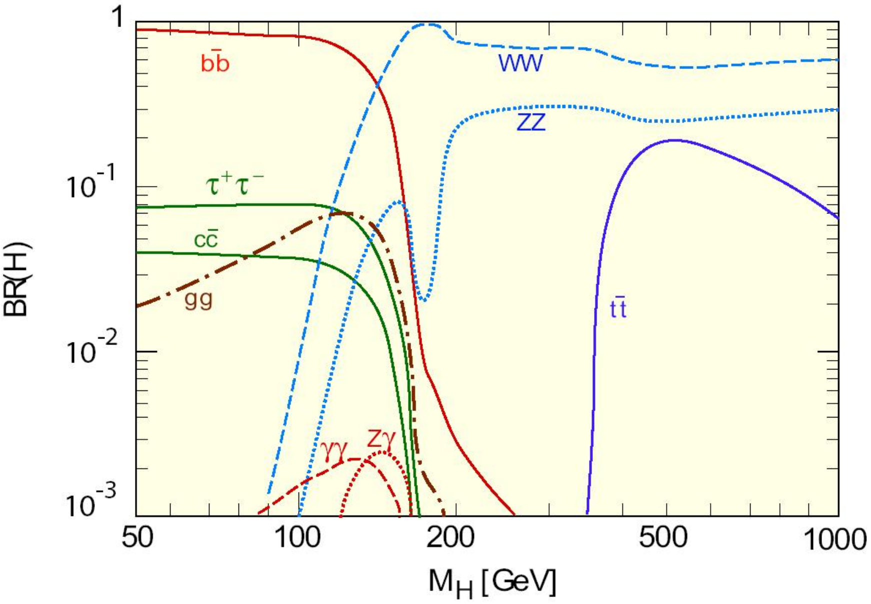

Figure 2.7: The branching ratio of the Higgs boson as a function of its mass [from www.hep.ph.ic.ac.uk].

## 2.5 The Limit on the Higgs Boson

Measuring the masses of the known particles of the SM with higher precision will constrain the Higgs mass. This is especially important for the heavier particles, such as the $W$ boson and the top quark (the $Z$ boson is already measured with high precision). By measuring the parameters of the SM to a higher precision, yesterday's accelerators have helped constrain the Higgs mass. The Tevatron[16] is nowadays, in addition to searching for the Higgs boson, also constraining its mass, and has added more to the constraints especially through measurements on the top quark[17], produced at a high rate there [22].

Figure 2.8 is made up from measurements done at LEP[18], SLC[19] and Tevatron and calculations of all the unfree parameters of the SM, which will constrain the only free parameter left - the Higgs boson mass [23]. This plot shows us the $\Delta\chi^2$ as a function of the Higgs mass (on a logaritmic scale) - which is dependent on the difference between the measured data and the calculated values. The $\Delta\chi^2$ tells us how likely it is to find a variable at a certain value; where the $\Delta\chi^2$ has its minimum (where the difference is the smallest), is where the probability is the highest. The area examined directly by LEP, where the presence of a Higgs boson is excluded, is colored yellow, the blue band

---

[16] A circular proton-antiproton accelerator with a center of mass energy of 1.96 TeV. Tevatron is situated at Fermi National Accelerator Laboratory, near Chicago, IL.

[17] Tevatron is the only laboratory as of today with high enough energy to produce the top quark.

[18] Large Electron-Positron collider which was situated at CERN and operated from 1989 till 2000.

[19] Stanford Linear Collider; an electron-positron linear collider.

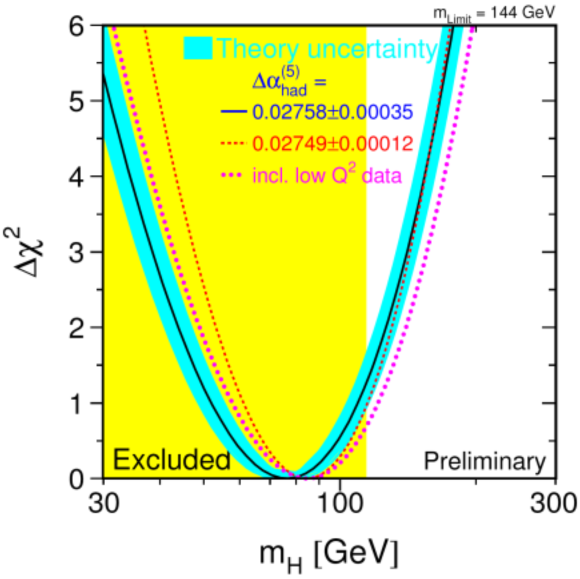

Figure 2.8: A least-squares plot as a function of the Higgs mass [from arXiv:0712.0929v2].

is the estimated theoretical error from unknown higher order corrections. The most probable place of finding the Higgs boson, according to these calculations, is already excluded by LEP, so it is expected (or hoped) that the Higgs boson will be found at a mass near the exclusion limit. If this is not the case, the Standard Model is poorly understood, or it is not the whole story (see section 2.3 for beyond the Standard Model physics).

The limit on the Higgs mass set by LEP is 114.1 GeV at a 95% confidence level [24]. We can see that a light Higgs boson is favored by the existing electroweak precision measurements. Figure 2.8 and the calculation behind it, leads in all to a 95% confidence level upper limit of $M_H < 260$ GeV [21].

# Chapter 3

# The ATLAS Experiment at CERN

In this chapter, an introduction of the tool used for exploring the theoretical model in Chapter 2 will be made. This tool is the ATLAS detector, situated at one of the collision points of the Large Hadron Collider (LHC), located at CERN. We will have a look at what CERN and LHC are, how the ATLAS detector is built up and how the different parts of it function. We will also see how to recognize different particles using the detector, how to design an analysis based on the detector information and finally the how the trigger and data acquisition systems work.

## 3.1 CERN

CERN, Conseil Européen pour la Recherche Nucléaire - European Council for Nuclear Research, is situated right outside Geneva, on the border between Switzerland and France. CERN is one of the largest centers in the world for scientific research, was established in 1954 and has of today 20 European Member States. Scientists from all over the world, representing 85 countries and 580 universities, come to do research there - as many as 8000 scientists visit CERN each year, this is about half of all particle physicists. The number of employees at CERN is 2500 [25].

## 3.2 The Large Hadron Collider

The LHC is the newest and most powerful particle accelerator built by CERN, and started up the 10th of September 2008 (before an accident occurred, causing it to be shut down again), after more than twenty years of planning and building. The LHC is as of today not only the largest and most powerful particle accelerator at CERN, but in the world. The two proton beams travelling in the LHC will have an energy of up to 14 TeV in the head-on-head collisions that will take place in the detectors. It is designed to have a luminosity (depending mainly of the rate of proton bunches, the number of protons in each bunch and the cross-section of the beam) of $10^{34}\text{cm}^2\ \text{s}^{-1}$ at its maximum, reaching it after about three years of running. Beams of lead will also be made, colliding with a maximum beam energy of 2.76 TeV per nucleon [26], at a design luminosity of $10^{27}\text{cm}^2\ \text{s}^{-1}$ [27].

Figure 3.1: Location of CERN in Europe [from earth.google.com].

See Figures 3.1, 3.2 and 3.3 for the location of CERN in Europe, the LHC accelerator ring and the four different experiments situated around it. These four different experiments are:

- ALICE - A Large Ion Collider Experiment at CERN LHC
  A detector built to focus on heavy-ion (lead) collisions to investigate the nature of the quark-gluon-plasma.

- ATLAS - A Toroidal LHC ApparatuS
  A general-purpose detector searching for 'whatever it can find', such as the Higgs boson, extra dimensions and particles that could be responsible for dark matter and supersymmetry.

- CMS - Compact Muon Solenoid
  A general-purpose detector with the same goals as the ATLAS detector. Having these two detectors reduces the possibility of biased results and makes discoveries more convincing.

- LHCb - Large Hadron Collider beauty
  This experiment will investigate why the antimatter-matter balance is so skew as we observe in the universe today by high-statistics studies of hadrons containing a b-quark.

The picture in Figure 3.2 is taken from the air above Geneva with the LHC ring and the SPS (Super Proton Synchrotron), the final injector of protons to the LHC, sketched in. The CERN working area can be seen as a triangle where the two rings meet. Please note that the accelerator ring is in reality not to be seen on the surface, as it is placed approximately 100 meters underground, which is illustrated in Figure 3.3.

Figure 3.2: Photograph taken above Geneva; the LHC ring and the SPS are sketched in. The Geneva airport and Lake Geneva can be seen on the right [Picture from University of Florida].

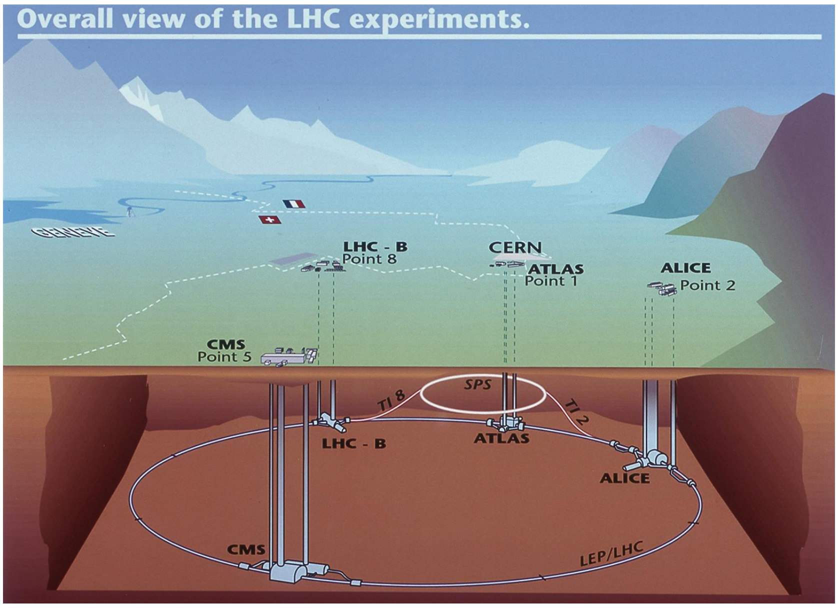

Figure 3.3: Figure of the location of the four experiments situated around the LHC ring, approximately 100 meters underground [from the multimedia gallery of www.cern.ch].

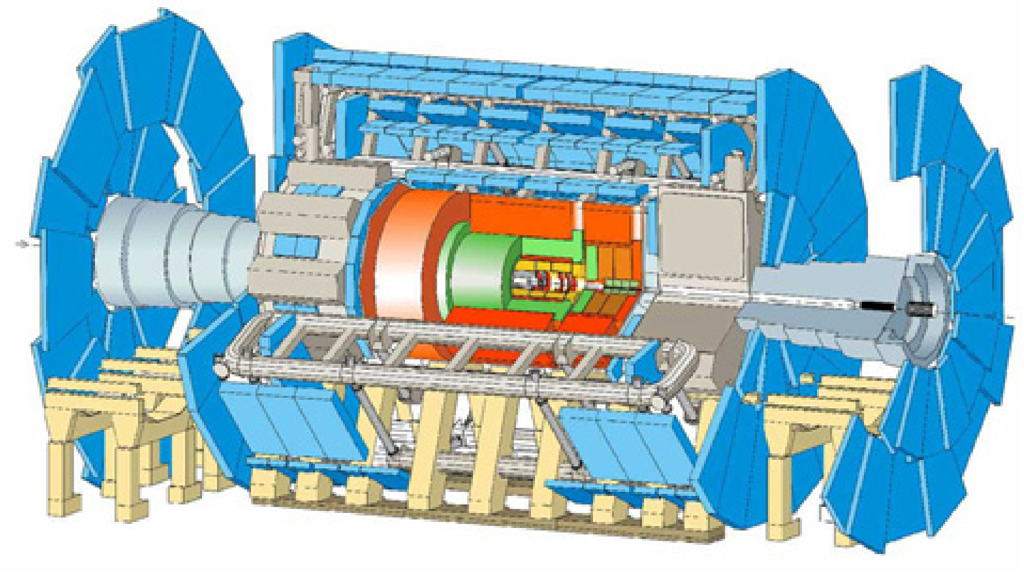

Figure 3.4: A schematic illustration of the ATLAS detector. The different colors indicate the different detector components - going from the center and outwards; the inner detector in yellow, the solenoid magnet in red, the electromagnetic calorimeter in green, the hadronic calorimeter in orange, the torodial magnet system in grey and the muon detectors in blue [from www.cern.ch].

## 3.3 The ATLAS detector

The ATLAS detector is about 25 meters high and wide, and about 46 meters long, weighs roughly 7000 tons, and is, like the rest of the detectors at the LHC, placed approximately 100 meters underground. It is also the largest volume particle detector ever constructed for an accelerator-based experiment [28].

The detector, shown schematically in Figure 3.4, is built with an “onion” structure, with different layers of detectors at increasing radius, and is hermetic - covering a full $4\pi$ of the solid angle, in order to be able to indirectly detect missing energy of particles escaping the detector. It has both a barrel, and an end-cap structure. In Figure 3.5, the coordinate system used by ATLAS is displayed.

### 3.3.1 Detector Components

For the analysis done in this thesis, the inner detector, the presampler and the electromagnetic calorimeter will be the parts of ATLAS that are crucial. The two photons that we search for will (mainly) be stopped before the hadronic calorimeter, so the components after the electromagnetic calorimeter are in general of less interest to us. The exception is the first compartment of the hadronic calorimeter, from which the information might help in a separation of $\pi^{\pm}$ and $e^{\pm}$ (this is of interest because $\mathrm{e}^+\mathrm{e}^-$ pairs might be accepted as converted photons, so we do not want a contamination of electrons from charged pions). The inner detector will be important for this analysis because it will measure the tracks we will need (or the lack of tracks, in the case of photons) and tell us whether any photon conversions into $\mathrm{e}^+\mathrm{e}^-$ pairs have taken place. The

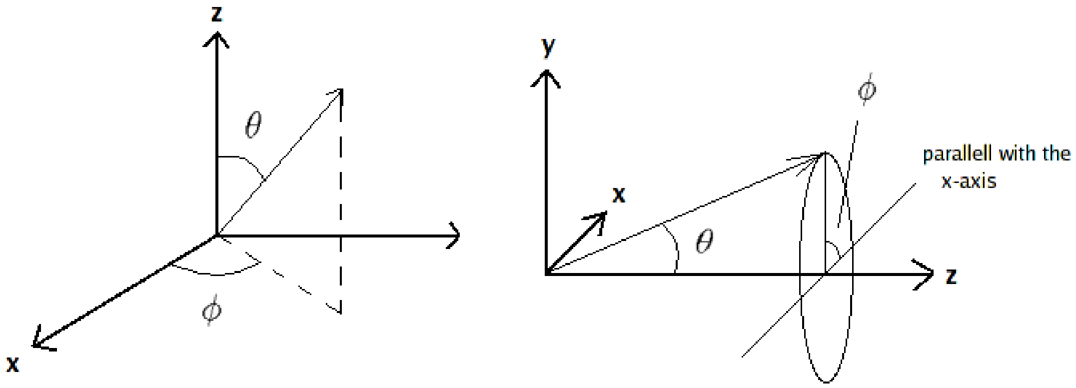

Figure 3.5: Coordinate system used in ATLAS seen from two different angles; x is inwards from the interaction point towards the center of the LHC ring, y is up towards the surface and z is along the beam. $\phi$ is the azimuthal angle; in the (x-y)-plane (so it is running 'around the beam') and $\theta$ is in relation to the z-axis. Instead of $\theta$, it is more common to use the pseudorapidity, $\eta$, given by $\eta = -ln[tan(\frac{\theta}{2})]$ [29].

presampler, located in front of the electromagnetic calorimeter, will give us more accurate energy measurements. The electromagnetic calorimeter, in addition to giving us the energy measurement, will be important as it is the only device that will measure the trackless (due to their zero charge) photons, unless they convert. It must measure the directions of the photons precisely, so one can reconstruct that they came from the same origin (this is called "pointing") [30], in order to reconstruct the vertex and mass of the Higgs boson. In a typical $H \rightarrow \gamma\gamma$ event, there will not be so much else happening in the detector; therefore, it is of great importance that the electromagnetic calorimeter does the job well, so that the vertex and mass can be reconstructed with the little information there is.

### The Inner Detector

The Inner Detector (ID) has an outer radius of 1.15 meters, and a length of 7 meters. It consists of the Pixel Detector, the SemiConductor Tracker (SCT) and the Transition Radiation Tracker (TRT). These detectors will only measure particles with an electric charge. The placement of the inner detector can be seen in Figure 3.4, where the inner detector is colored yellow. See Figure 3.6 for the structure of the inner detector itself.

The Pixel Detector starts at approximately five centimeters radially from the beam and goes on until twelve centimeters, consists of three layers, is very radiation hard and is meant to detect the secondary vertices of short lived systems, such as the $\tau$-lepton and the b- and c-quarks. Due to the extreme radiation this detector will be exposed to, the planning of renewing these inner detectors is already on-going; a part of the Pixel Detector is planned to be replaced in the end of 2012, and a major upgrade is planned to take place at the end of 2016 [31].

The SCT spans the area given by a radius between 30 and 52 centimeters in eight layers, giving eight measurements contributing to the determination of momentum and impact parameter[1] and vertex reconstruction.

The TRT starts at a radius of 56 centimeters, and ends at a radius of 107 centimeters. It consists of straw detectors - the straws are filled with a Xenon mixture gas, which picks up the X-ray transition radiation initiated by the low-density polypropylene/polyethylene fibre radiator filled in-between the straws [33]. Each straw is 4 millimeters in diameter and has a 30 micrometer wire for readout in the middle. The barrel contains 50 000 straws, the end-caps 320 000 and all straws give a measurement of drift time used to find the position of the hit. The purpose of the TRT, in addition to charged particle tracking, is to contribute to a more decisive detection of electrons using transition radiation, which occurs when a charged particles passes suddenly between materials with different refractive indices[2]. This process is not important for energy loss, but can be used as a part of particle identification. What frequency the radiation sent out has depends on the relativistic $\gamma$-factor[3] of the particle - a particle with a $\gamma$-factor of $10^3$ will emit radiation in the soft X-ray range of 2-20 keV [26]. Heavier charged particles will have a lower $\gamma$-factor, and thus radiate in a range where the TRT is not sensitive.

These three sub-detectors are contained inside a solenoid magnet of 2 Tesla, bending the tracks of charged particles in order to measure their momenta. All the elements of the inner detector are supposed to affect the particles travelling through them as little as possible, in order to get an as correct and full measurement of their energy as possible in the calorimeters (which will shortly be described). Effects like photons converting into $e^+e^-$ pairs, bremsstrahlung and multiple scattering makes the job of reconstructing what happened in the detector more difficult, and the probability of these processes increase with the material the particles have to pass through. Therefore, a low amount of material before the calorimeters is desired.

### The Calorimeters

The calorimeters' main task is to detect the energy of the particles, by absorbing them. The electromagnetic calorimeter, as can be seen in Figure 3.4 colored in green, stops electrons and photons completely, the hadronic calorimeter, colored orange in Figure 3.4, stops hadrons[4]. The particles interact with the matter in the calorimeters, and gradually split up in new particles, creating what is called showers.

The energy resolution of calorimeters can be parameterized as

$$\frac{\sigma}{E} = \frac{a}{\sqrt{E}} \oplus b \oplus \frac{c}{E} \quad , \tag{3.1}$$

---

[1] Impact parameter is found by extrapolating a track back to the primary vertex - it is the perpendicular distance in the transverse plane ($r - \phi$) (in the longitudinal plane, for longitudinal impact parameter) between the extrapolated track and the primary vertex [32].

[2] The refractive index tells something about the optical property of the material, indicating for instance how fast light would travel through it.

[3] $\gamma = \frac{E}{mc^2}$.

[4] Hadrons are particles consisting of quarks. Particles built up of a quark and an anti-quark are called mesons, while the ones built up of three quarks are called baryons.

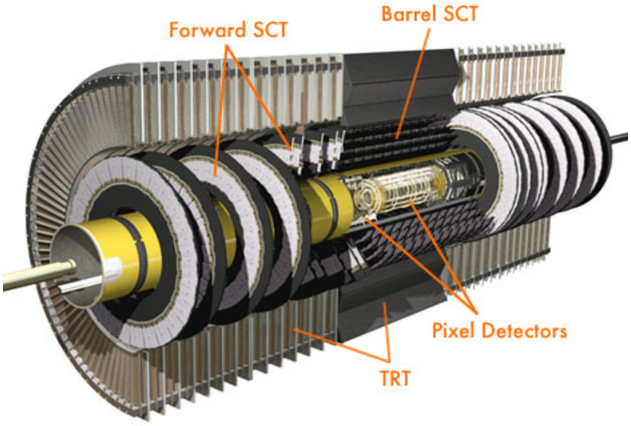

Figure 3.6: Schematics of the inner detector of ATLAS [from www.atlas.ch/inner_detector].

where $\oplus$ is an addition in quadrature[5], $a$ is the sampling term[6], $b$ is the constant term[7] and $c$ is due to electronic noise [34]. Thus, the higher the energy deposited, the more accurate the measurement of the energy.

For the momentum resolution, the complete opposite applies - the higher the momentum, the worse the resolution of the momentum. This is due to the fact that the momentum is determined from the curvature of the bent track (due to the magnetic field, given that the particle has an electric charge), and the higher the momentum, the less the particle is affected by the magnetic field and so the less bent the track is. The smaller the bending of the track, the more difficult it is to determine the curvature. This we can see from equation 3.2, in which the momentum resolution is proportional to the momentum, in contrast to equation 3.1, in which the energy resolution is inversely proportional to the energy. The relative momentum resolution is given by

$$\left.\frac{\sigma(p_T)}{p_T}\right|^{measurement} = \frac{\sigma(s)}{s} = \frac{c\cdot\sigma(x)p_T}{0.3BL^2}\,, \tag{3.2}$$

where $s$ is the sagitta (see figure to the right) related to the measurements in $x$ in this manner $s = x_2 - \frac{x_1+x_3}{2}$, the error on $x$ being $\sigma(x)$. $c$ is a constant, $B$ is the strength of the magnetic field and $L$ is the length of where the particle is exposed to a magnetic field.

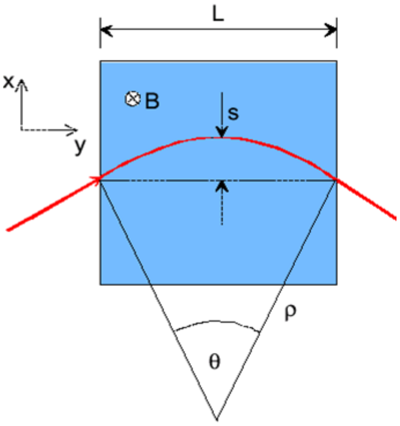

---

[5] That is $\sqrt{(\frac{a}{\sqrt{E}})^2 + b^2 + (\frac{c}{E})^2}$

[6] The sampling term represents statistically related fluctuations, such as dead material in front of the detecting parts of the calorimeter and sampling fluctuations.

[7] The constant term represents the fact that the calorimeter is not uniform, and therefore does not sample the energy uniformly either. If we had exposed different parts of the calorimeter to the same energy, we would have gotten different read-outs. One has tried to take care of this, but the corrections/calibration are not perfect. With effort this term can be reduced to below 1%, and the goal of ATLAS is 0.7% [27].

The electromagnetic calorimeter consists of a barrel part, covering $|\eta|$<1.475 and two end-cap parts, covering 1.375<$|\eta|$<3.2. It is a lead-LAr (Liquid Argon) detector, built with an accordion shape. The presamplers, covering $|\eta|$<1.8, have a granularity given in $\Delta\eta \times \Delta\phi$ of 0.025×0.1 both in the barrel and end-caps. The number of read-out channels for the presampler is 7808 in the barrel and 1536 in the end-cap. The electromagnetic calorimeter has different granularity for different values of $|\eta|$ and of the three different layers it consists of. For instance, the first layer of the barrel has 0.025×0.025 for 1.40<$|\eta|$<1.475, while the first layer of the end-cap is 0.025×0.1 for 1.425$|\eta|$<1.5. The number of read-out channels for the calorimeter is 101.760 in the barrel and 62.208 for each of the end-caps [27].

The region (1.37<$|\eta|$<1.52) is called the crack region. It is an overlap area (a gap between the barrel and end-cap calorimeters) where the electromagnetic calorimeter performs poorly due to components like ID services, cables and cryostat walls, see Figure 3.7 [29].

The presampler is, as mentioned, important for this analysis. The function of the presampler is to make up for the energy losses due to the material in front of the calorimeter, such as the cryostat walls, the superconducting coil, the inner detector and cables - all the material in front of the electromagnetic calorimeter is made with the intention of minimizing it, but at some places it still exceeds three radiation lengths, $X_0$ [30]. All this material in front of the calorimeter causes showers to start before the particle has reached the calorimeter, which is unfavourable because there are no devices for detecting energy deposits before the calorimeter - the energy lost by the particle before the calorimeter would be unseen, and we would reconstruct the particle with too low an energy. As said, the presampler makes up for this loss of energy of the particles before the calorimeter has been reached. Having this purpose, the presampler is placed in front of the electromagnetic calorimeter, see Figure 3.7 [35]. It consists of an active LAr layer of 1.1 cm thickness in the barrel region, and of 0.5 cm thickness in the end-cap region [27]. The presampler is an additional sampling device that is read out independently from the rest of the calorimeter and is used where $|\eta| < 1.8$ [30]. As it is used only for energy measurements, its granularity is coarser than in the calorimeter.

The material in front of the electromagnetic calorimeter was increased by an average of $0.15X_0$ with respect to the Technical Design Report (TDR) made in 1999 (partly due to that some changes were made in the inner detector layout). This causes more photons to convert (with respect to the TDR study), and therefore degrades the calorimeter performance. The gap between the barrel and endcap also increased by 4 cm in the z-direction, which potentially can affect the endcap calorimeter performance [36, 27].

For Higgs boson decays where the two photons are within $|\eta| < 2.5$, as much as 57% of the events will have at least one conversion inside a radius of 80 cm in the detector [1].

**The Muon Spectrometer**

All the parts colored blue in Figure 3.4 are the muon spectrometer. Muons are the only particles to survive this long in the detector and still be detected - they are so-called minimum ionizing particles; muons leave a little of their energy all the way through the detector. The momentum of

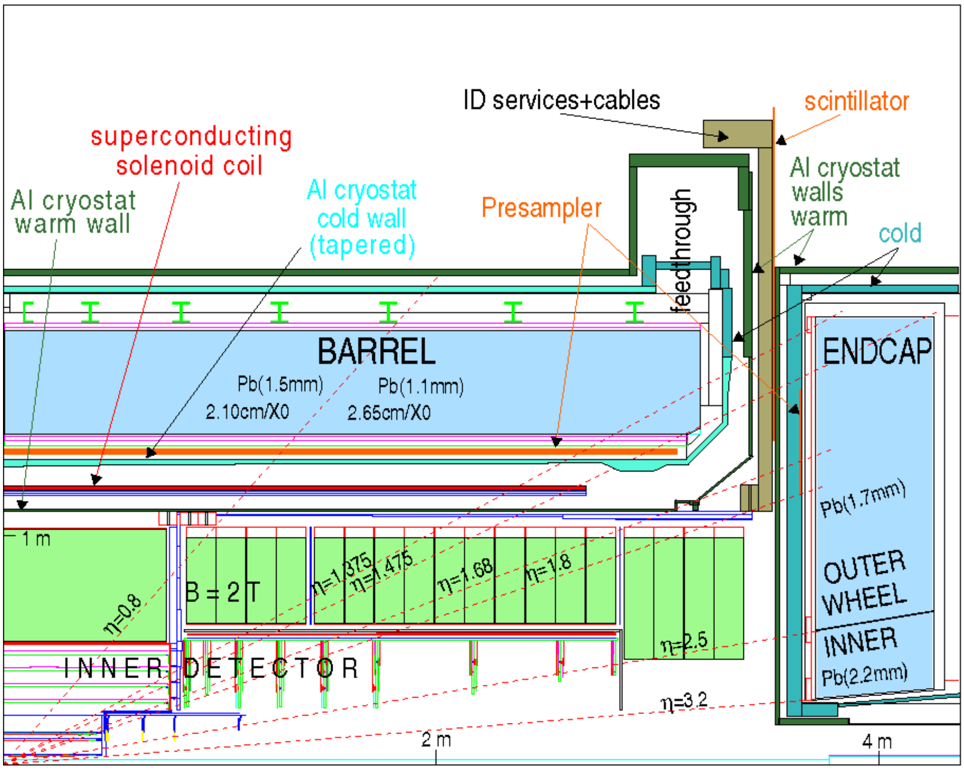

Figure 3.7: Longitudinal view of the ATLAS EM calorimeter [from ATLAS TDR].

the muons is determined by measuring the bending of the track in the magnetic field set up by the torodial magnets (colored grey in Figure 3.4), deflecting the muons as they pass through the layers of the muon spectrometer. The sensors in these detectors are similar to the straw tubes described in the inner detector (specifically in the TRT), but with a larger tube diameter.

### 3.3.2 Particle Identification with the ATLAS Detector

Combining the information from all of the different layers of the detector will give information about which particle it is that is observed, as well as its momentum and energy. As one can see from Figure 3.8, different particles behave differently in the detector.

Taking two examples:

- A photon, having no charge, will leave no track in the inner detector, and make a shower in the electromagnetic calorimeter where it will be stopped.
- A proton, having charge, will leave a track in the inner detector and will be deflected by the magnetic field set up by the solenoid, which will make a measurement of the momentum possible. Further on, the proton will pass the electromagnetic calorimeter and go to the hadronic calorimeter, where it will make a shower and be stopped.

In this manner, one can combine the information from the different parts of the detector to give a good guess about what kind of particle one is dealing with. Of course, this process is not as straight forward as it might seem, given that the real world is complicated, and the detector not perfect; tracks might not be found, the reconstruction may not give the full energy measurement, parts of the detector can be dead or read out incorrectly, etc. In addition to the imperfection of the detector, the complexity of nature, like pile-up and the fact that a lot of things are going on at once, filling the detector with hits, can make life as a particle physicist more difficult. In Figure 3.9 one of the simulated events to be used in this thesis is displayed. The energy deposits from the two photons are clearly seen.

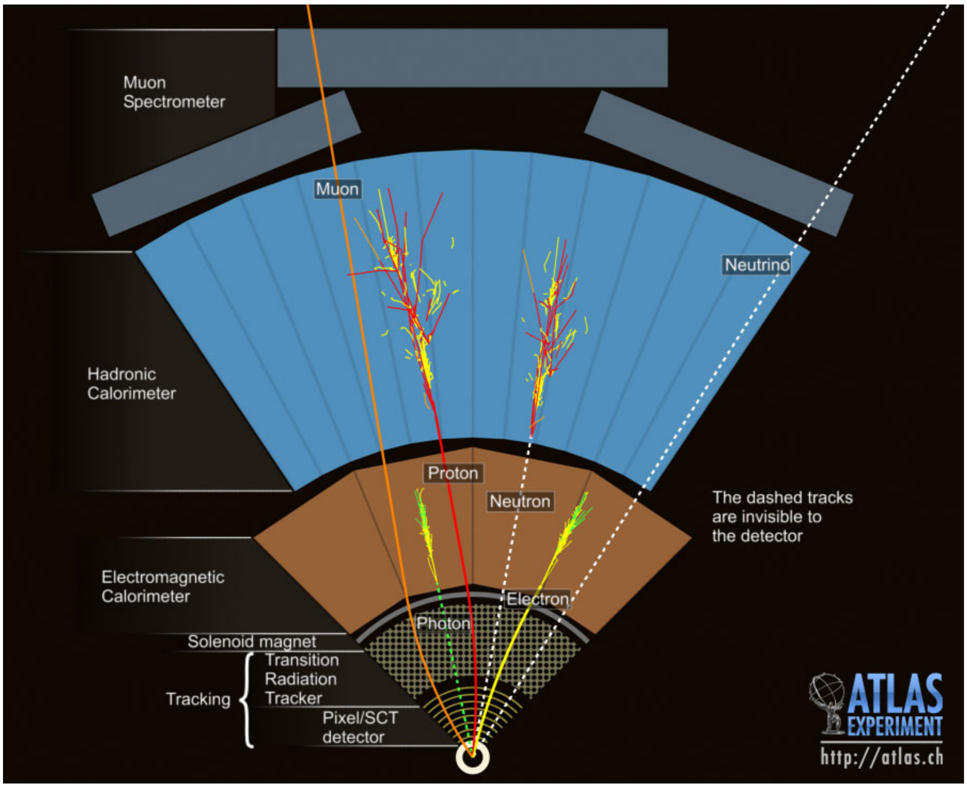

Figure 3.8: How to identify different particles using the ATLAS detector [from http://atlas.ch].

### 3.3.3 Building Up An Analysis

Highly unstable particles live far too short a time to be detected directly in the detector. This is the case for most of the particles we are searching for as of today. The approach one uses to find this kind of particle is to focus on a decay channel for the particle in interest, look for those decay products in the detector (which do live long enough to be detected) and make an analysis based on the combination of these products to reconstruct the mother particle. This is called a final state analysis, and it is the approach that is used in this master thesis. The alternative is to do precision measurements of distributions that depend on the new particle, for instance as in Figure 2.8, which was discussed in Section 2.5.

There are different approaches as how to choose the basis for the analysis. One approach is to select a particular process through which your mother particle was produced, like for instance W, Z bremsstrahlung (see Figure 2.6), and/or final state, like for instance having the vector boson decay

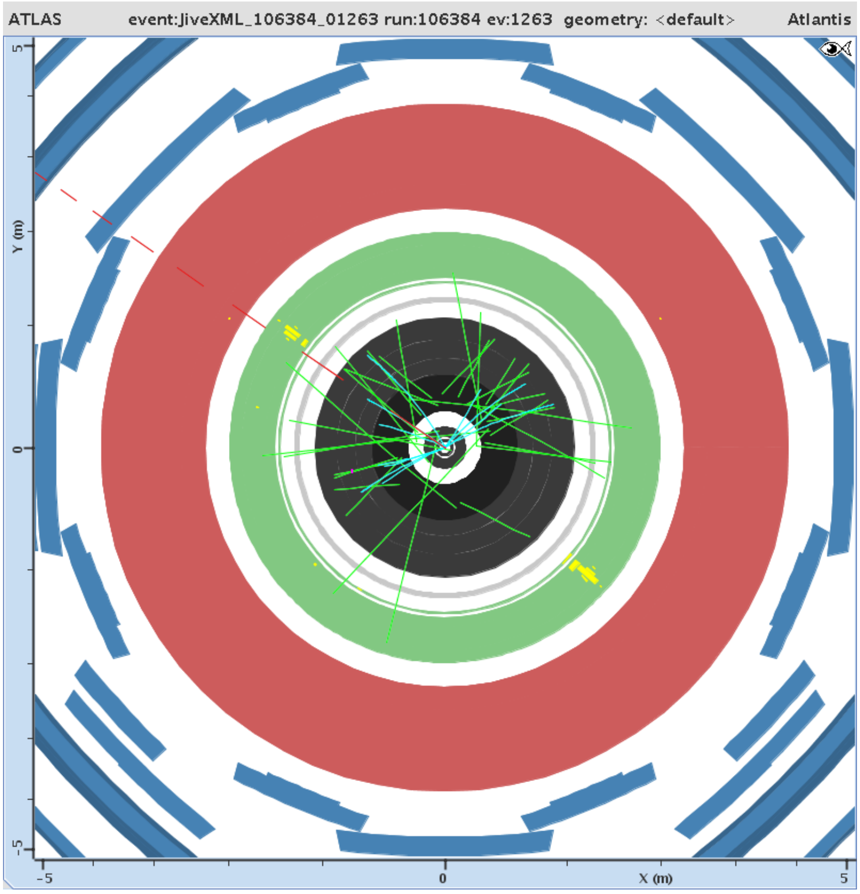

Figure 3.9: Simulated $H \rightarrow \gamma\gamma$ event in the ATLAS detector, displayed with Atlantis. The long, red, dotted line to the upper left represents missing transverse energy.

into some specific leptons. This is called an exclusive analysis. The advantage of an exclusive analysis is that the background of the decay channel is reduced, since there are some criteria (like for instance missing energy) for choosing the events of interest (that is, in addition to what the Higgs boson decayed into). The disadvantage is that, because the demands are so stringent, the rate of this happening is much lower than if all events in where the Higgs boson decayed in the chosen manner had been accepted. In addition, one is not open to include unexpected production mechanisms.

The other approach is to include all different production mechanisms (effectively, this is to say that one does not care about how the mother particle was created; one gladly accepts all one can get) and not to care so much about what the Higgs boson is accompanied by. In other words; the primary information used when selecting the events of interest is what the Higgs boson itself decayed into. This is called an inclusive analysis, and it is this approach that is used in this thesis. The advantage of an inclusive analysis is that unexpected production mechanisms can be picked up and that the rate of the decay is as large as possible (because there is no demand on anything else happening at the same time). The disadvantage is that the background is frequently much larger than in an exclusive analysis.

### 3.3.4 Trigger and Data Acquisition (DAQ)

The collisions in ATLAS will occur at a rate of 40 MHz (that is every 25 ns). Storing the amount of data corresponding to this rate would be completely impossible, and also uninteresting, given that the rare physics we are looking for does not happen that often. A selection of the interesting events must therefore take place, which means to reduce the rate of 40 MHz to $\sim$100 Hz, which corresponds to about 100 MB/s, for permanent storage. This is done by three levels of triggers; the Level-1 (LVL1) running in the pipelines of the detector electronics, the Level-2 (LVL2) and the Event Filter (EF) running as software filters on processor farms in the rack-room next to the detector [29]. The Level-2 trigger and the Event Filter are together called the High Level Trigger (HLT) [37].

$H \rightarrow \gamma\gamma$ has a cross-section times branching ratio ($\sigma$·BR) of the order of 10 fb in the mass range of interest (100 - 140 GeV/c$^2$), which means that there will be produced about 1000 Higgs events of this kind in a year of running at full luminosity[8]. For comparison, the inelastic cross-section is about 100 mb, that is $10^{14}$ fb, resulting in $10^{16}$ events of this kind per year of running at full luminosity [38]. To imagine picking out one event in a hundred billion events might be difficult to envision, it is no doubt that this is a great challenge. It is worth mentioning that the so-called minimum bias events come from the part of the total inelastic proton-proton collisions that are non-single diffractive, and have a cross-section of 65mb [39].

---

[8] The number of events of a specific process is given by $N = \mathcal{L}\sigma$, where N is number of events of the process with cross-section $\sigma$ and $\mathcal{L}$ is the integrated luminosity

# Chapter 4

# The $H \rightarrow \gamma\gamma$ Signal and Background

In this chapter, we will have a look at what defines our signal and what defines our background. First, we will have a look at the signal and then we will come to the background and how to get rid of parts of it (the parts of it we can get rid of).

“Background” is events in the data or simulation that imitate our signal - that is; it *looks* like our signal, but it really is not. This might for instance be the process of a quark and an anti-quark turning into two photons which by chance seem to come from the decay of a Higgs boson.

It is possible to divide the background of this channel into a reducible part, and an irreducible part. The background that it is possible to distinguish from our signal, is called reducible. As the word “reducible” describes - we are able to remove a lot of this background (while still keeping most of the signal) by applying appropriate cuts[1]. This kind of background consists of so-called “fake photons” - that is objects that are falsely identified as photons. This goes mostly for jets[2], and above all for $\pi^0$’s, which are created when quarks or gluons fragment. Other particles, as electrons, can also be misidentified as photons if reconstructed incorrectly. Thus, for an event to be a reducible background, it must contain at least one fake photon. Irreducible background, on the other hand, comes from processes with two real photons which are impossible to distinguish from our signal. These backgrounds together are predicted to be above the signal by eight orders of magnitude [40] before any cuts are made.

## 4.1 The Signal

The main feynman diagram for the signal of this analysis is included in Figure 4.1. A Higgs boson decaying into two photons has to go through a loop of massive particles (it does not couple directly to the photon, since the photon is massless). This loop will mostly consist of W-bosons, but also a

---

[1] A cut is a selection of events - you say that "I want events within these values of these parameters" and those events that are outside the chosen range are thrown away.

[2] A jet is a shower (seen as a cluster of hits in the detector) that mostly come from strongly interacting (QCD) objects. Quarks and gluons will be seen as jets in the detector; they will make bound systems, as they cannot be single objects (nature seems to require that all observable particles must be colorless), which will decay and together make up these jets. The $\tau$ lepton, mainly decaying hadronically, will thus also mainly be detected as a jet.

loop of top-quarks will give a contribution worthy of mentioning. Bosons in the loop contribute a factor about five to six more than fermions when the masses of the bosons and fermions are not so different from the Higgs mass [41]. Since the W and the top-quark are the heaviest object allowed in this loop, these two contributions will be the most important ones (remember that a ZZ$\gamma$-vertex is not permitted).

In Figure 4.2 a plot of the absolute value of the largest $\eta$ among the two photons for both the signal of a 120 GeV Higgs boson and the merged background, that is the contribution of all the background listed in Table 5.3 put together, can be seen. The plot is made with 14 TeV fully simulated data, and the only demand was that the event contained two photons. The crack region of $1.37 < |\eta| < 1.52$ is clearly visible.

In Figure 4.3 the p$_T$ of the hardest photon can be seen, both for a 120 GeV Higgs signal and the merged background. In Figure 4.4 the difference in p$_T$ of the two photons can be seen, both for 120 GeV Higgs signal and the merged background.

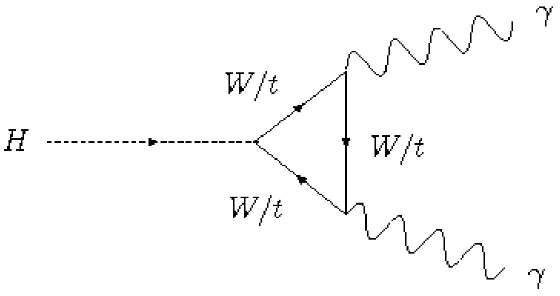

Figure 4.1: Dominant feynman diagrams for H$\rightarrow \gamma\gamma$.

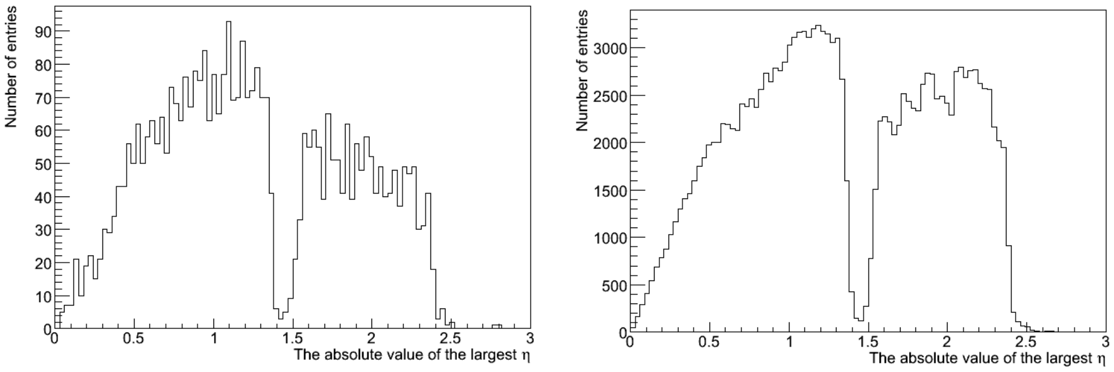

Figure 4.2: Plot of the absolute value of the largest $\eta$ among the two photons of the signal. To the left: for a signal of 120 GeV. To the right: for the merged background. Made using 14 TeV fully simulated data (unscaled).

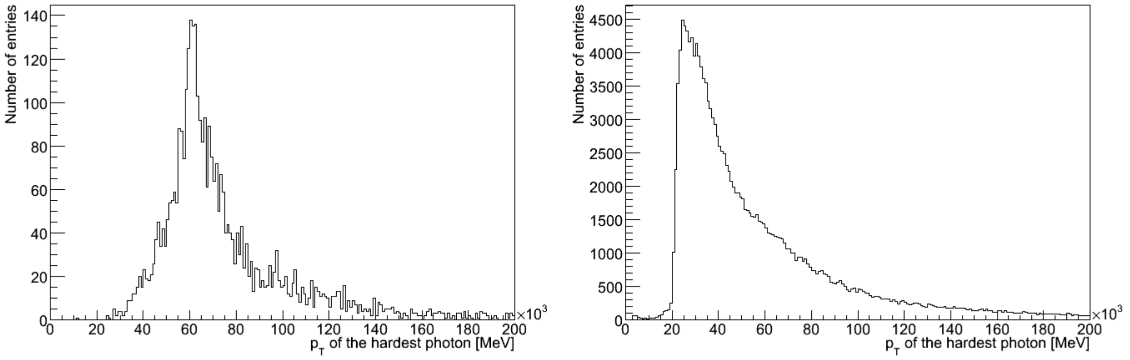

Figure 4.3: The $p_T$ of the hardest photon for the signal of a 120 GeV Higgs boson to the left, and for the merged background to the right. Made using 14 TeV fully simulated data (unscaled).

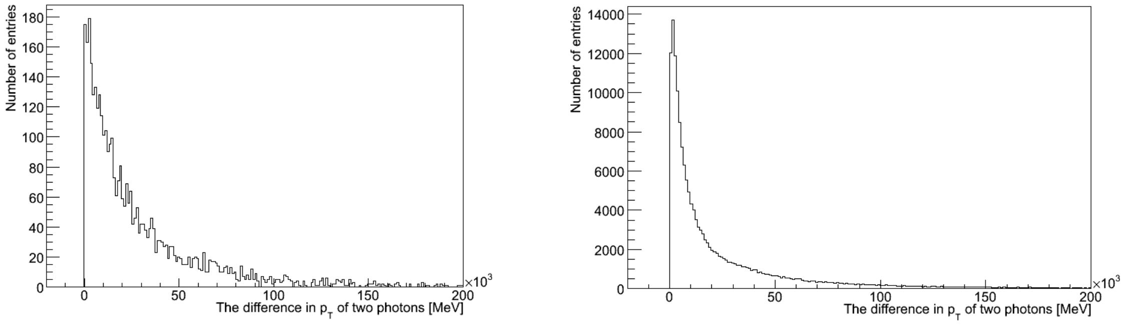

Figure 4.4: The difference in $p_T$ of the two photons for the signal of a 120 GeV Higgs boson to the left, and for the merged background to the right. Made using 14 TeV fully simulated data (unscaled).

### 4.1.1 Selecting the $\gamma\gamma$ Pair[3]

Moving to the experimental point of view, it must be said that the way the selection of the $\gamma\gamma$ pair is done has great importance, because this will have a great say in how much of the background is reconstructed as signal (through the fact that it decides what is labeled as a photon in the reconstruction). It is not the intention of this thesis to investigate or improve the selection of the photon pair, but merely to use the selections made from the ATLAS collaboration (which in practice means to use the Ntuples generated from these selection criteria).

#### Photon reconstruction and identification

What is essential in setting up the criteria for a photon candidate is the shape of the shower it makes - which gives the so-called shower-shape variables. The way true photons shower, and the way for instance $\pi^0$'s shower are (slightly) different, and we want to catch this difference so that we are able to assign the label "photon" to as many true photons and to as few non-photons as possible.

---

[3] This section is based on the ATLAS CSC note.

When reconstructing the photons in the calorimeters, different cluster sizes are used. The size of the cluster is given in $\Delta\eta \times \Delta\phi$, where the denomination is in units of middle sampling calorimeter cells. In the barrel region ($|\eta| < 1.37$), the cluster size used for unconverted photons is $3\times5$, and the cluster size for converted photons is $3\times7$. The reason that the cluster size for converted photons is bigger, is that the electron and the positron that the photon converts into open up (they move away from each other) in the inner detector, due to the magnetic field. In the end-cap region, both converted and unconverted photons are reconstructed using a cluster size of $5\times5$.

The shower-shape variables include (moving from the outer part of the detector towards the center):

- the leakage from the electromagnetic calorimeter to the first compartment of the hadronic calorimeter
- the lateral size of the shower (how broad it is) in the second layer of the electromagnetic calorimeter
- variables connected to the lateral size in the first layer of the electromagnetic calorimeter
- a search for a second maximum in $\eta$ in the energy deposited in the strips of the first layer of the electromagnetic calorimeter[4]

The average efficiency for these cuts are 83% for photons coming from a Higgs boson decay with $p_T > 25$ GeV, when pile-up corresponding to an instantaneous luminosity of $10^{33}\mathrm{cm}^2\mathrm{s}^{-1}$ (that is, a factor ten lower than the design luminosity) is added.

In addition to these cuts, a cut on the isolation of the photon is also added, further reducing the reducible background; the demand is that the sum of the $p_T$'s of the tracks in a cone of $\Delta$R=0.3 around the cluster position[5] is less than 4 GeV, only summing up tracks with $p_T > 1$ GeV. Additional cuts are applied to the tracks with $\Delta$R<0.1 of the cluster position, removing conversion tracks from the sum (if a track belongs to a *reconstructed* $e^+e^-$ pair, it is not included in the sum). This last cut has an efficiency of 98% for photons fulfilling all the other identification criteria. After all cuts, single $\pi^0$'s are the dominant source of background.

**Photon trigger**

For the $H \rightarrow \gamma\gamma$ channel, there are two triggers of interest; the 2g17i trigger and the g55 trigger. 2g17i is efficient for photons with $p_T > 20$ GeV and demands at least two isolated photons. This trigger is expected to be ~94% efficient for triggering on two photons coming from a Higgs boson decay, and is the one that was used in the CSC note analysis. In the g55 trigger, no isolation is required, but at least one photon is demanded. This trigger is efficient for photons with $p_T > 60$ GeV (in other words, it is marginal unless the mass of the Higgs boson is somewhat larger than 120 GeV). In this analysis, no trigger was used. This will not have a large impact on the results - as the 2g17i trigger (that would have been chosen) is so efficient, not a lot of events would have

---

[4] This is in order to separate photons from $\pi^0$'s, through the fact that $\pi^0$'s often have two maxima due to the $\pi^0 \rightarrow \gamma\gamma$ decay [42].

[5] $\Delta R = \sqrt{\Delta^2\eta + \Delta^2\phi}$, is distance in pseudorapidity-azimuthal angle space [29].

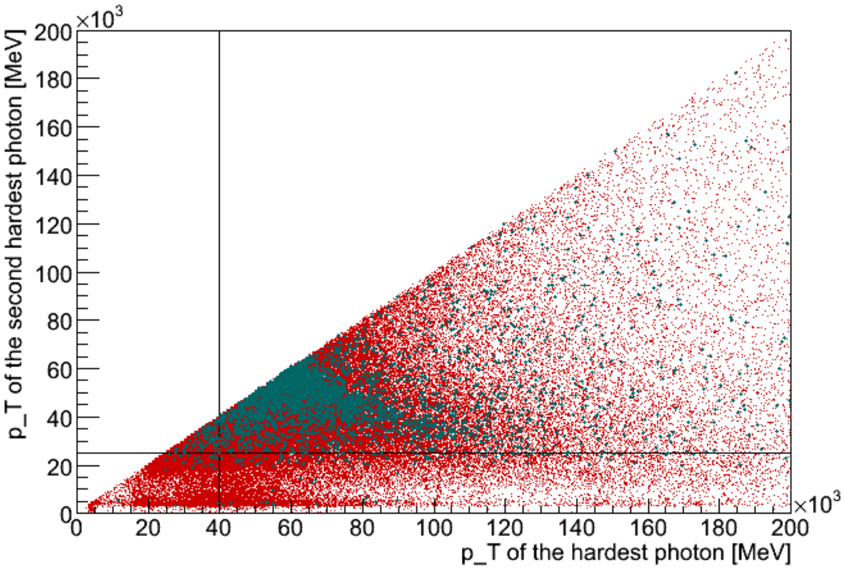

Figure 4.5: The $p_T$ of the second hardest photon versus the $p_T$ of the hardest photon. The distribution for a 120 GeV Higgs boson is shown in green, and for the merged background in red. The $p_T$ cuts of >40 GeV and >25 GeV are indicated by straight lines. Plotted using 14 TeV fully simulated data (background is unscaled). Please note that the marker size for the signal is larger than for the background, in order to make it more visible.

been lost due to trigger selections.

### The selection of the two photons

In the CSC note, the two photons selected had $p_T > 25$ GeV and $p_T > 40$ GeV, both were in the region $(0 < |\eta| < 1.37)$ , $(1.52 < |\eta| < 2.37)$ and passed the trigger and identification criteria described above[6]. The cuts in $p_T$ were found from an optimization study done earlier in the TDR ([29, 43]). These cuts were also applied in the analysis done in this thesis, see Figure 6.4 for the effect of these cuts on the 10 TeV fully simulated data.

In Figure 4.5, the $p_T$ of the second hardest photon versus the $p_T$ of the hardest photon both for a 120 GeV Higgs boson and for the merged background can be seen, where the $p_T$ cuts on the respective photons are indicated by straight lines. As can be seen, by doing these cuts a part of the background is removed while still keeping most of the signal. Doing an additional cut in large values of $p_T$ could also be considered, as the concentration of the signal is not too large at high values of $p_T$. A more complex cut of a -45° slope could be a clever one to make. However, one must keep in mind that this $p_T$ distribution of the signal is dependent on the mass of the Higgs boson (it can be seen in Figure 4.5 that the concentration of the signal of a 120 GeV Higgs is highest around a $p_T$ of 60 GeV for each of the two photons), so one must exercise caution not to specialize the cuts too much.

---

[6] Photons in the crack region are rejected. See Section 3.3.1 for more information on the crack region.

## 4.2 Reducible Background

Since the production cross-sections of the reducible background processes, mainly consisting of jets and $\pi^0$'s, are many orders of magnitude larger than the signal process, we need excellent rejection power of fake photons [43]. A rejection factor of about $10^4$ against single jets is needed in order to be able to see the signal [35]. For the same purpose, a rejection power against $\pi^0$ of about three is necessary, when having a 90% efficiency for identifying photons [29]. Reconstruction of photon conversions and electrons are also real challenges for the inner detector, since electrons have lost on average somewhere between 10% and 50% (depending on $|\eta|$) of their energy when they leave the SCT, and between 10% and 50% of photons have converted within the same region (keep in mind that electrons might be reconstructed as photons, and that photons might be lost in the reconstruction due to a conversion) [27]. After TDR ([29, 43]) the material budget in front of the presampler and the calorimeter has increased substantially, as mentioned in Chapter 3.3.1, degrading the energy sampling in the calorimeter and making more photons convert, so in all degrading the ability to reconstruct photons correctly.

Reconstructing tracks is important when trying to find out what happened in an event. The efficiency for track reconstruction is a function of pseudorapidity $\eta$ and of the transverse momentum $p_T$. The track reconstruction efficiency for pions is higher for more energetic pions going in the direction of $|\eta| \approx 0$ (straight upwards or straight downwards). For pions with $p_T$ = 1,5,100 GeV, the track reconstruction efficiency is respectively approximately 91.5%, 94.0% and 97.5% for $\eta \approx 0.1$, and approximately 77.5%, 83.0% and 89.5% for $\eta \approx 2.4$ [27].

The efficiency of identifying pions is a function of the energy of the pion. If the electron efficiency is 90%, the efficiency for identifying charged pions (using the TRT) is between $10^{-1} - 10^{-2}$ (that is somewhere between one in ten and one in a hundred) - it is higher for more energetic pions, because electrons emit more transition radiation than pions at higher energies and thus it is simpler to separate them from pions. Pion rejection factors above 50 are reached for 2-20 GeV (this decreases after 10 GeV, since the pions become more relativistic and therefore create more knock-on electrons which makes a charged pion look like an electron) [27]. The expected electron-pion separation is a function of $\eta$. For electrons with $p_T$ of 25 GeV, the efficiency for identifying pions is about $7 \cdot 10^{-2}$ for $\eta \approx 0.1$ and about $5 \cdot 10^{-3}$ for $\eta \approx 1.7$ when requiring an electron identification efficiency of 90% [27].

As mentioned earlier, reconstructing photon conversions is a challenge. The efficiency for reconstructing a conversion of a photon with $p_T = 20$ GeV and $|\eta| < 2.1$ is about 80% when the conversion took place at a radius of 25 mm, and about 95% when the conversion radius was 100 mm [27]. The efficiency is dependent on the ability to reconstruct the vertex and the ability to identify single-track conversions (when only one of the tracks coming from the electrons in the inner detector is reconstructed).

In addition to jets, a small background contribution is predicted to come from the Drell-Yan[7] production of $e^+e^-$, faking a photon pair. It was not included as one of the backgrounds in this

---

[7] The Drell-Yan process is the production of a lepton-antilepton pair from the scattering of two hadrons, through a electromagnetic or weak interaction. Two of the quarks in the hadrons collide to make the lepton-antilepton pair, and the rest of the quarks can make up any hadronic final state [9].

thesis. There is also a contribution from events with a photon and a W, where the W decays into an electron and a neutrino, and the electron is mis-identified as a photon [1]. This contribution was not included in the analysis, as datasets of this process did not exist. A contribution from a Z boson decaying leptonically (into two neutrinos or to charged leptons), and that of a W boson decaying leptonically (into a neutrino and a charged lepton), being in the same event as two photons was included in the analysis done with the 14 TeV datasets. They were not available among the 10 TeV simulated data, but this is not critical, as the contribution from these datasets is minuscule (see Table 6.6 last column for the number of events passing all the CSC cuts, scaled). These backgrounds are of greater importance when an exclusive analysis with associated production including W, Z is studied, in which a lepton or missing transverse energy is demanded.

### 4.2.1 Reducing the Reducible Background

In order to be able to reduce this background, an excellent photon identification ability is needed - it is crucial to be able to tell what really are photons, and what merely looks like photons, but really are not. We are therefore very dependent on the resolution of the electromagnetic calorimeter. A fine segmentation is needed in order to be able to tell the $\pi^0$'s (which is, as mentioned, the main source of the fake photons from jets) from the real photons. This is, because $\pi^0$'s mainly decay into two photons. The separation between these two photons coming from a $\pi^0$ might be too small for the calorimeter to separate (if the $\pi^0$ has a high energy, the Lorentz-boost would cause the photons to have a small opening angle) - it would then look like one photon with accordingly higher energy than the two real photons. $\pi^0 \rightarrow \gamma\gamma$ was one of the benchmark processes for the electromagnetic calorimeter, putting demands on the granularity - in other words, the electromagnetic calorimeter was built with the segmentation it has in order to be able to separate the two photons coming from a $\pi^0$. When considering the $\pi^0$, the probability of having a shower started early in the electromagnetic calorimeter is twice as big as when considering a photon - simply because in the $\pi^0 \rightarrow \gamma\gamma$ decay, there are *two* photons. The ATLAS detector is able to separate $\pi^0$'s with $p_T =$ 50 GeV from photons with $p_T =$ 50 GeV - for a photon efficiency of 90%, the $\pi^0$ rejection at this transverse momenta is about three (depending on the $\eta$) [30].

## 4.3 Irreducible Background

In the irreducible department, there are three processes; $gg \rightarrow \gamma\gamma$ (Box process), $q\bar{q} \rightarrow \gamma\gamma$ (Born process) and $qg \rightarrow \gamma\gamma q$ (Bremsstrahlung process). See Figure 4.6 for the feynman diagrams of these processes. This last mentioned contribution coming from quark bremsstrahlung is not fully irreducible - since the softest of the two photons is produced close to a jet (coming from the quark that fragments), we can put an isolation cut on this. If we add a requirement that there is no more than 15 GeV in a cone of $\Delta$R=0.7 around the photon , the quark bremsstrahlung contribution will be reduced to be around 50% of the sum of the Born and Box contributions [40]. This was not done in this analysis, as there were more pressing matters to be handled.

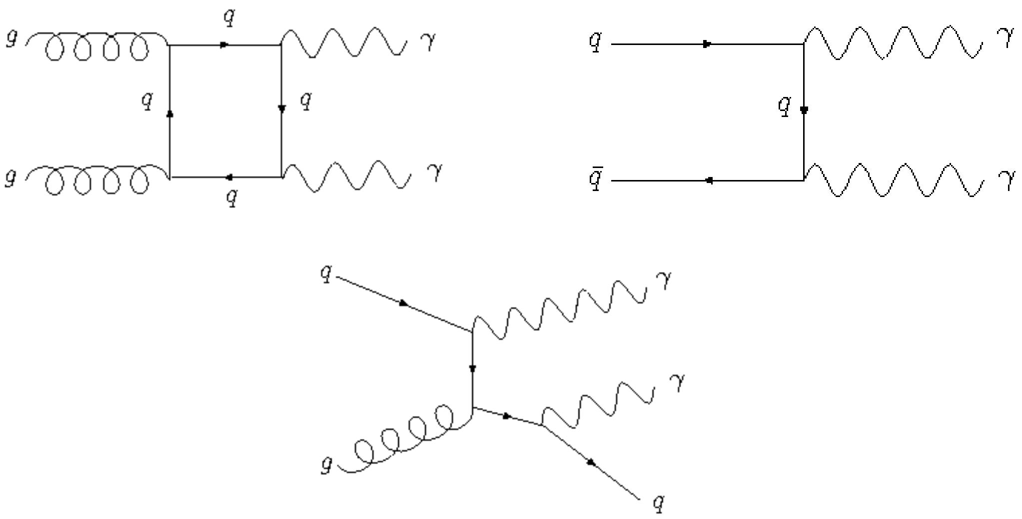

Figure 4.6: Upper: Irreducible background; feynman diagrams of the Box (left) process and the Born (right) process. Lower: Semi-irreducible background; feynman diagram of the Bremsstrahlung process.

# Chapter 5

# Working On Simulated Data

As the LHC has as of yet not delivered colliding beams data, the analysis must be done on Monte Carlo simulated data. We will now have a very brief look at how the structure of generating and working on simulated data is built up, and list the basic information about the datasets used in this study.

## 5.1 From Raw Data to Analysis Data Format

From our detector, raw data, digital information in form of zeros and ones, is collected. In order to do a realistic imitation and preparation for when real data is coming, this must be produced. The creation of events is done with so-called event generators. The output of an event generator is a data format which is called EVNT. The EVNT files are input to simulation of the detector and the digitization of the samples. The raw data files after this stage are large and fairly unmanageable. A reduction of the information must be done - it is impractical to do an analysis based on digitalized signals from the detector, in the end physical objects like photons and jets are desired. The reconstruction software applied at this stage is the same as which will be applied to the real data coming from the detector. The course of the data format is as follows: EVNT, RDO (Reduced Data Object), ESD (Event Summary Data), AOD (Analysis Object Data) and Ntuples, where the last format is what the analysis finally is carried through with. The Athena Framework takes care of reducing the RDO’s to ESD’s, the ESD’s to AOD’s, and AOD’s to Ntuples. With fast simulations (ATLFAST), one can jump directly from EVNT to AOD, taking only average values of the effect the detector has on different particles. This gives a larger uncertainty in the results obtained, compared to using fully simulated data.

## 5.2 Generating Simulated Data

This section is based on Les Houches Guidebook to Monte Carlo Generators for Hadron Collider Physics written by H. Baer et al. [44].

So, first of all, the events must be created using event generators like for instance PYTHIA [45], AlpGEN [46] and MadGraph [47]. It is possible to combine the output from different generators, as the generators are specialized in producing different processes. To take the already mentioned generators; PYTHIA is a general purpose generator for hadronic events in proton-proton (pp), electron-positron ($e^+e^-$) or electron-proton (ep) collisions, AlpGEN is designed for generating SM processes in hadronic collisions with emphasis of events with large jet multiplicity in the final state and finally MadGraph is a matrix element generator for SM processes at any collider, it calculates the amplitudes for all the relevant subprocesses and may be used in combination with another generator.

The events that were used as a basis for the Ntuples used in this analysis were generated with the help of the computer program PYTHIA. Included in PYTHIA is a subprocess library at leading order (LO), initial and final state parton showers at leading-log (LL), but also with many next-to-leading-log (NLL) aspects (such as energy conservation), underlying event (due to that protons are not elementary particles, more than one parton-parton interaction may take place), hadronization[1] and decays, analysis tools and, logically enough (given that it is a generator); a generation machinery.

When the event is generated, the particles in the event must be "sent" through the detector - the Athena Framework take cares of this - it implements the interaction of the particles with the detector, the detector response and the detector geometry itself, by using the program GEANT4 [48, 49]. The reconstruction from the digital information the particles leave in the detector is carried through, which means to use algorithms for finding what most probably took place - such as finding the most likely tracks and showers. When Athena is finished doing it's job, the datasets it has produced will hopefully represent the realistic outcome of our process in the detector, what is expected to be seen when the LHC is switched on. Athena produces Analysis Object Data (AOD), but can also be reused to produce Ntuples through specialized codes for the different working groups. In the case of this analysis the Athena package HiggsAnalysisUtils of the HiggsToGammaGamma working group has been used to produce the Ntuples with which the analysis was carried through.

## 5.3 Ntuples Used in this Study

In this thesis, both a study using 10 TeV fully simulated data and 14 TeV fully simulated data was carried through. In this respect, we try to go beyond the fast simulation studies published by the ATLAS Higgs group in the CSC note [1]. As mentioned in the introduction, it is not yet decided whether the LHC will start up at a center of mass energy of 10 TeV, or go directly to full 14 TeV collisions.

Please note that the Ntuples used in this analysis are of varying origin with respect to Athena release and detector geometry. That means that the Ntuples were created with different descriptions of the detector, and generated with different releases of Athena. This is because it was simply not

---

[1] To make colorless objects out of strongly interacting particles.

| Process | Dataset name | Generator | Cross-section [nb] |
|---|---|---|---|
| H->gamgam (gg+VBF) | *H120* | Pythia | 0.0000352799 |
| diphotons (MSTP68=1) | *gamgam* | Pythia | 0.934449 |
| dijets J0 (8-17GeV) | *J0* | Pythia | 11698200 |
| dijets J1 (17-35GeV) | *J1* | Pythia | 863605 |
| dijets J2 (35-70GeV) | *J2* | Pythia | 56013.3 |
| dijets J3 (70-140GeV) | *J3* | Pythia | 3286.72 |
| dijets J4 (140-280GeV) | *J4* | Pythia | 151.61 |
| gamma+jet 1 (17-35GeV) | *PhotonJet1* | Pythia | 199.056 |
| gamma+jet 2 (35-70GeV) | *PhotonJet2* | Pythia | 19.1778 |
| gamma+jet 3 (70-140GeV) | *PhotonJet3* | Pythia | 1.65284 |
| gamma+jet 4 (140-280GeV) | *PhotonJet4* | Pythia | 0.11444 |

Table 5.1: Information for 10 TeV datasets using full simulation. Cross-sections found through ATLAS Metadata Interface (AMI) [50].

| Process | Dataset name | Higgs mass [GeV] | Generator | Cross-section [fb] |
|---|---|---|---|---|
| H->gamgam (gg+VBF) | *H110* | 110 | Pythia | 65.3 |
| H->gamgam (gg+VBF) | *H120* | 120 | Pythia | 64.3 |
| H->gamgam (gg+VBF) | *H130* | 130 | Pythia | 56.4 |
| H->gamgam (gg+VBF) | *H140* | 140 | Pythia | 41.8 |
| H->gamgam (gg+VBF) | *H200* | 200 | Pythia | 0.618 |

Table 5.2: Information for 14 TeV signal datasets using full simulation.

practically possible to obtain a consistent dataset.

Table 5.1 (in which case there were only signal datasets for a Higgs mass of 120 GeV) lists information about the signal and background datasets used in the 10 TeV study, together with their respective cross-sections. The same information for the datasets of the 14 TeV study can be seen in Tables 5.2 and 5.3. Please note that "gg" stands for gluon-gluon fusion, and "VBF" for Vector Boson Fusion (see section 2.4 for more details on production mechanisms). The entries in the “Dataset name” column will be what is used to indicate the different backgrounds throughout the rest of this thesis. The *gamgam* dataset contains the irreducible background, as described in Section 4.3. The datasets *J0*, *J1*, *J2*, *J3* and *J4* are di-jet backgrounds of different $\sum p_T$ and *PhotonJet1*, *PhotonJet2*, *PhotonJet3*, *PhotonJet4* are $\gamma$-jet backgrounds of different $\sum p_T$. The dataset *AAj* contains two photons and one jet, the *WplAA_lnu*/*WminAA_lnu* datasets are $W^+ \rightarrow l\nu/W^- \rightarrow l\nu$ being in the same event as two photons. Finally, the *ZAA_ll*/*ZAA_nunu* datasets are $Z^0 \rightarrow ll/Z^0 \rightarrow \nu\nu$ being in the same event as two photons.

| Process | Dataset name | Generator | Cross-section [nb] |
|---|---|---|---|
| diphotons (MSTP68=1) | *gamgam* | Pythia | 0.166 |
| diphotons+1jet | *AAj* | MadGraph/Pythia | 0.00702 |
| dijets J0 (8-17GeV) | *J0* | Pythia | 17436300 |
| dijets J1 (17-35GeV) | *J1* | Pythia | 1386760 |
| dijets J2 (35-70GeV) | *J2* | Pythia | 97090.6 |
| dijets J3 (70-140GeV) | *J3* | Pythia | 6121.69 |
| dijets J4 (140-280GeV) | *J4* | Pythia | 316.471 |
| gamma+jet 1 (17-35GeV) | *PhotonJet1* | Pythia | 261.782 |
| gamma+jet 2 (35-70GeV) | *PhotonJet2* | Pythia | 27.2374 |
| gamma+jet 3 (70-140GeV) | *PhotonJet3* | Pythia | 2.56447 |
| gamma+jet 4 (140-280GeV) | *PhotonJet4* | Pythia | 0.197719 |
| W+(->ln)+diphotons | *WplAA_lnu* | MadGraph/Pythia | 0.000003334 |
| W-(->ln)+diphotons | *WminAA_lnu* | MadGraph/Pythia | 0.000003092 |
| Z(->ll)+diphotons | *ZAA_ll* | MadGraph/Pythia | 0.000002443 |
| Z(->nn)+diphotons | *ZAA_nunu* | MadGraph/Pythia | 0.000004865 |

Table 5.3: Information for 14 TeV background datasets using full simulation.

# Chapter 6

# The Analysis

In this chapter it will firstly be shown that a fit of the full sum of all the background together with the signal cannot be made, due to poor statistics (and thus large scaling factors) of the background samples. Then, we will move on to the motivation for separating the signal and background, and a search for a parameter plane in which this is fulfilled. Moving along, the search made for such a parameter plane will be discussed, before a description of the parameter plane chosen for this analysis is presented. Furthermore, a discussion of the effect of this parameter plane on the different backgrounds and signals of different masses will be made. Finally, fits of the signal alone, two of the backgrounds alone as well as the signal together with the irreducible (*gamgam*) background will be made. Please note that all plots were made with 30 $\text{fb}^{-1}$.

As mentioned in the introduction, it is also possible to separate the analysis into different regions (which could be called categories) according to pseudorapidity, $\eta$ - different regions of pseudorapidity have different resolution on the diphoton invariant mass, $m_{\gamma\gamma}$, so a division of this kind would lead to a higher sensitivity to the result (in this way, one does not mix broad and narrow peaks together). This approach has been used in the CSC note [1], but due to limited time, it will as mentioned earlier not be a part of this thesis.

## 6.1 The Limitation of Full Simulation and the Effect of the CSC cuts

It was impossible to make a fit of the sum of the background and the signal when using full simulation of the detector description. This is because processes such as jet events containing two photons are very rare, thus an enormous amount of events must be generated in order to get a large enough (corresponding to the cross-section this processes have) number of events of this kind, which is not practically possible as of today.

The impossibility of a merged background and signal fit is displayed in Figure 6.1 (for 10 TeV) and Figure 6.3 (for 14 TeV) - the statistics using full simulation were plainly awful. In Figure 6.2, it is zoomed in on the invariant mass distribution of the 10 TeV simulation, to compare the shape of the distribution with the one for 14 TeV simulation, which looks fairly similar. The cross-sections and the corresponding scaling factors for the different datasets used when creating of these plots can be seen in Table 6.1 for 10 TeV and in Table 6.2 for 14 TeV. The appallingly high scale factors come from the fact that the processes corresponding to these large scale factors have large cross sections - and since there is a limited amount of events generated for these processes in the dataset samples, they need to be scaled up to fit the luminosity decided for these plots (which is 30 $\text{fb}^{-1}$). With a scale factor of $10^{10}$, one generated event will correspond to ten billion events in the histograms. Thus, small fluctuations in the dataset will give an enormous effect in the plotted distribution. Because of this, there are great uncertainties of the plots such that a statement about the outcome is impossible to make. Please see Appendix B for the invariant mass distributions for separate datasets adding on the different CSC cuts, as well as the invariant mass distributions in different regions of the '$p_{\text{tmiss}}$ versus $\Delta\phi$'-plane (see section 6.2.2).

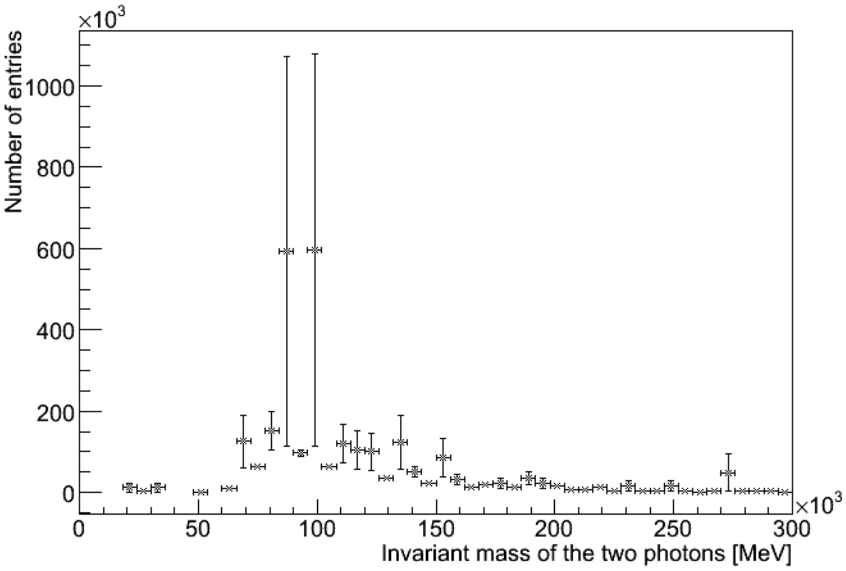

Figure 6.1: Invariant mass plot for events passing all the CSC cuts, using 10 TeV full simulation data with 30 $\text{fb}^{-1}$, for a Higgs boson at 120 GeV together with the merged background, indicating far too low statistics, demanding scale factors of horrible size, see Table 6.1.

| Dataset | Cross-section [nb] | Scale factor |
|---|---|---|
| *H120* | $3.527990 \cdot 10^{-5}$ | 0.2645993 |
| *gamgam* | 0.9344490 | 4672.245 |
| *J0* | $1.169820 \cdot 10^{7}$ | $5.849100 \cdot 10^{10}$ |
| *J1* | $8.636050 \cdot 10^{5}$ | $4.318025 \cdot 10^{9}$ |
| *J2* | $5.601330 \cdot 10^{4}$ | $2.800665 \cdot 10^{8}$ |
| *J3* | 3286.720 | $1.643360 \cdot 10^{7}$ |
| *J4* | 151.6100 | $7.580500 \cdot 10^{5}$ |
| *PhotonJet1* | 199.0560 | $9.952800 \cdot 10^{5}$ |
| *PhotonJet2* | 19.17780 | $9.588900 \cdot 10^{4}$ |
| *PhotonJet3* | 1.652840 | 8264.200 |
| *PhotonJet4* | 0.1144400 | 572.2000 |

Table 6.1: Table showing the cross-sections and scaling factors for the different datasets, using 10 TeV fully simulated data and 30 $\text{fb}^{-1}$. This table corresponds to Figures 6.1 and 6.2.

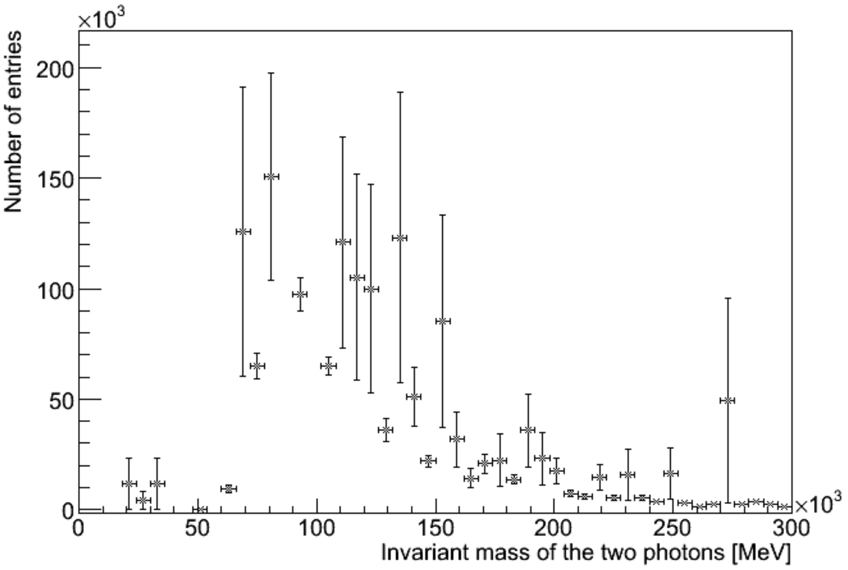

Figure 6.2: Same plot as Figure 6.1, only zoomed in on the y-axis to see the shape of the invariant mass distribution, which is similar to the one for the 14 TeV fully simulated data as shown in Figure 6.3.

The effect of the different CSC cuts is displayed in Figure 6.4 for 10 TeV fully simulated data, adding one more cut for each histogram when moving to the right. This same effect, given in numbers, is shown in Table 6.3, where the unscaled number of events in the datasets for 10 TeV full simulations can be seen, adding on one more cut for each column moved to the right. Thus, the numbers in the rightmost column is the number of events passing the CSC cuts. The same table with scaling can be seen in Table 6.4. The scaling is done using the numbers in Table 6.1. The two identical tables for the 14 TeV full simulations can be seen in Table 6.5 and 6.6, the latter one being the scaled table. The scaling is done using the numbers in Table 6.2. Looking at Table 6.5 and Table 6.3 we can extract that out of all the signal events generated, both for 14 TeV and for 10 TeV, approximately one out of four events has more than one photon ($\frac{9017}{20700} \approx \frac{1622}{4000} \approx \frac{1}{4}$).

## 6.2 Separating Background and Signal

We want to separate the background and the signal. There are two motivations for doing this. One of the motivations is to be able to carry out a data driven analysis - we want to base the analysis on real data, so that we do not have to trust the MC simulations, and so that we are unbiased from looking for the signal. These two points of a data-driven analysis will shortly be addressed. The other motivation is to find a signal-enriched region, which means to improve the background rejection. This last point is not the main focus of this thesis, but comes as a bonus.

To the first point of the motivation of a data driven analysis: We cannot blindly trust the MC simulations, because we do not know whether the description of the detector and the background are correct. In addition, the efficiencies, background rejection factors, $e^+e^-$ conversion probability and mass resolution etc. could easily be wrong. Separating the background and signal enables a

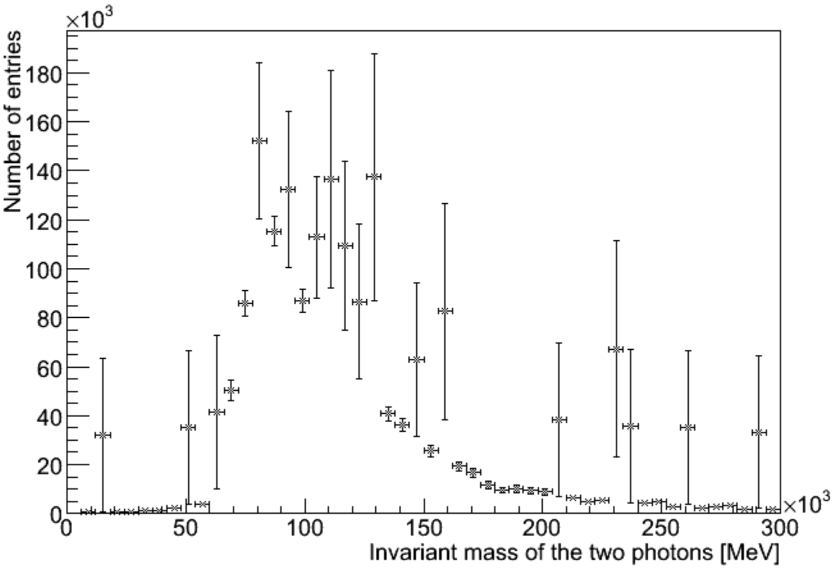

Figure 6.3: Invariant mass plot for events passing all the CSC cuts, using 14 TeV full simulation data with 30 fb$^{-1}$, for a Higgs boson at 120 GeV together with the merged background, indicating far too low statistics, demanding scale factors of horrible size, see Table 6.2.

study of the background alone, so it is possible to make sure that the background and the detector response is fully understood. After having understood the background, we are in good shape to add on regions that contain the signal, and to say something firmer about what happens as a consequence of this. If deviations from the regions containing only background are seen, it is possible to make a firmer statement about that this is not merely due to a poor understanding of the detector and/or the background itself - we are able to make a stronger statement about what we are seeing.

To the second point of the motivation of a data driven analysis: when one knows what one is looking for, it is easy to fall into the trap of twisting the analysis and the search in order to find what is desired, even subconsciously. For instance, one might choose cuts which pick out background events that meet somebody's expectation of the Higgs mass. By doing a data driven analysis on the background before looking for the signal, one can prevent this from happening.

The other motivation for separating the background and the signal is as previously mentioned to find a signal-enriched region. If one does find a region which is background-enriched, then one knows that the complementary region is signal-enriched, which is very pleasant, since there is not too much of this signal in the first place. The goal is to reduce the effect of the background on the uncertainty of the result to a minimum.

Now, what is important when finding these kinds of regions, where the background and signal are separated, is that they must be independent of the mass of the Higgs boson - simply because the mass of the Higgs boson is unknown. So what is done, is to look for parameter planes where this criteria of a mass-independent separation of the background and the signal is fulfilled, and then it is checked whether the choice of region distorts the distributions (a distortion of the distributions

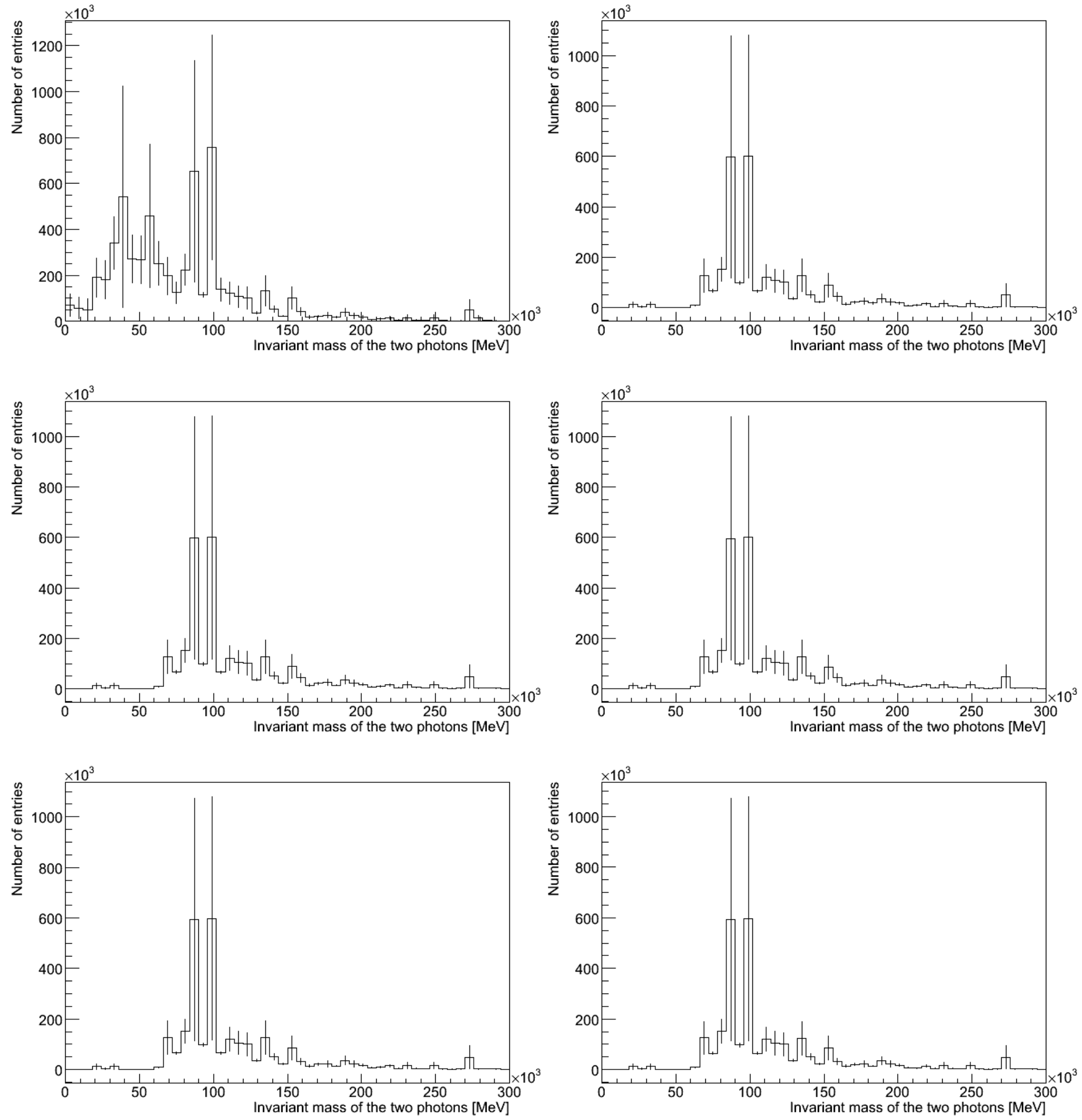

Figure 6.4: The effect of the different cuts on the two photons on the invariant mass calculation, adding one more cut for each histogram when moving to the right, from the top to the bottom. The histograms are made with a signal of 120 GeV together with the merged background, run with 10 TeV fully simulated data. Topmost left to right: with 40 GeV cut on $p_T$, added 25 GeV cut on $p_T$. Middle left to right: added $|\eta|_{\gamma_1} < 2.37$, added $|\eta|_{\gamma_2} < 2.37$. Bottommost left to right: added $|\eta|_{\gamma_1} < 1.37$ or $|\eta|_{\gamma_1} > 1.52$ and at last added $|\eta|_{\gamma_2} < 1.37$ or $|\eta|_{\gamma_2} > 1.52$.

| Dataset | Cross-section [nb] | Scale factor |
|---|---|---|
| *H110* | $6.530000 \cdot 10^{-5}$ | $9.463768 \cdot 10^{-2}$ |
| *H120* | $6.430000 \cdot 10^{-5}$ | $2.085405 \cdot 10^{-1}$ |
| *H130* | $5.640000 \cdot 10^{-5}$ | $1.504000 \cdot 10^{-1}$ |
| *H140* | $4.180000 \cdot 10^{-5}$ | $9.464151 \cdot 10^{-2}$ |
| *H200* | $6.180000 \cdot 10^{-7}$ | $4.120000 \cdot 10^{-3}$ |
| *gamgam* | $1.660000 \cdot 10^{-1}$ | 1.724675 |
| *AAj* | $7.020000 \cdot 10^{-3}$ | 4.258847 |
| *J0* | $1.743630 \cdot 10^{7}$ | $2.963677 \cdot 10^{9}$ |
| *J1* | $1.386760 \cdot 10^{6}$ | $2.178157 \cdot 10^{8}$ |
| *J2* | $9.709060 \cdot 10^{4}$ | $3.498760 \cdot 10^{7}$ |
| *J3* | $6.121690 \cdot 10^{3}$ | $2.138557 \cdot 10^{6}$ |
| *J4* | $3.164710 \cdot 10^{2}$ | $3.129245 \cdot 10^{4}$ |
| *PhotonJet1* | $2.617820 \cdot 10^{2}$ | $2.429907 \cdot 10^{4}$ |
| *PhotonJet2* | $2.723740 \cdot 10^{1}$ | $5.043963 \cdot 10^{2}$ |
| *PhotonJet3* | 2.564470 | $2.625289 \cdot 10^{2}$ |
| *PhotonJet4* | $1.977190 \cdot 10^{-1}$ | $2.185545 \cdot 10^{1}$ |
| *WplAA_lnu* | $3.334000 \cdot 10^{-6}$ | $3.746067 \cdot 10^{-3}$ |
| *WminAA_lnu* | $3.092000 \cdot 10^{-6}$ | $2.457219 \cdot 10^{-3}$ |
| *ZAA_ll* | $2.443000 \cdot 10^{-6}$ | $4.886000 \cdot 10^{-3}$ |
| *ZAA_nunu* | $4.865000 \cdot 10^{-6}$ | $9.730000 \cdot 10^{-3}$ |

Table 6.2: Table showing the cross-sections and scaling factors for the different datasets, using 14 TeV fully simulated data and 30 fb$^{-1}$. This table matches Figure 6.3.

is of course not desired).

The CSC note has not mentioned this focus on data driven analysis and finding parameter planes in which the background and the signal are separated, so finding such a plane would be a supplement to the analysis the ATLAS collaboration did for this note.

The work of finding these planes is non-trivial - a lot of different parameters plotted against each other were tried out, and parameters were invented before something that looked promising emerged. Some plots on the way of finding parameter planes with the desired properties will now be shown.

### 6.2.1 The Search for Parameter Planes separating Signal and Background

If the Higgs boson is created at rest with respect to the z-direction, then

$$\eta_1 + \eta_2 = 0.$$

Plotting these two variables against each other, the expected result is a straight line with a $-45^\circ$ slope if the Higgs was produced at rest in the z-direction. If the Higgs was boosted in the z-direction, this line is expected to be smudged out in the $\eta_2 = \eta_1 + constant$ (or $+45^\circ$ diagonal) direction when looping over a lot of such events with different z-boosts. See Figure 6.5 for the p$_z$

of Higgs from the truth-information in the Ntuples. As we can see from the left plot in Figure 6.6 (Figure 6.7 for scaled version), the distribution is very broad, but broader along the $+45°$ diagonal than along the - 45° diagonal. To explain; if the Higgs boson is boosted in positive z-direction, both the $\eta$'s will tend to be positive, and if Higgs is boosted in negative z-direction, both the $\eta$'s will tend to be negative. The plot to the right is made looping only over a 120 GeV signal. We can extract a relatively signal free area at $(\eta_1 \sim 2, \eta_2 \sim -2)$ and $(\eta_1 \sim -2, \eta_2 \sim 2)$, which could be of interest. However, we decided not to use this parameter plane, as the background has an equally broad distribution and a deficit in the same corners, as can be seen in the right plot of Figure 6.6.

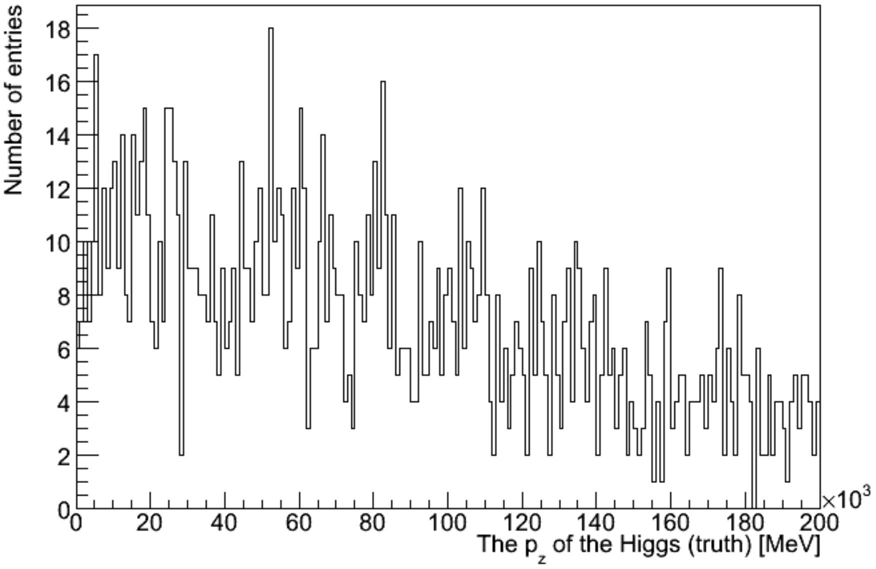

Figure 6.5: The $p_z$ of a Higgs boson of 120 GeV, from the truth information in the Ntuples.

A plot of the $\eta_1 - \eta_2$ versus the sum of the $p_z$ of the two photons was made, with the hope of a separation of the signal and the background. The result, for a 120 GeV Higgs boson to the left, and for the merged background to the right can be seen in Figure 6.8. As can be seen, this turned

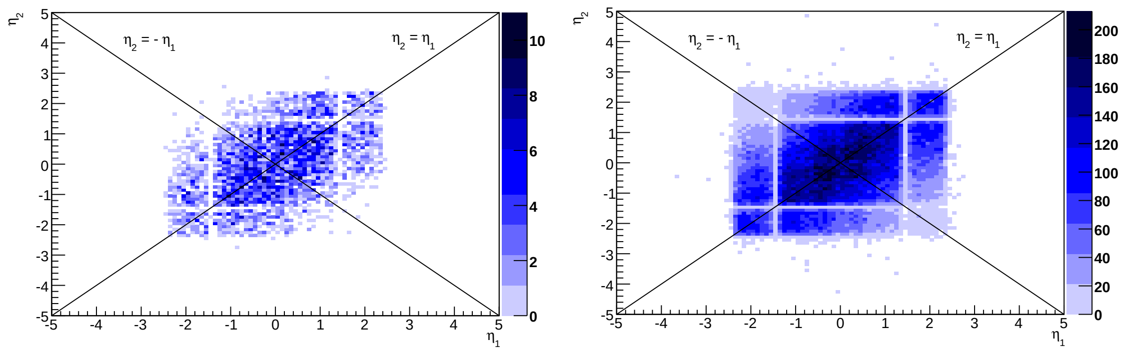

Figure 6.6: $\eta$ of one of the photons versus $\eta$ of the second photon. To the left; for the signal. To the right; for the merged background. Made using 14 TeV fully simulated data (unscaled).

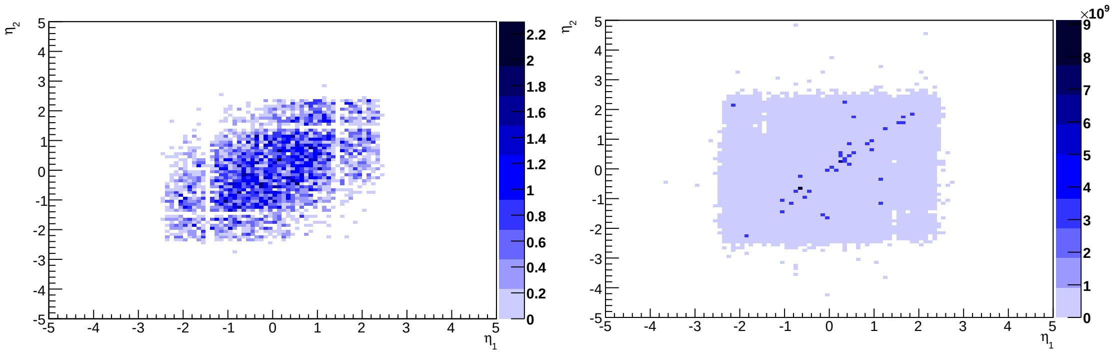

Figure 6.7: $\eta$ of one of the photons versus $\eta$ of the second photon. To the left; for the signal. To the right; for the merged background. Made using 14 TeV fully simulated data (scaled).

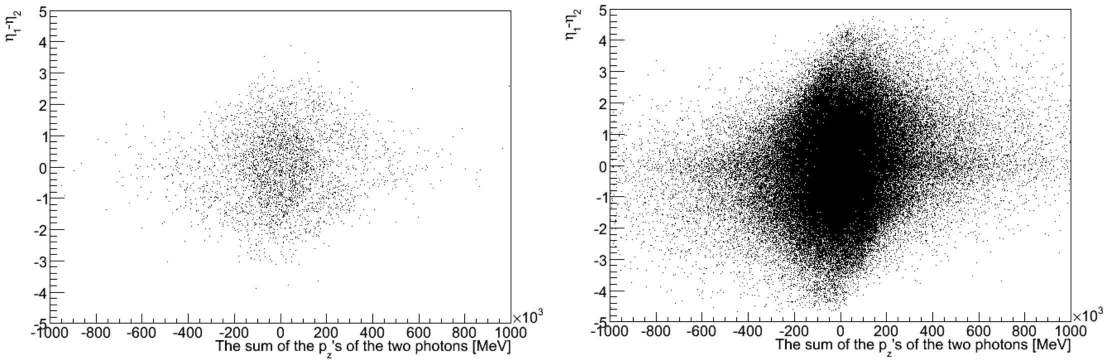

Figure 6.8: $\eta_1 - \eta_2$ versus the sum of the $p_z$ of the two photons. To the left; for the signal of a 120 GeV Higgs. To the right; for the merged background. Made using 14 TeV fully simulated data (unscaled).

out not to be of any use in a signal/background separation. In Figure 6.9 a collection of other strange-looking plots from our playing with the different variables which didn't give anything we could use further are shown, just to give a feeling of the game.

One of the parameter planes that looked promising, was the '$\eta_1 + \eta_2$ versus $p_{z1}+p_{z2}$'-plane. In Figure 6.10 this parameter plane is plotted both for a signal of a 120 GeV Higgs boson (to the left) and for the merged background (to the right), using 14 TeV fully simulated data. What is interesting to note, is that there seems to be two different slopes or structures in the plot of the background. If this really is the case, then it would render possible a measurement of the different background contributions against each other. This is something to look further into.

The profile plot of the $\eta_1 + \eta_2$ versus $p_{z1}+p_{z2}$ distribution can be seen in Figure 6.11, for the Higgs masses 110 GeV, 140 GeV and 200 GeV to the left and for a 120 GeV Higgs boson and the merged background to the right. The Higgs masses 120 GeV and 130 GeV are left out in the plot to the left for clarity, but lie in between the 110 GeV slope and the 140 GeV slope. The first mentioned of these two plots shows that the distribution is not completely independent of the Higgs boson mass. The second mentioned plot shows that there is a slope discrepancy between the 120 GeV Higgs boson signal and the merged background, but it is unlikely that this is enough

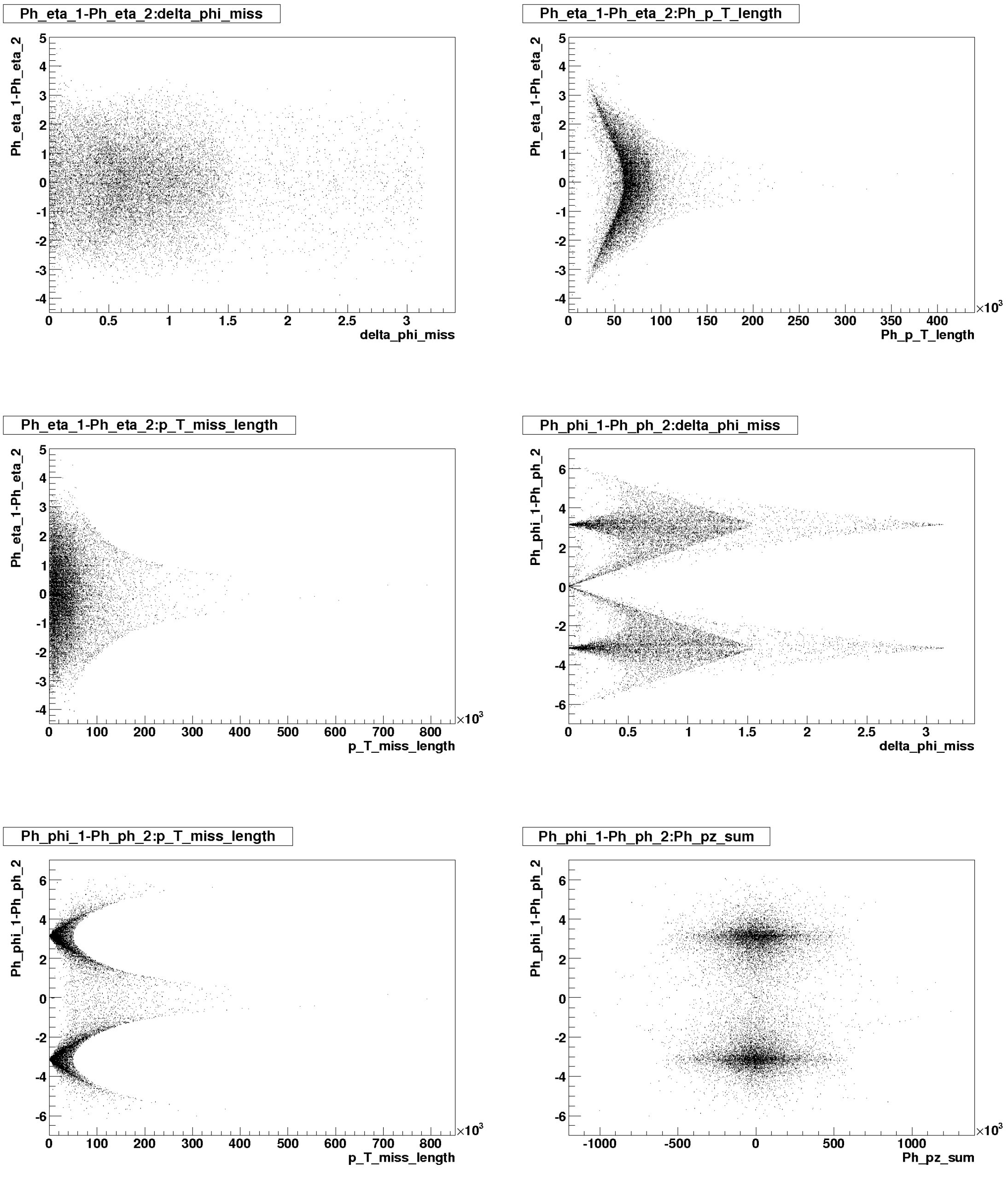

Figure 6.9: Trying out different parameters plotted against each other in the search for a parameter plane in which the signal and background are separated. The $p_T$-axis as well as the $p_z$-axis are in units of MeV. These plots were made using datasets not described in this thesis, generated by the Higgs working group.

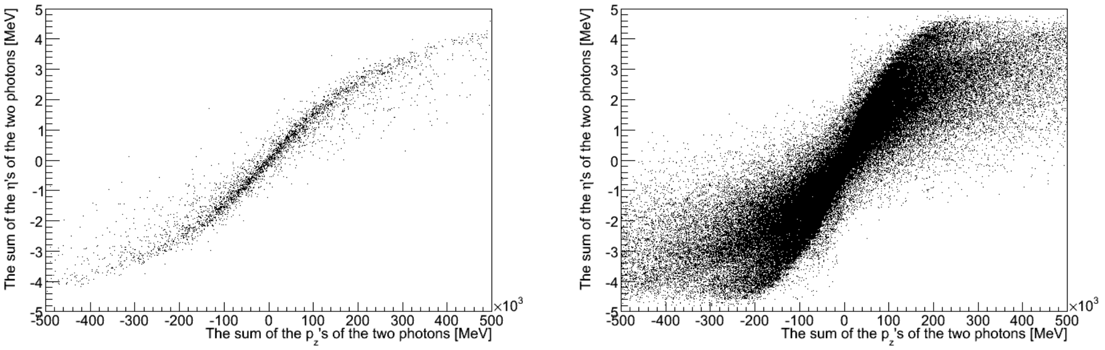

Figure 6.10: The sum of the $\eta$'s versus the sum of the $p_z$'s for the two photons. To the left: for a signal of a 120 GeV Higgs boson. To the right: the merged background. Made using 14 TeV full simulated data (unscaled).

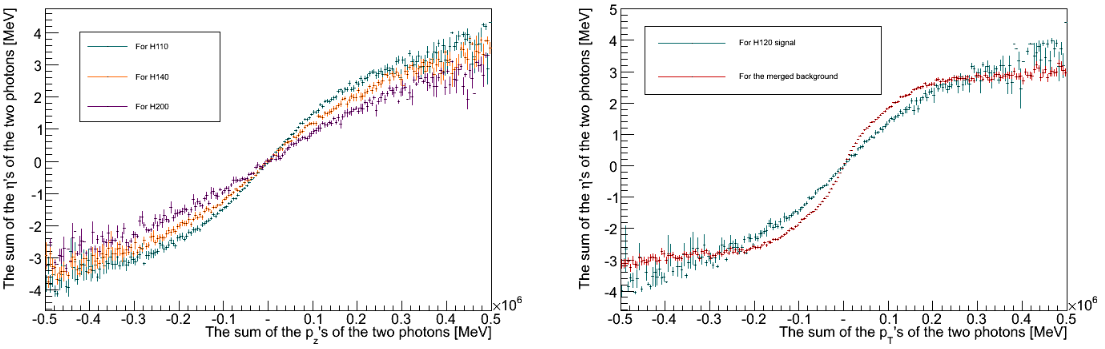

Figure 6.11: Profile plot of the sum of the $\eta$'s versus the sum of the $p_z$'s for the two photons. To the left: for the signals of a 110 GeV, a 140 GeV and a 200 GeV Higgs boson. To the right: for a 120 GeV signal and the merged background. Made using 14 TeV full simulated data (unscaled).

to separate the signal from the background.

| Dataset | # of events | | | | | | | |
|---|---|---|---|---|---|---|---|---|
| | with no cut (in dataset) | with more than one photon | plus $p_{T\gamma_1} > 40$ GeV | plus $p_{T\gamma_2} > 25$ GeV | plus $\|\eta\|_{\gamma_1} < 2.37$ | plus $\|\eta\|_{\gamma_2} < 2.37$ | plus $\|\eta\|_{\gamma_1} < 1.37$ or $\|\eta\|_{\gamma_1} > 1.52$ | plus $\|\eta\|_{\gamma_2} < 1.37$ or $\|\eta\|_{\gamma_2} > 1.52$ |
| *H120* | 4000 | 1622 | 1569 | 1528 | 1526 | 1520 | 1508 | 1492 |
| *gamgam* | 99939 | 23063 | 4026 | 3645 | 3639 | 3629 | 3604 | 3564 |
| *J0* | 389754 | 30 | 0 | 0 | 0 | 0 | 0 | 0 |
| *J1* | 388437 | 75 | 0 | 0 | 0 | 0 | 0 | 0 |
| *J2* | 380015 | 55 | 0 | 0 | 0 | 0 | 0 | 0 |
| *J3* | 326912 | 52 | 1 | 0 | 0 | 0 | 0 | 0 |
| *J4* | 388477 | 69 | 38 | 16 | 15 | 15 | 14 | 14 |
| *PhotonJet1* | 12440 | 35 | 3 | 2 | 2 | 2 | 2 | 2 |
| *PhotonJet2* | 12428 | 71 | 52 | 11 | 11 | 11 | 11 | 11 |
| *PhotonJet3* | 12429 | 64 | 64 | 28 | 27 | 25 | 25 | 23 |
| *PhotonJet4* | 108009 | 586 | 586 | 344 | 343 | 327 | 324 | 307 |

Table 6.3: Number of events for the 10 TeV datasets using full simulation, adding on one more cut for each column towards the right, unscaled.

| Dataset | # of events | | | | | | | |
|---|---|---|---|---|---|---|---|---|
| | with no cut | with more than one photon | plus $p_{T\gamma_1} > 40$ GeV | plus $p_{T\gamma_2} > 25$ GeV | plus $\|\eta\|_{\gamma_1}<2.37$ | plus $\|\eta\|_{\gamma_2}<2.37$ | plus $\|\eta\|_{\gamma_1}<1.37$ or $\|\eta\|_{\gamma_1}>1.52$ | plus $\|\eta\|_{\gamma_2}<1.37$ or $\|\eta\|_{\gamma_2}>1.52$ |
| *H120* | 1058 | 429 | 415 | 404 | 404 | 402 | 399 | 395 |
| *gamgam* | $2.8033\cdot10^{7}$ | $6.4693\cdot10^{6}$ | $1.1293\cdot10^{6}$ | $1.0224\cdot10^{6}$ | $1.0207\cdot10^{6}$ | $1.0179\cdot10^{6}$ | $1.0109\cdot10^{6}$ | $9.9972\cdot10^{5}$ |
| *J0* | $3.5094\cdot10^{14}$ | $2.7012\cdot10^{10}$ | 0 | 0 | 0 | 0 | 0 | 0 |
| *J1* | $2.5908\cdot10^{13}$ | $5.0023\cdot10^{9}$ | 0 | 0 | 0 | 0 | 0 | 0 |
| *J2* | $1.6803\cdot10^{12}$ | $2.4320\cdot10^{8}$ | 0 | 0 | 0 | 0 | 0 | 0 |
| *J3* | $9.8601\cdot10^{10}$ | $1.5683\cdot10^{7}$ | $3.0161\cdot10^{5}$ | 0 | 0 | 0 | 0 | 0 |
| *J4* | $4.5483\cdot10^{9}$ | $8.0785\cdot10^{5}$ | $4.4490\cdot10^{5}$ | $1.8732\cdot10^{5}$ | $1.7562\cdot10^{5}$ | $1.7562\cdot10^{5}$ | $1.6391\cdot10^{5}$ | $1.6391\cdot10^{5}$ |
| *PhotonJet1* | $5.9716\cdot10^{9}$ | $1.6801\cdot10^{7}$ | $1.4401\cdot10^{6}$ | $9.6007\cdot10^{5}$ | $9.6007\cdot10^{5}$ | $9.6007\cdot10^{5}$ | $9.6007\cdot10^{5}$ | $9.6007\cdot10^{5}$ |
| *PhotonJet2* | $5.7533\cdot10^{8}$ | $3.2868\cdot10^{6}$ | $2.4072\cdot10^{6}$ | $5.0922\cdot10^{5}$ | $5.0922\cdot10^{5}$ | $5.0922\cdot10^{5}$ | $5.0922\cdot10^{5}$ | $5.0922\cdot10^{5}$ |
| *PhotonJet3* | $4.9585\cdot10^{7}$ | $2.5532\cdot10^{5}$ | $2.5532\cdot10^{5}$ | $1.1170\cdot10^{5}$ | $1.0771\cdot10^{5}$ | $9.9737\cdot10^{4}$ | $9.9737\cdot10^{4}$ | $9.1758\cdot10^{4}$ |
| *PhotonJet4* | $3.4332\cdot10^{6}$ | $1.8627\cdot10^{4}$ | $1.8627\cdot10^{4}$ | $1.0934\cdot10^{4}$ | $1.0903\cdot10^{4}$ | $1.0394\cdot10^{4}$ | $1.0299\cdot10^{4}$ | 9758 |

Table 6.4: The scaled number of events for the 10 TeV datasets using full simulation, adding on one more cut for each column towards the right. Scaled using the numbers in Table 6.1.

| Dataset | # of events |  |  |  |  |  |  |  |
|---|---|---|---|---|---|---|---|---|
|  | with no cut (in dataset) | with more than one photon | plus $p_{T\gamma_1} > 40$ GeV | plus $p_{T\gamma_2} > 25$ GeV | plus $\|\eta\|_{\gamma_1}<2.37$ | plus $\|\eta\|_{\gamma_2}<2.37$ | plus $\|\eta\|_{\gamma_1}<1.37$ or $\|\eta\|_{\gamma_1}>1.52$ | plus $\|\eta\|_{\gamma_2}<1.37$ or $\|\eta\|_{\gamma_2}>1.52$ |
| *H110* | 20700 | 9017 | 8631 | 8304 | 8280 | 8249 | 8216 | 8161 |
| *H120* | 9250 | 3808 | 3691 | 3579 | 3570 | 3552 | 3525 | 3493 |
| *H130* | 11250 | 4933 | 4839 | 4739 | 4732 | 4708 | 4676 | 4635 |
| *H140* | 13250 | 5869 | 5788 | 5691 | 5680 | 5648 | 5605 | 5565 |
| *H200* | 4500 | 2135 | 2124 | 2118 | 2113 | 2107 | 2102 | 2084 |
| *gamgam* | 288750 | 94074 | 30660 | 28267 | 28195 | 28108 | 27972 | 27794 |
| *AAj* | 49450 | 19218 | 18256 | 16516 | 16443 | 16388 | 16289 | 16142 |
| *J0* | 176500 | 39 | 0 | 0 | 0 | 0 | 0 | 0 |
| *J1* | 191000 | 91 | 0 | 0 | 0 | 0 | 0 | 0 |
| *J2* | 83250 | 52 | 0 | 0 | 0 | 0 | 0 | 0 |
| *J3* | 85876 | 48 | 4 | 0 | 0 | 0 | 0 | 0 |
| *J4* | 303400 | 148 | 63 | 22 | 21 | 21 | 21 | 20 |
| *PhotonJet1* | 323200 | 1621 | 64 | 4 | 4 | 4 | 4 | 4 |
| *PhotonJet2* | 1620000 | 9111 | 6081 | 1075 | 1069 | 1062 | 1050 | 1022 |
| *PhotonJet3* | 293050 | 1794 | 1784 | 633 | 630 | 619 | 613 | 588 |
| *PhotonJet4* | 271400 | 1987 | 1983 | 1117 | 1112 | 1089 | 1084 | 1032 |
| *WplAA_lnu* | 26700 | 10491 | 9950 | 8058 | 8009 | 7965 | 7910 | 7825 |
| *WminAA_lnu* | 37750 | 15236 | 14327 | 11622 | 11584 | 11492 | 11432 | 11342 |
| *ZAA_ll* | 15000 | 5828 | 5338 | 4313 | 4279 | 4236 | 4196 | 4146 |
| *ZAA_nunu* | 15000 | 5694 | 5191 | 3961 | 3951 | 3939 | 3921 | 3898 |

Table 6.5: Number of events for the 14 TeV datasets using full simulation, adding on one more cut for each column towards the right, unscaled.

| Dataset | # of events | | | | | | | |
|---|---|---|---|---|---|---|---|---|
| | with no cut (in dataset) | with more than one photon | plus $p_{T\gamma_1} > 40$ GeV | plus $p_{T\gamma_2} > 25$ GeV | plus $\lvert\eta\rvert_{\gamma_1} < 2.37$ | plus $\lvert\eta\rvert_{\gamma_2} < 2.37$ | plus $\lvert\eta\rvert_{\gamma_1} < 1.37$ or $\lvert\eta\rvert_{\gamma_1} > 1.52$ | plus $\lvert\eta\rvert_{\gamma_2} < 1.37$ or $\lvert\eta\rvert_{\gamma_2} > 1.52$ |
| *H110* | 1959 | 853 | 817 | 786 | 784 | 781 | 778 | 772 |
| *H120* | 1929 | 794 | 770 | 746 | 744 | 741 | 735 | 728 |
| *H130* | 1692 | 742 | 728 | 713 | 712 | 708 | 703 | 697 |
| *H140* | 1254 | 555 | 548 | 539 | 538 | 535 | 530 | 527 |
| *H200* | 19 | 9 | 9 | 9 | 9 | 9 | 9 | 9 |
| *gamgam* | $4.9800\cdot10^{6}$ | $1.6225\cdot10^{6}$ | $5.2879\cdot10^{5}$ | $4.8751\cdot10^{5}$ | $4.8627\cdot10^{5}$ | $4.8477\cdot10^{5}$ | $4.8243\cdot10^{5}$ | $4.7936\cdot10^{5}$ |
| *AAj* | $2.1060\cdot10^{5}$ | $8.1847\cdot10^{4}$ | $7.7750\cdot10^{4}$ | $7.0339\cdot10^{4}$ | $7.0028\cdot10^{4}$ | $6.9794\cdot10^{4}$ | $6.9372\cdot10^{4}$ | $6.8746\cdot10^{4}$ |
| *J0* | $5.2309\cdot10^{14}$ | $1.1558\cdot10^{11}$ | 0 | 0 | 0 | 0 | 0 | 0 |
| *J1* | $4.1603\cdot10^{13}$ | $1.9821\cdot10^{10}$ | 0 | 0 | 0 | 0 | 0 | 0 |
| *J2* | $2.9127\cdot10^{12}$ | $1.8194\cdot10^{9}$ | 0 | 0 | 0 | 0 | 0 | 0 |
| *J3* | $1.8365\cdot10^{11}$ | $1.0265\cdot10^{8}$ | $8.5542\cdot10^{6}$ | 0 | 0 | 0 | 0 | 0 |
| *J4* | $9.4941\cdot10^{9}$ | $4.6313\cdot10^{6}$ | $1.9714\cdot10^{6}$ | $6.8843\cdot10^{5}$ | $6.5714\cdot10^{5}$ | $6.5714\cdot10^{5}$ | $6.5714\cdot10^{5}$ | $6.2585\cdot10^{5}$ |
| *PhotonJet1* | $7.8535\cdot10^{9}$ | $3.9389\cdot10^{7}$ | $1.5551\cdot10^{6}$ | $9.7196\cdot10^{4}$ | $9.7196\cdot10^{4}$ | $9.7196\cdot10^{4}$ | $9.7196\cdot10^{4}$ | $9.7196\cdot10^{4}$ |
| *PhotonJet2* | $8.1712\cdot10^{8}$ | $4.5956\cdot10^{6}$ | $3.0672\cdot10^{6}$ | $5.4223\cdot10^{5}$ | $5.3920\cdot10^{5}$ | $5.3567\cdot10^{5}$ | $5.2962\cdot10^{5}$ | $5.1549\cdot10^{5}$ |
| *PhotonJet3* | $7.6934\cdot10^{7}$ | $4.7098\cdot10^{5}$ | $4.6835\cdot10^{5}$ | $1.6618\cdot10^{5}$ | $1.6539\cdot10^{5}$ | $1.6251\cdot10^{5}$ | $1.6093\cdot10^{5}$ | $1.5437\cdot10^{5}$ |
| *PhotonJet4* | $5.9316\cdot10^{6}$ | $4.3427\cdot10^{4}$ | $4.3339\cdot10^{4}$ | $2.4413\cdot10^{4}$ | $2.4303\cdot10^{4}$ | $2.3801\cdot10^{4}$ | $2.3691\cdot10^{4}$ | $2.2555\cdot10^{4}$ |
| *WplAA_lnu* | 100 | 39 | 37 | 30 | 30 | 30 | 30 | 29 |
| *WminAA_lnu* | 93 | 37 | 35 | 29 | 28 | 28 | 28 | 28 |
| *ZAA_ll* | 73 | 28 | 26 | 21 | 21 | 21 | 21 | 20 |
| *ZAA_nunu* | 146 | 55 | 51 | 39 | 38 | 38 | 38 | 38 |

Table 6.6: Number of events for the 14 TeV datasets using full simulation, adding on one more cut for each column towards the right, scaled using the numbers in Table 6.2.

### 6.2.2 The ’$p_{\mathrm{tmiss}}$ versus $\Delta\phi$’- plane

We will now have a look at the parameter plane that was used for this analysis. According to the simulations, the Higgs boson is mostly produced with relatively low transverse momenta (in the x-y plane), see Figure 6.12. This is due to the fact that the most common production mechanism for the Higgs boson is gluon-gluon fusion (see Figure 2.5), and the gluons, coming from the colliding protons travelling along the beam (that is, in the z-direction), rarely have a large transverse momentum. Knowing this, we can define a back-to-back decay of the Higgs to two photons in the transverse plane as the "perfect" case, and get some other variables out of this definition.

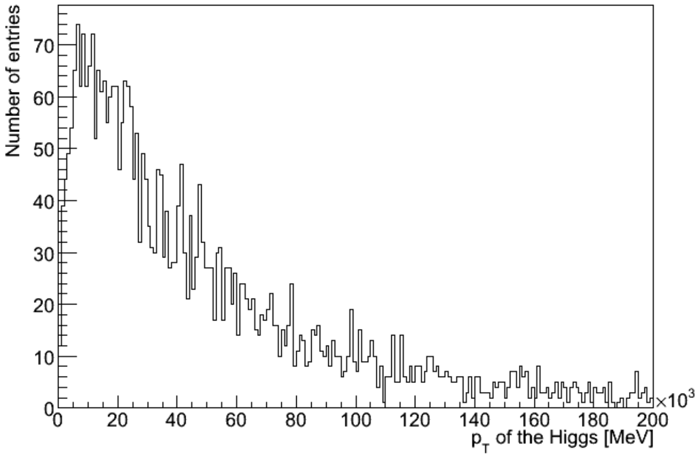

Figure 6.12: The transverse momenta of the Higgs boson from truth information, made with 14 TeV fully simulated data for a 120 GeV Higgs boson.

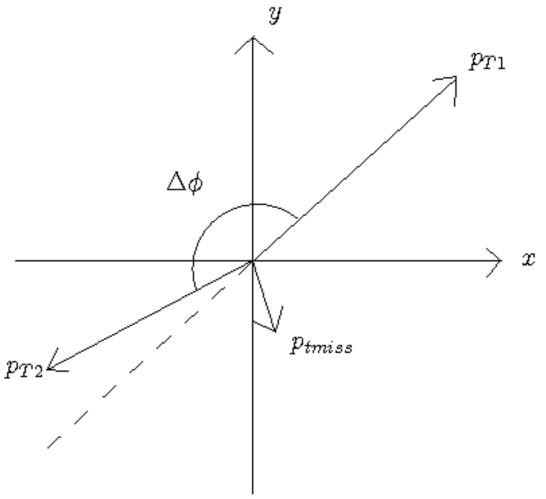

Figure 6.13: An illustration of the variables $p_{\mathrm{tmiss}}$ and $\Delta\phi$.

The variables we got out of this, which finally resulted in a parameter plane which looked promising, were $p_{\mathrm{tmiss}}$ and $\Delta\phi$. An illustration of these two variables can be found in Figure 6.13. $\Delta\phi$ is the

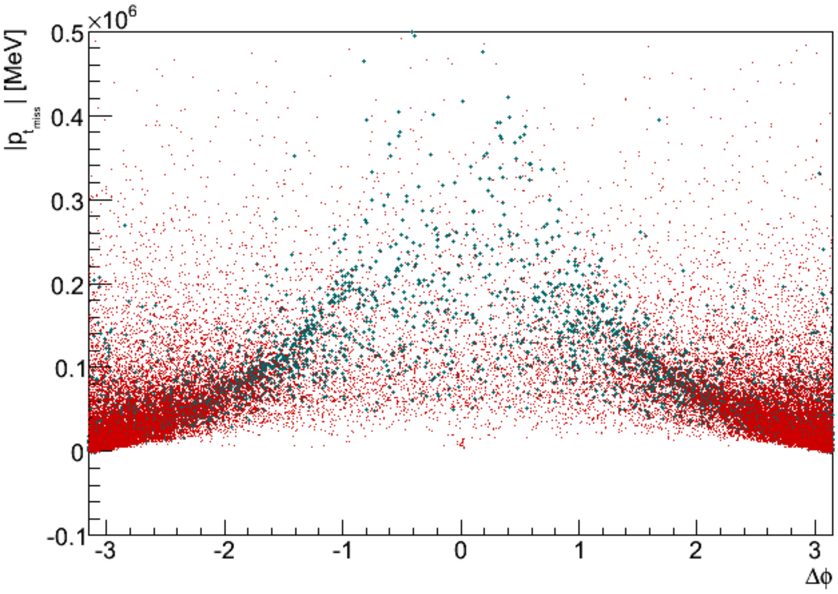

Figure 6.14: Scatter plot of $\mathrm{p}_{\mathrm{tmiss}}$ versus $\Delta\phi$ for the signal and background using 14 TeV fully simulated data, quitting the loop after 20.000 events (unscaled). The signal 120 GeV Higgs boson is marked in green. The merged background is indicated in red. Please note that the marker size of the signal is larger than for the background in order to make it more visible.

angle between the $\mathrm{p}_{\mathrm{T}}$'s of the two photons, given in the range $(-\pi, \pi)$. The angles $\pm\pi$ (or $\pm 180^\circ$ written in degrees) corresponds to a back-to-back configuration of the two photons. The variable $\mathrm{p}_{\mathrm{tmiss}}$ is what makes up for that the $\mathrm{p}_{\mathrm{T}}$'s of the two photons are not 'perfect' - that is back-to-back and of equal length. Written as an equation, this will be

$$\vec{\mathrm{p}}_{\mathrm{T1}} + \vec{\mathrm{p}}_{\mathrm{T2}} + \vec{\mathrm{p}}_{\mathrm{tmiss}} = 0.$$

In other words: You will have a non-zero $\mathrm{p}_{\mathrm{tmiss}}$ if the photons are either non-back-to-back and/or of non-equal energy.

What was ended up with, when plotting these parameters against each other, were the plots seen in Figures 6.14 and 6.15. In these plots, the distribution of a 120 GeV Higgs boson is plotted together with the backgrounds merged together. Making a profile plot of these parameters - that is, taking the average value of the content of every bin along the x-axis, making a one sigma error bar, we got what can be seen in Figure 6.16. From this last plot, it can be seen that the average value of $\mathrm{p}_{\mathrm{tmiss}}$ for the signal is higher than the average value of $\mathrm{p}_{\mathrm{tmiss}}$ for the background. This indicates a difference between the signal and the background, which we can try to exploit for finding a signal-free region.

### 6.2.3 The Regions of the '$\mathrm{p}_{\mathrm{tmiss}}$ versus $\Delta\phi$'-plane

In this parameter plane, it was possible to make some sort of separation of regions that contained both background and signal, a region that contained mostly background and a region where the signal was dominant. See Figure 6.17 for an illustration of the chosen regions in the '$\mathrm{p}_{\mathrm{tmiss}}$ versus

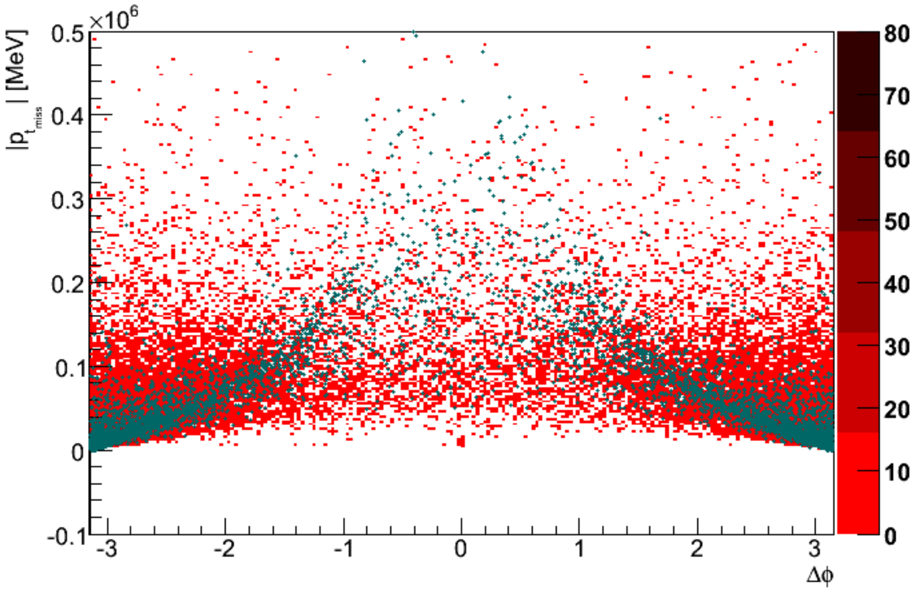

Figure 6.15: Plot of $p_{t_{miss}}$ versus $\Delta\phi$ for the signal and background, identical to Figure 6.14, where the density of background is shown in red, and the signal, laid on top of the background, is marked in green.

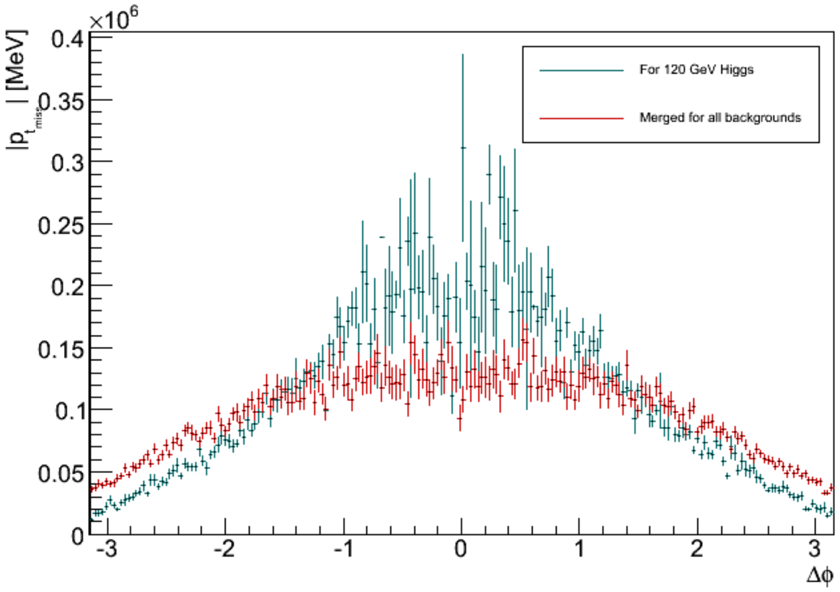

Figure 6.16: Profile plot of $p_{t_{miss}}$ versus $\Delta\phi$ for the signal and background, with the same inputs as Figure 6.14.

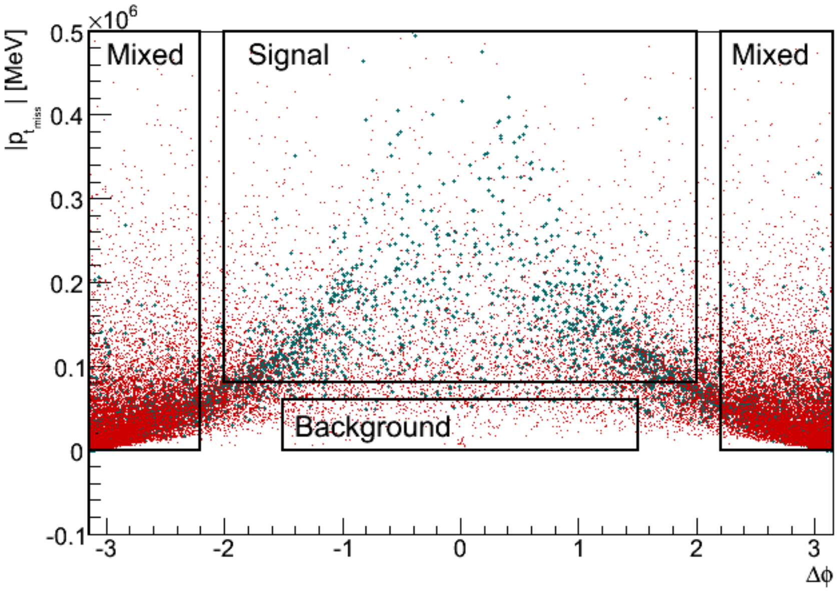

Figure 6.17: The chosen regions of $p_{tmiss}$ versus $\Delta\phi$ with labels (given by the main component of the region), identical to Figure 6.14.

$\Delta\phi$'-plane. This separation of regions had different purities for different types of background as can be seen in the Tables 6.7, 6.8, 6.9 and 6.10. In these tables the number of events for different signal and background datasets in the chosen regions of the '$p_{tmiss}$ versus $\Delta\phi$'-plane can be seen. Table 6.7 and 6.8 are for 10 TeV fully simulated data, the first table being unscaled, the second one being scaled using Table 6.1. Table 6.9 and 6.10 are for 14 TeV fully simulated data, the first one is unscaled, the second one is scaled using Table 6.2.

For the 14 TeV datasets *PhotonJet3*, *PhotonJet4*, *AAj*, *WminAA_lnu*, *WplAA_lnu*, *ZAA_ll* and *ZAA_nunu* the number of events within the signal region is larger than the number of events within the background region This is however okay, if the number of background events in the background region is large enough to study, and if it is representative for the background (i.e that no major distortion is made through the choice of region). This is because our main priority is to find a signal-free region, in which we can study the background alone. For the dataset *gamgam* the number of events in the background and signal dominant regions are so to speak identical.

However, for the datasets *J0*, *J1*, *J2*, *J3*, *J4*, *PhotonJet1* and *PhotonJet2*, we get a pleasant bonus - the number of events within the signal region is significantly lower than the number of events within the background region. In other words, in addition to that we can use this parameter plane to study the di-jet and the less energetic $\gamma$-jet background without being disturbed or biased by the signal by choosing the region of background domination, we might be able to reduce the amount of these backgrounds by doing a cut on this region. The scatter plot of $p_{tmiss}$ versus $\Delta\phi$ for the merged di-jet background can be seen in Figure 6.18 and for *PhotonJet1* merged with *PhotonJet2* in Figure 6.19. Please see Appendix A for the scatter plots of the '$p_{tmiss}$ versus $\Delta\phi$'-plane for the rest of the background datasets. In this appendix, the *PhotonJet* datasets have been merged, as have also *PhotonJet1*, *PhotonJet2* and *PhotonJet3* (leaving *PhotonJet4* out), from where it can be seen that removing the more energetic $\gamma$-jet backgrounds reduces the events in the signal region.

| Dataset \ Region | Mixed | Background | Signal |
|---|---|---|---|
| *H120* | 1300 | 4 | 214 |
| *gamgam* | 22614 | 18 | 3 |
| *J0* | 0 | 30 | 0 |
| *J1* | 17 | 57 | 0 |
| *J2* | 17 | 36 | 0 |
| *J3* | 20 | 26 | 0 |
| *J4* | 38 | 14 | 6 |
| *PhotonJet1* | 29 | 6 | 0 |
| *PhotonJet2* | 52 | 14 | 2 |
| *PhotonJet3* | 42 | 0 | 18 |
| *PhotonJet4* | 412 | 0 | 153 |

Table 6.7: The number of events in the different regions of the $p_{tmiss}$ versus $\Delta\phi$ plane (as given in Figure 6.17) for different datasets requiring only two photons using 10 TeV fully simulated data, unscaled (see Table 6.8 for the scaled numbers).

As already mentioned; the two less energetic datasets of this type are the best ones for separating the $\gamma$-jet background from the signal.

All the signal datasets (*H110*, *H120*, *H130*, *H140*, *H200*) have a significantly larger fraction of events within the signal region than within the background region, which is of course what we want. For the 10 TeV datasets, similar results are obtained (with the datasets available), with the exception that the *gamgam* displays a better ratio of events within the signal/background region.

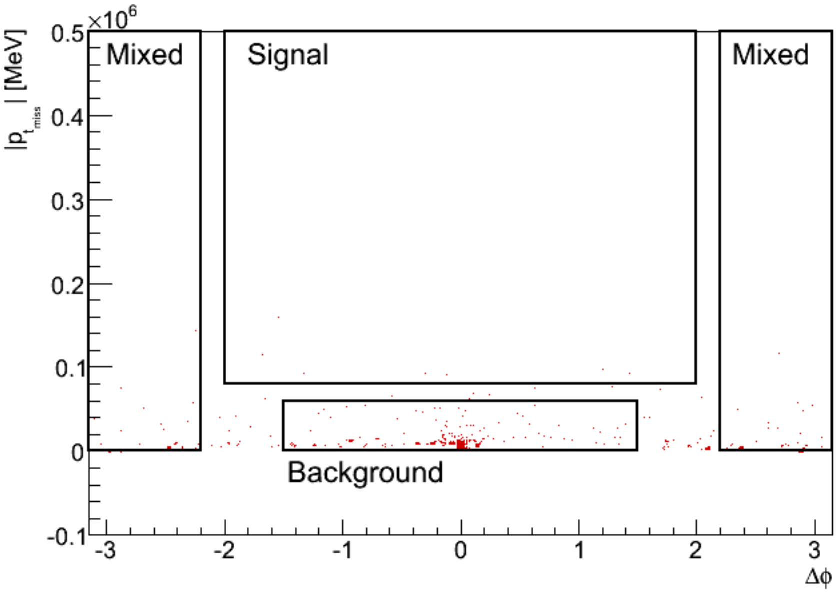

Figure 6.18: Scatter plot of $p_{t\mathrm{miss}}$ versus $\Delta\phi$ for the merged datasets for dijet background (*J0-J4*) using 14 TeV full simulation data.

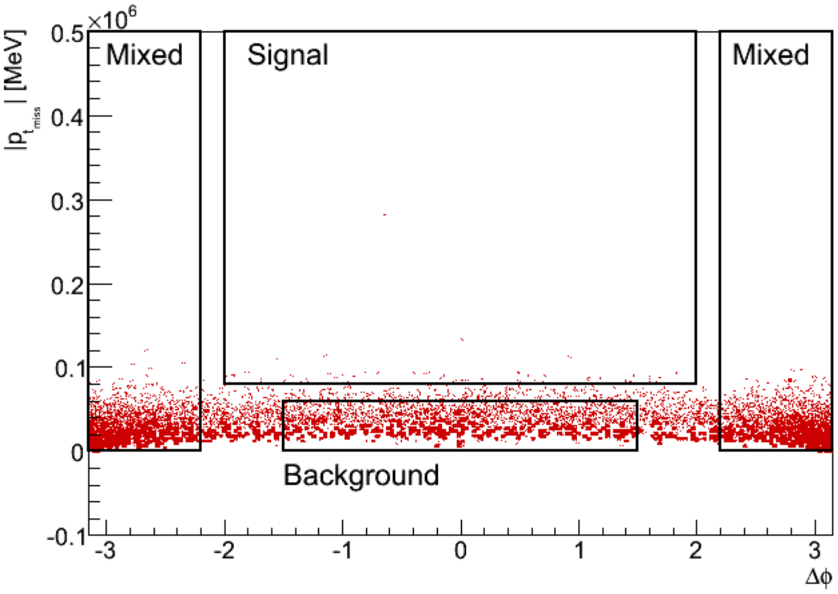

Figure 6.19: Scatter plot of $p_{t\mathrm{miss}}$ versus $\Delta\phi$ for the merged datasets *PhotonJet1* and *PhotonJet2* using 14 TeV full simulation data.

| Region<br>Dataset | Mixed | Background | Signal |
|---|---|---|---|
| *H120* | 344 | 1 | 57 |
| *gamgam* | $1.0566\cdot10^{8}$ | 84.100 | 14.017 |
| *J0* | 0 | $1.7547\cdot10^{12}$ | 0 |
| *J1* | $7.3406\cdot10^{10}$ | $2.4613\cdot10^{11}$ | 0 |
| *J2* | $4.7611\cdot10^{9}$ | $1.0082\cdot10^{10}$ | 0 |
| *J3* | $3.2867\cdot10^{8}$ | $4.2727\cdot10^{8}$ | 0 |
| *J4* | $2.8806\cdot10^{7}$ | $1.0623\cdot10^{7}$ | $4.548\cdot10^{6}$ |
| *PhotonJet1* | $2.8863\cdot10^{7}$ | $5.9717\cdot10^{6}$ | 0 |
| *PhotonJet2* | $4.9862\cdot10^{6}$ | $1.3424\cdot10^{6}$ | $1.9178\cdot10^{5}$ |
| *PhotonJet3* | $3.4710\cdot10^{5}$ | 0 | $1.4876\cdot10^{5}$ |
| *PhotonJet4* | $2.3575\cdot10^{5}$ | 0 | $8.7547\cdot10^{4}$ |

Table 6.8: The number of events in the different regions of the $\mathrm{p}_{\mathrm{tmiss}}$ versus $\Delta\phi$ plane (as given in Figure 6.17) for different datasets requiring only two photons using 10 TeV fully simulated data. Scaled using Table 6.1.

| Region<br>Dataset | Mixed | Background | Signal |
|---|---|---|---|
| *H110* | 7260 | 19 | 1159 |
| *H120* | 3065 | 15 | 508 |
| *H130* | 4017 | 8 | 653 |
| *H140* | 4810 | 12 | 766 |
| *H200* | 1828 | 2 | 228 |
| *gamgam* | 92211 | 119 | 120 |
| *AAj* | 17057 | 77 | 904 |
| *J0* | 6 | 32 | 0 |
| *J1* | 19 | 67 | 0 |
| *J2* | 22 | 26 | 0 |
| *J3* | 16 | 27 | 0 |
| *J4* | 60 | 56 | 7 |
| *PhotonJet1* | 1198 | 292 | 0 |
| *PhotonJet2* | 6475 | 1468 | 59 |
| *PhotonJet3* | 1257 | 19 | 325 |
| *PhotonJet4* | 1462 | 4 | 481 |
| *WplAA_lnu* | 8234 | 165 | 1200 |
| *WminAA_lnu* | 11840 | 242 | 1729 |
| *ZAA_ll* | 3937 | 141 | 1039 |
| *ZAA_nunu* | 3748 | 152 | 1067 |

Table 6.9: The number of events in the different regions of the $\mathrm{p}_{\mathrm{tmiss}}$ versus $\Delta\phi$ plane (as given in Figure 6.17) for different datasets requiring two photons for 14 TeV fully simulated data. These numbers are unscaled, see Table 6.10 for the scaled numbers.

| Region<br>Dataset | Mixed | Background | Signal |
|---|---|---|---|
| *H110* | 687.1 | 1.798 | 109.7 |
| *H120* | 639.2 | 3.128 | 105.9 |
| *H130* | 604.2 | 1.203 | 98.21 |
| *H140* | 455.2 | 1.136 | 72.50 |
| *H200* | 7.531 | 0.0082 | 0.9394 |
| *gamgam* | $1.590{\cdot}10^{6}$ | 2052 | 2070 |
| *AAj* | $7.264{\cdot}10^{4}$ | 327.9 | 3850 |
| *J0* | $1.778{\cdot}10^{10}$ | $9.484{\cdot}10^{10}$ | 0.000 |
| *J1* | $4.139{\cdot}10^{9}$ | $1.459{\cdot}10^{10}$ | 0.000 |
| *J2* | $7.697{\cdot}10^{8}$ | $9.097{\cdot}10^{8}$ | 0.000 |
| *J3* | $3.422{\cdot}10^{7}$ | $5.774{\cdot}10^{7}$ | 0.000 |
| *J4* | $1.878{\cdot}10^{6}$ | $1.752{\cdot}10^{6}$ | $2.191{\cdot}10^{5}$ |
| *PhotonJet1* | $2.911{\cdot}10^{7}$ | $7.095{\cdot}10^{6}$ | 0.000 |
| *PhotonJet2* | $3.266{\cdot}10^{6}$ | $7.405{\cdot}10^{5}$ | $2.976{\cdot}10^{4}$ |
| *PhotonJet3* | $3.300{\cdot}10^{5}$ | 4988 | $8.532{\cdot}10^{4}$ |
| *PhotonJet4* | $3.195{\cdot}10^{4}$ | 87.42 | $1.051{\cdot}10^{4}$ |
| *WplAA_lnu* | 30.85 | 0.6181 | 4.4953 |
| *WminAA_lnu* | 29.09 | 0.5947 | 4.249 |
| *ZAA_ll* | 19.24 | 0.6889 | 5.0766 |
| *ZAA_nunu* | 36.47 | 1.4790 | 10.38 |

Table 6.10: The number of events in the different regions of the $p_{\mathrm{tmiss}}$ versus $\Delta\phi$ plane (as given in Figure 6.17) for different datasets requiring two photons for 14 TeV fully simulated data. Scaled using Table 6.2.

## 6.3 Fitting the Distributions

In this section, the results of fits of the signal alone, two of the backgrounds alone and finally the signal together with the irreducible (*gamgam*) background will be shown. All the fits were made using 14 TeV fully simulated data and 30 $\text{fb}^{-1}$ of data.

### 6.3.1 Fitting the Signal

A fit of the signals was made using a simple Gaussian. The results of the fitting can be seen in Figure 6.20, in which the histograms are normalized to the integral of the distribution. Note that the fits of the distributions for a given mass of the Higgs within the mixed region and the signal-enriched regions look similar. This is exactly what is wanted - in order to be able to exploit the regions of the ’$p_{tmiss}$ versus $\Delta\phi$’-plane, the invariant mass distribution should not be distorted by the choice of region. The statistics of the signal in the background enriched region is very poor, as is also desired. Also note that the fitted mass tends to be 400-500 MeV under the generated Higgs mass in the signal and mixed region. This is consistent with the CSC results (in the CSC note, a category dependent offset was added to the fit).

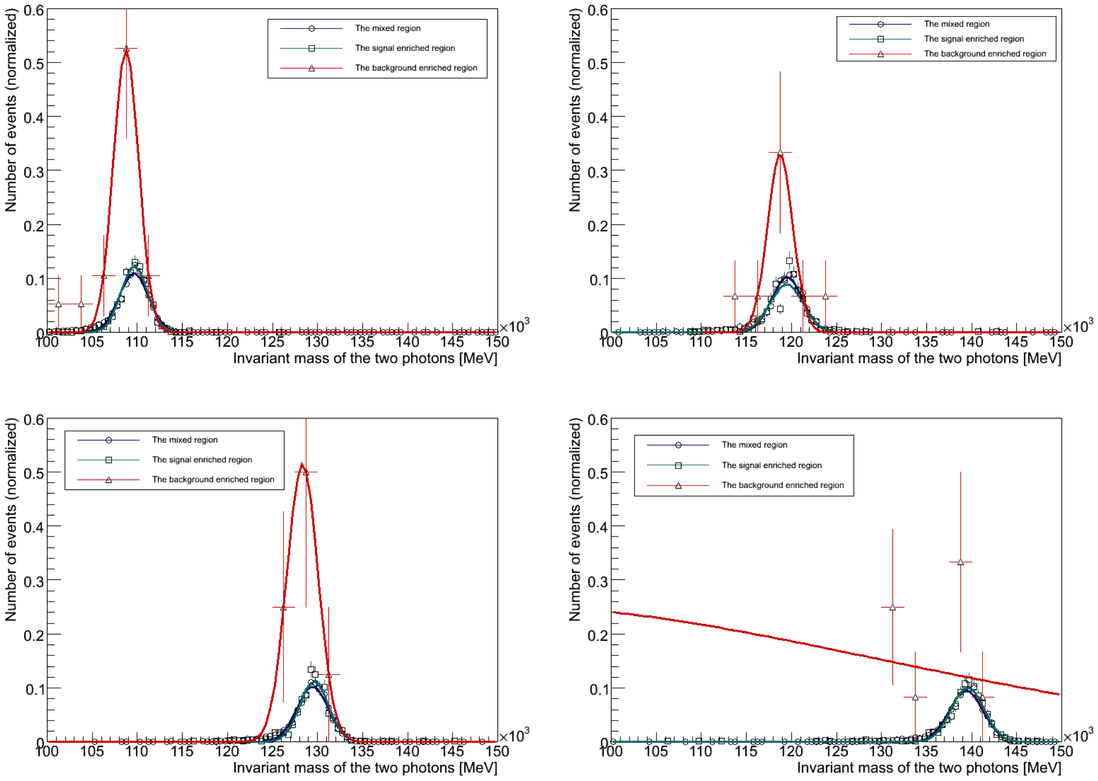

Figure 6.20: The signals of different masses fitted with a simple Gaussian. Topmost left: for a 110 GeV Higgs. Topmost right: for a 120 GeV Higgs. Bottom left: for a 130 GeV Higgs. Bottom right: for a 140 GeV Higgs. The histograms are normalized to the integral of the distribution. Note that the statistics in the background enriched region is very poor (which is what we want).

| Region | Parameter | Value [GeV] |
|---|---|---|
| Mixed | Mean | 109.6±0.02 |
| | $\sigma$ | 1.63±0.02 |
| Signal | Mean | 109.66±0.05 |
| | $\sigma$ | 1.48±0.04 |
| Background | Mean | 108.7±0.4 |
| | $\sigma$ | 1.4±0.3 |

Table 6.11: Parameters of the fit of the *H110* signal to a Gaussian as shown in Figure 6.20.

| Region | Parameter | Value [GeV] |
|---|---|---|
| Mixed | Mean | 119.51±0.04 |
| | $\sigma$ | 1.73±0.03 |
| Signal | Mean | 119.5±0.1 |
| | $\sigma$ | 1.84±0.08 |
| Background | Mean | 118.8±0.7 |
| | $\sigma$ | 1.4±0.4 |

Table 6.12: Parameters of the fit of the *H120* signal to a Gaussian as shown in Figure 6.20.

### 6.3.2 Fitting the Background

A fit of two of the backgrounds was also carried through. We picked two backgrounds that had fairly good statistics and a variation in simulated physics. They were fitted using a simple exponential function, see Figure 6.21 for the result (please note that the histograms are normalized to the integral of the distribution), and Table 6.15 and 6.16 for the values of the parameters of the fit. As can be seen, fitting the backgrounds with a simple exponential works fairly well in the mass range of 100 GeV to 200 GeV, but the backgrounds have different slopes in the different regions of the '$p_{\mathrm{tmiss}}$ versus $\Delta\phi$'-plane. That is to say - it is not possible to describe the backgrounds in the different regions of $p_{\mathrm{tmiss}}$ versus $\Delta\phi$ with a common exponential. On the bright side, there are no peaks created in the background distributions by choosing these regions.

| Region | Parameter | Value [GeV] |
|---|---|---|
| Mixed | Mean | 129.47±0.03 |
| | $\sigma$ | 1.74±0.03 |
| Signal | Mean | 129.61±0.07 |
| | $\sigma$ | 1.60±0.07 |
| Background | Mean | 128.3±0.7 |
| | $\sigma$ | 1.7±0.7 |

Table 6.13: Parameters of the fit of the *H130* signal to a Gaussian as shown in Figure 6.20.

| Region | Parameter | Value [GeV] |
|---|---|---|
| Mixed | Mean<br>$\sigma$ | 139.39±0.03<br>1.89±0.02 |
| Signal | Mean<br>$\sigma$ | 139.56±0.07<br>1.82±0.06 |
| Background | Mean<br>$\sigma$ | 84±26<br>45±68 |

Table 6.14: Parameters of the fit of the *H140* signal to a Gaussian as shown in Figure 6.20.

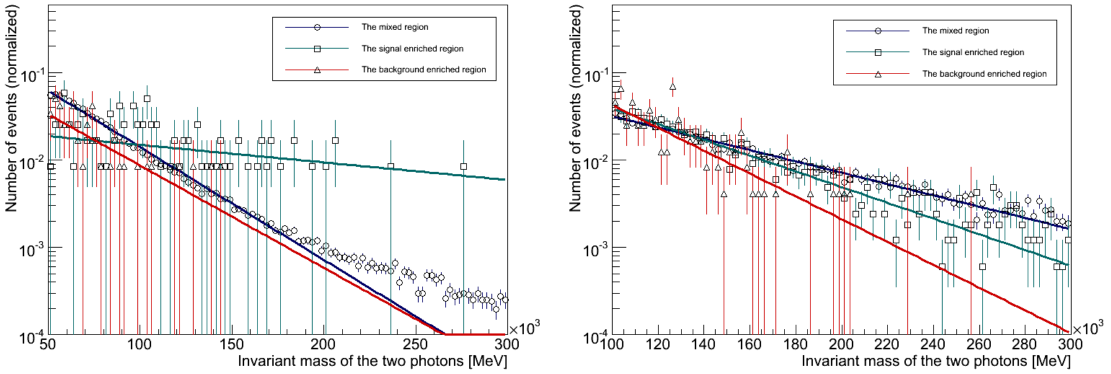

Figure 6.21: Two of the backgrounds (with fairly good statistics) fitted with a simple exponential. To the left: the *gamgam* background. To the right: the *WminAA_lnu* background. Please note that the histograms are normalized to the integral of the distribution.

### 6.3.3 Fitting the Signal with the Irreducible (*gamgam*) Background

A fit of a 120 GeV Higgs signal on top of the *gamgam* background was carried through, using three different combination of functions to describe the signal and background. The fits were all performed in the range 100 GeV $< m_{\gamma\gamma} <$ 200 GeV, with a bin width of 1 GeV. Throughout Equations 6.1-6.4, x is equal to $m_{\gamma\gamma}$ (the calculated invariant mass of the two photons).

For the background, two different functions were implemented. In the polynomial description of

| Region | Parameter | Value [MeV] |
|---|---|---|
| Mixed | Constant<br>Slope | -1.29±0.01<br>$(-2.97\pm0.01)\cdot10^{-5}$ |
| Signal | Constant<br>Slope | -3-7±0.3<br>$(-0.5\pm0.3)\cdot10^{-5}$ |
| Background | Constant<br>Slope | -2.1±0.9<br>$(-3\pm1)\cdot10^{-5}$ |

Table 6.15: Parameters of the fit of the *gamgam* background to a simple exponential as shown in Figure 6.21.

| Region | Parameter | Value [MeV] |
|---|---|---|
| Mixed | Constant | -1.96±0.04 |
| | Slope | (-1.49±0.02)·$10^{-5}$ |
| Signal | Constant | -1.7±0.1 |
| | Slope | (-2.07±0.07)·$10^{-5}$ |
| Background | Constant | -0.1±0.6 |
| | Slope | (-3.0±0.5)·$10^{-5}$ |

Table 6.16: Parameters of the fit of the *WminAA_lnu* background to a simple exponential as shown in Figure 6.21.

the background, the function

$$y = ax^3 + bx^2 + cx + d \tag{6.1}$$

was used, where $a, b, c$ and $d$ were parameters to be fitted.

In the exponential description of the background, the function

$$y = e^{f+gx} \tag{6.2}$$

was used, where $f$ and $g$ were parameters to be fitted.

Also for the signal two different functions were implemented. In the Gaussion description of the signal, the function

$$y = N \cdot binwidth \cdot \frac{1}{\sqrt{2\pi\sigma_x^2}} \cdot e^{-\frac{1}{2}\left(\frac{x-M_H}{\sigma_x}\right)^2} \tag{6.3}$$

was used, where $N, M_H$ and $\sigma_x$ were parameters to be fitted.

The second signal function to be used was the so-called Crystal Ball function, which the fit in the CSC note was based on, in order to compensate for the low-mass tails seen in Figure 6.20, which come from photon energy losses before the electromagnetic calorimeter. This function reads;

$$y = N \cdot binwidth \cdot \begin{cases} e^{-t^2/2} & \text{for } t > -\alpha, \\ \left(\frac{n}{|\alpha|}\right)^n \cdot e^{-|\alpha|^2/2} \cdot \left(\frac{n}{|\alpha|} - \alpha - t\right)^{-n} & \text{otherwise} \end{cases} \tag{6.4}$$

where $t = \frac{x-M_H}{\sigma_x}$. The parameters to be fitted were $N, M_H, \sigma_x, n$ and $\alpha$. For these two last distributions, $N$ gives the number of $H \to \gamma\gamma$ events, $M_H$ gives the mass of the Higgs (the mean of the distribution), $\sigma_x$ gives the width of the signal distribution and $\alpha$ indicates where the transition from a Gaussian distribution to a non-Gaussian tail is.

The three combinations studied were:

- a Gaussian description of the signal with a polynomial description of the background.

- a Gaussian description of the signal with a exponential description of the background.
- a description of the signal using the Crystal Ball function with a polynomial description of the background.

In order to get more realistic statistics for the background (keep in mind the large scale factors as shown in Table 6.2, causing unnaturally big fluctuations in the resulting histogram), a statistical smoothing of the distribution was performed (hereafter simply called ¨smoothed¨ background distributions). What was done, was to make a fit of the background alone, take the resulting function and fill a new histogram based on it by randomly picking out values. The routine randomly picks out a x-value and a y-value within domain of the function (within the boundaries of the original histogram), and if this point (x,y) lies under the function (gotten from the background fit), the point is accepted. Otherwise, it is rejected. Thus, a histogram that has more realistic statistics than the one from the *gamgam* dataset is obtained. The random distributions of the polynomial background used in combination with the Gaussian and the Crystal Ball description of the signal were the same, as the seed used for generating the random histogram was unchanged.

The resulting values of the parameters $N, M_H$ and $\sigma_x$ of the fit, as well as the $\chi^2$ and the number of degrees of freedom (d.o.f.) can be seen in Table 6.17. In this table, $\mathrm{N}_{H\rightarrow\gamma\gamma}$ (equal to $N$ in the Equations 6.3 and 6.4) should be the number seen for dataset *H120* in the last column of Table 6.6, that is 728. This number is reproduced by the fit within the errors. As also can be seen, the choice of function for the background description does not affect the number of signal events found (it does only have a small saying in the uncertainty of this number), which is good. A value of $\chi^2/$d.o.f deviating significantly from $\sim$1 indicates too low statistics and a poor fit, whereas a value significantly lower than $\sim$1 indicates a too good fit (the statistical fluctuations are too low to be reasonable). The number of degrees of freedom is calculated in the following manner:

$$\text{d.o.f.} = \text{number of bins - parameters in fit.}$$

The number of bins was 100 (100 GeV - 200 GeV / 1GeV), and the number of parameters for the different combinations was

- 3+4 = 7 for Gaussian+polynomial,
- 3+2 = 5 for Gaussian+exponential,
- 5+4 = 9 for Crystal Ball+polynomial,

resulting in number of d.o.f of 93, 95, 91 for the three combinations of signal and background descriptions respectively.

The graphical result of the first fit can be seen in Figure 6.22, in the full range of the fit as well as in a smaller area around the signal top. The blue histogram is the smoothed background distribution, the black markers are the merged signal and background and the green curve is the result of the fit. The graphical result of the second fit is not displayed, as it looked fairly similar to the first fit.

The third fit, using a Crystal Ball description of the signal, gives the graphical result as can be seen in Figure 6.23. Again, the blue histogram is the smoothed background distribution, the black markers are the merged signal and background and the green curve is the result of the fit. Even though the fit gives a good $\chi^2$, it does not describe the signal well. The signal peak is far too broad; the fit includes events that are not signal events in the peak. The mass reconstructed is in addition too low, and has a larger error than for the two previous fits. More work is needed to use the Crystal Ball function. Exercising the fit on the signal-only distributions shown in Figure 6.20 is probably a good place to start.

The significance of the Higgs boson signal for the best fit (Gaussian+polynomial) is $\sim \frac{644}{165} \approx 4$. A significance of 2.4 was obtained in the CSC note for an inclusive analysis with the Higgs boson mass fixed at 120 GeV for the full background with 10 fb$^{-1}$ of data. Since we have about a third of the total background, and 30 fb$^{-1}$ of data, this seems reasonably in agreement.

| Signal function | Background function | $N_{H\to\gamma\gamma}$ | $M_H$ [GeV] | $\sigma_H$ [GeV] | $\chi^2$/d.o.f. |
|---|---|---|---|---|---|
| Gauss | Polynomial | 644±165 | 119.8±0.4 | 1.3±0.3 | 70/93 |
| Gauss | Exponential | 644±177 | 119.8±0.4 | 1.4±0.4 | 88/95 |
| Crystal Ball | Polynomial | 1139±316 | 118±1 | 3.8±0.9 | 76/91 |

Table 6.17: Parameters of the three fits of a 120 GeV Higgs signal together with the irreducible (*gamgam*) background.

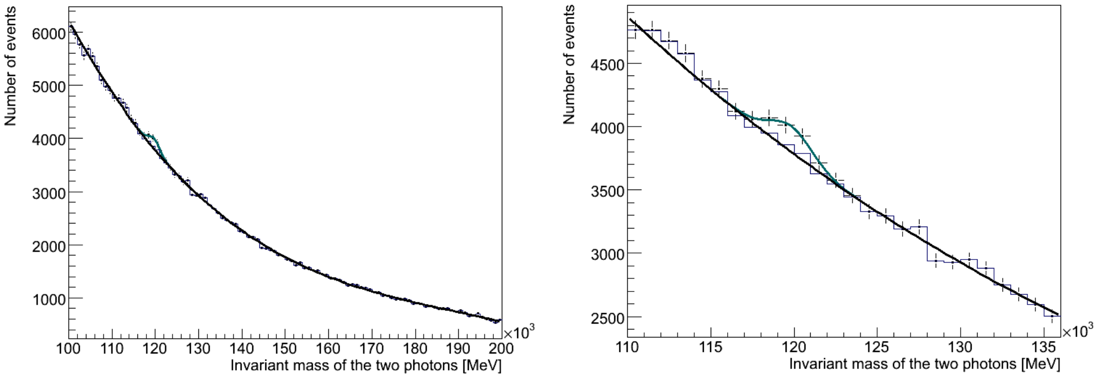

Figure 6.22: A fit of a 120 GeV Higgs signal and the *gamgam* background using a third degree polynomial description of the background and a Gaussian for the signal. The blue histogram is the smoothed background distribution, the black markers are the sum of the signal and background and the green curve is the result of the fit.

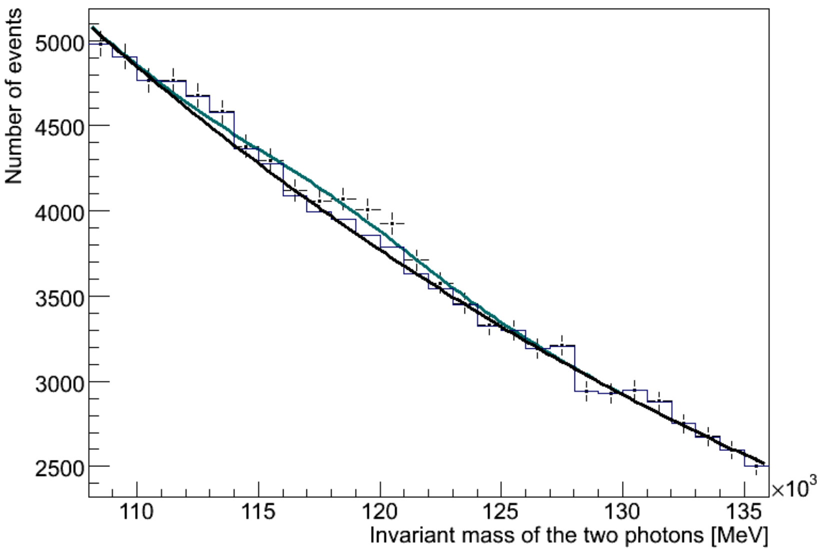

Figure 6.23: The result of the fit using the Crystal Ball function for the 120 GeV signal and a third degree polynomial for the *gamgam* background. The blue histogram is the smoothed background distribution, the black markers are the sum of the signal and background and the green curve is the result of the fit. It is clearly visible that the Crystal Ball function overestimated the width of the signal.

# Chapter 7

# Conclusions

A study of the $H \rightarrow \gamma\gamma$ channel has been carried through using Monte Carlo full simulation data, with emphasis on finding a new parameter plane in which the signal and the background are separated, in order to be able to study the background without being disturbed or biased by the signal. In this manner, one can make sure when the real data comes that the background and the detector response are fully understood before looking for the signal in the invariant mass distribution.

It was discovered that the statistics of the fully generated samples of the background was far too poor to do a fit of the joint signal and background invariant mass distribution. This leads to scale factors of horrible sizes, especially for the di-jet background, but also for the least energetic ($\sum p_T$<70 GeV) of the $\gamma$-jet background. This shows that, with the current tools, it is impossible to do a study of this decay channel using a full simulation of the background. In order to be able to do that, some sort of trick must be found in the simulation technique in order to filter out the uninteresting events (containing less than two photons) before the full generation of the event is carried through. If this is achieved, it may be possible to generate a large enough amount of events to avoid enormous scale factors. Thus, one is at this stage forced to use fast simulation of the background to get good enough statistics. Therefore a firm statement cannot be made about how it will look in the detector, what ratio of signal and background can be expected and how good the outlooks for discovering the Higgs boson through this decay channel are. As a reminder, the effects of pile-up and the spread and displacement of the vertex are not included in the full simulations used in this study. All these factors show even more clearly the need for a data-driven analysis, and encourages the development of a method in which we do not have to trust the MC simulations.

The regions of the '$p_{\mathrm{tmiss}}$ versus $\Delta\phi$'-plane as given in Figure 6.17 look promising to give signal-free background samples for some of the backgrounds after the $\gamma\gamma$-selection is done, in order to do a MC free study of the background in real data. The background samples that this selection of regions look most promising for are the di-jet background and the least energetic ($\sum p_T$<70 GeV) of the $\gamma$-jet background. This is very interesting because reducing these backgrounds relies heavily on fine details of the detector for $\pi^0$ and jet identification. Thus it is very fortunate that the datasets with the largest scaling factors (i.e with the highest uncertainty) have the best separation from the signal in this parameter plane. In addition, cutting out the background enriched region of the '$p_{\mathrm{tmiss}}$ versus $\Delta\phi$'-plane can possibly improve the signal significance, as most of the di-jet background resides with in this region, in addition to part of the $\gamma$-jet background. This has not yet been studied. Selecting these regions is shown to alter the slope of the background, but not to distort the signal. That the cuts do not distort the signal is somewhat difficult to state firmly for the background enriched region, since the statistics of the signal is low, but this is at the same time a good result, because we do not want much of the signal to lie within this region.

The structure in Figure 6.10 indicates that it might be possible to study the relative contributions of the different background processes. Finding out which backgrounds give the different slopes (given that it is not a random structure) requires more investigation.

A third degree polynomial function can better describe the irreducible (*gamgam*) background in the mass region 100 GeV - 200 GeV than an exponential function, but both seem to work well within the statistics at hand for this analysis. For the signal, a Gaussian function seems to better describe the peak than the naive application of the Crystal Ball function. However, it is clear that the Gaussian description of the signal is not good enough, since the low-mass tail is not well described. More work is needed here.

# Appendix A

# Scatter Plots of $\mathrm{p}_{\mathrm{tmiss}}$ versus $\Delta\phi$ for Backgrounds Using 14 TeV Fully Simulated Data

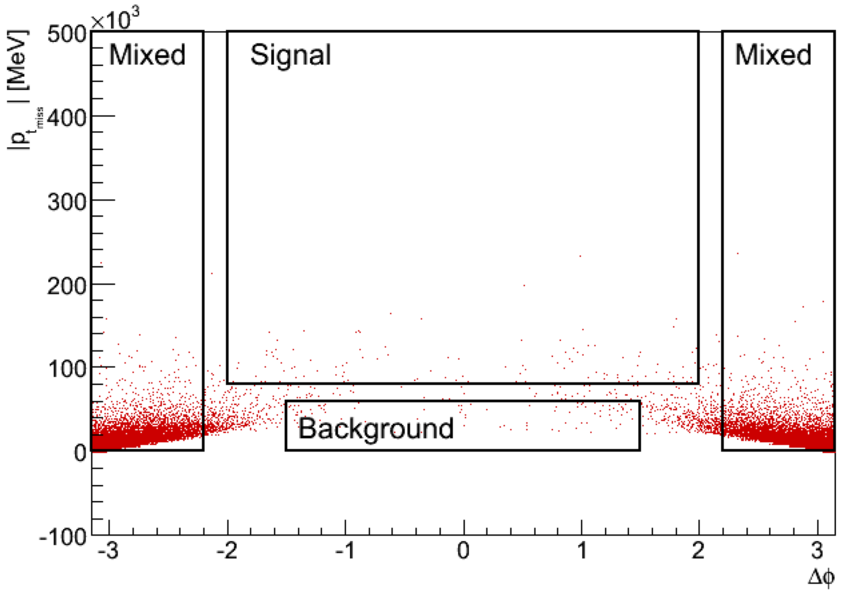

Figure A.1: Scatter plot of $\mathrm{p}_{\mathrm{tmiss}}$ versus $\Delta\phi$ for the dataset *gamgam* using 14 TeV full simulation data.

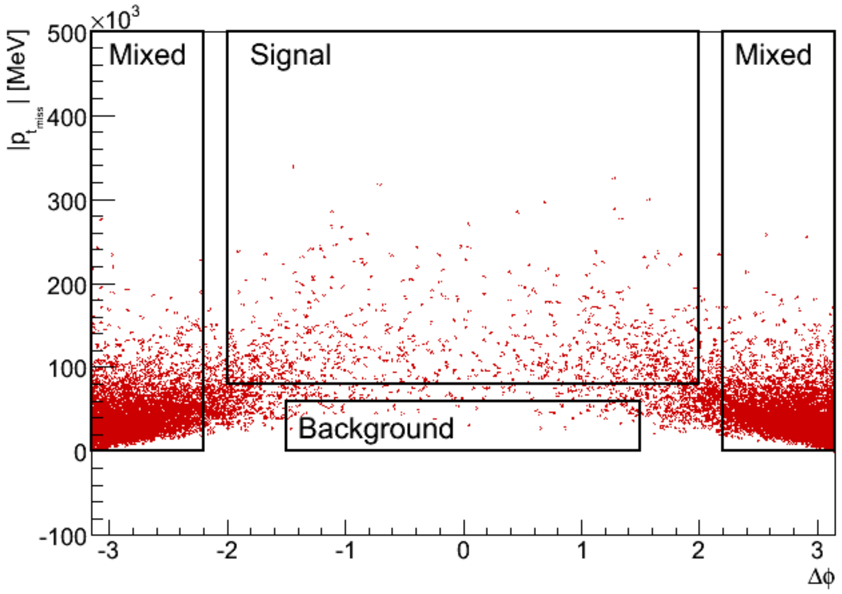

Figure A.2: Scatter plot of $\mathrm{p}_{\mathrm{tmiss}}$ versus $\Delta\phi$ for the dataset *AAj* using 14 TeV full simulation data.

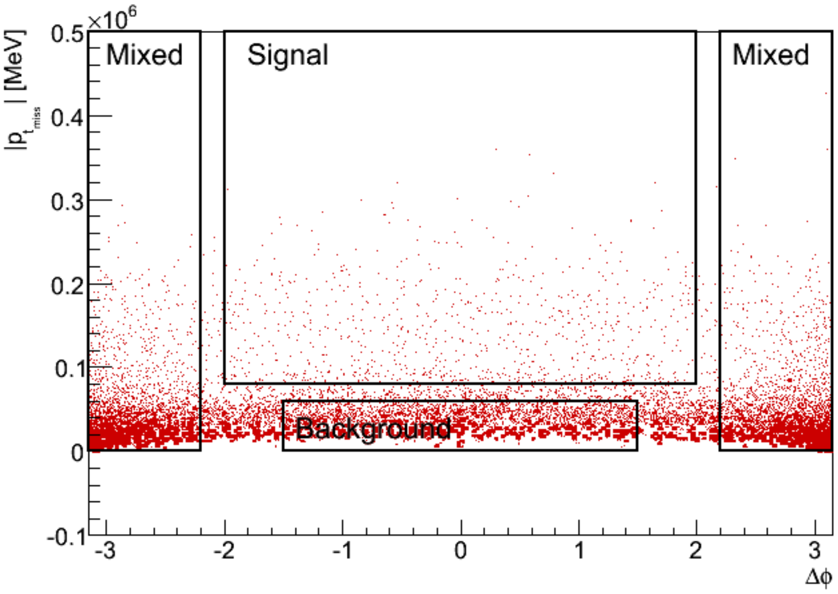

Figure A.3: Scatter plot of $p_{t\text{miss}}$ versus $\Delta\phi$ for the merged datasets for photon-jet background (*PhotonJet1*-*PhotonJet4*) using 14 TeV full simulation data.

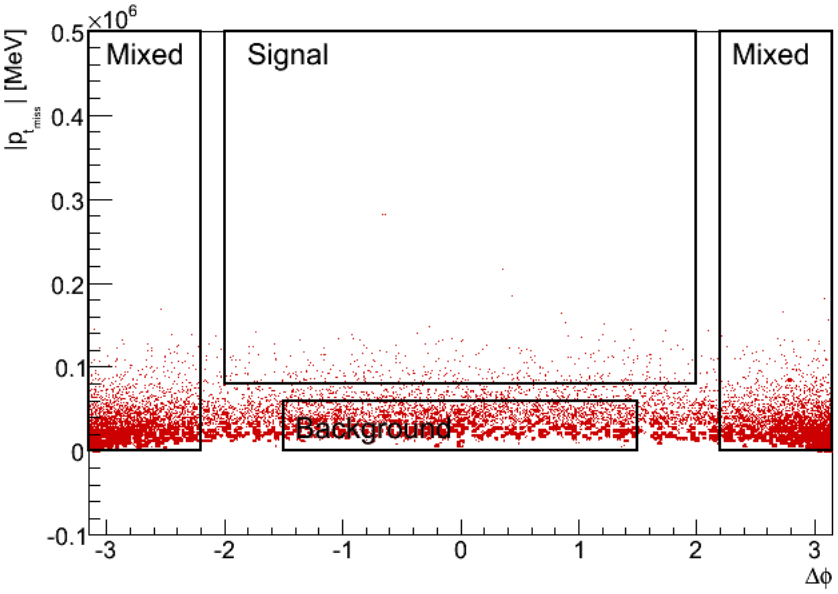

Figure A.4: Scatter plot of $p_{t\text{miss}}$ versus $\Delta\phi$ for the merged datasets *PhotonJet1*-*PhotonJet3* using 14 TeV full simulation data.

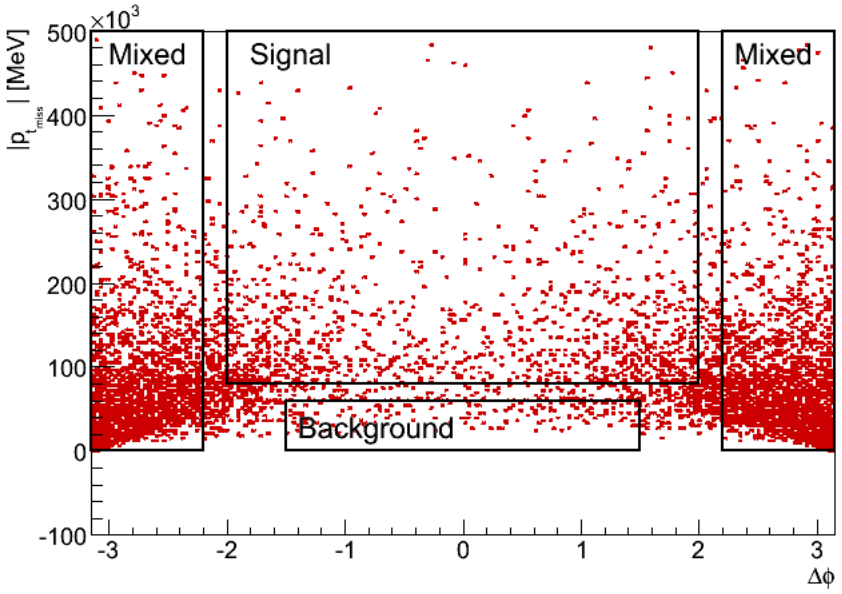

Figure A.5: Scatter plot of $p_{\mathrm{tmiss}}$ versus $\Delta\phi$ for the dataset *WplAA_lnu* using 14 TeV full simulation data.

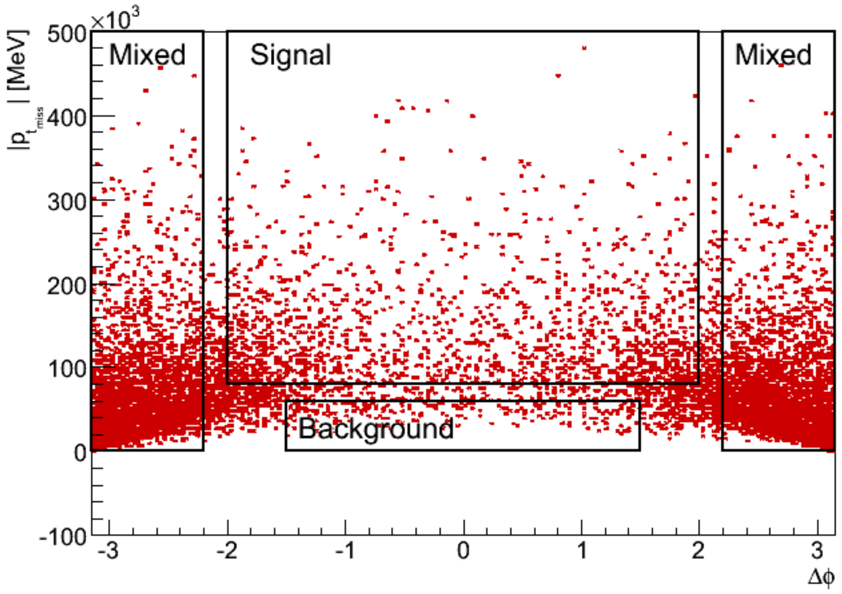

Figure A.6: Scatter plot of $p_{\mathrm{tmiss}}$ versus $\Delta\phi$ for the dataset *WminAA_lnu* using 14 TeV full simulation data.

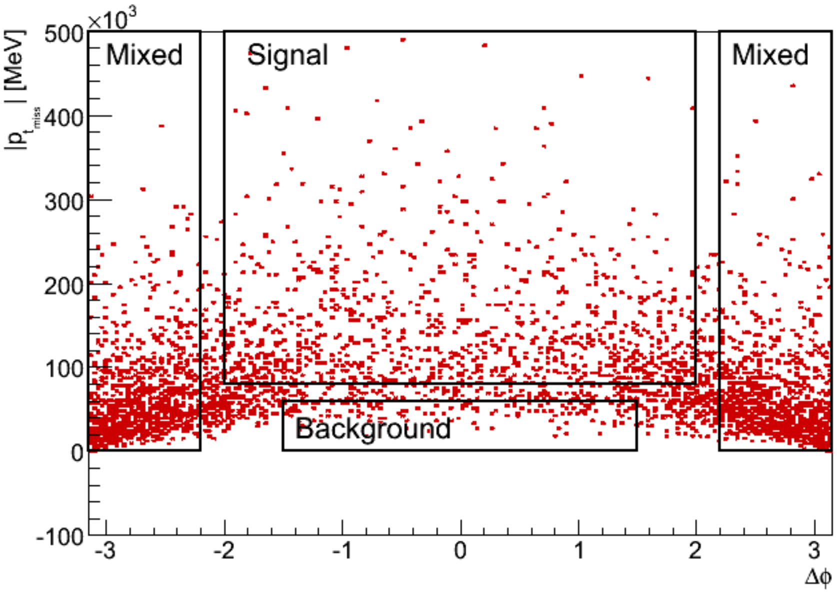

Figure A.7: Scatter plot of $p_{tmiss}$ versus $\Delta\phi$ for the dataset *ZAA_ll* using 14 TeV full simulation data.

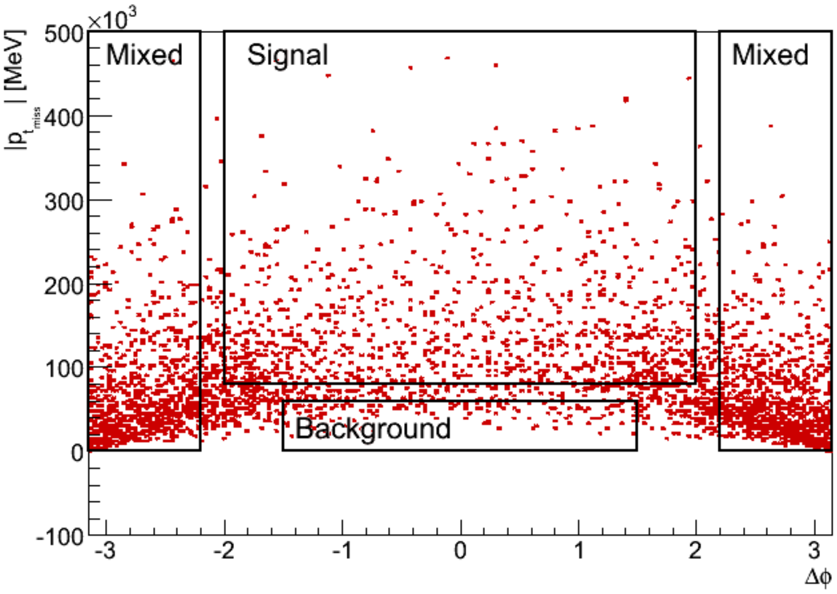

Figure A.8: Scatter plot of $p_{tmiss}$ versus $\Delta\phi$ for the dataset *ZAA_nunu* using 14 TeV full simulation data.

# Appendix B

# Plots of Invariant Mass Distributions for the Background Using 14 TeV Fully Simulated Data

The plots of the invariant mass in the three different regions of the ’$\mathrm{p_{tmiss}}$ versus $\Delta\phi$’-plane are normalized to the integral of the respective distributions. The rapid drop-off in the *AAj* background at approximately 150 GeV is not understood.

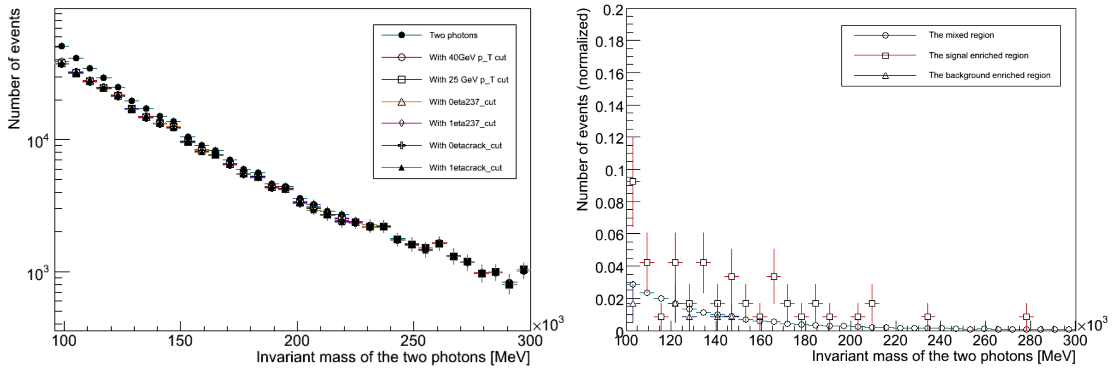

Figure B.1: Invariant mass for the dataset *gamgam* using 14 TeV full simulations. To the left: the effect on the invariant mass of applying the cuts, one at a time. To the right: the invariant mass in the three selected regions according to Figure 6.17.

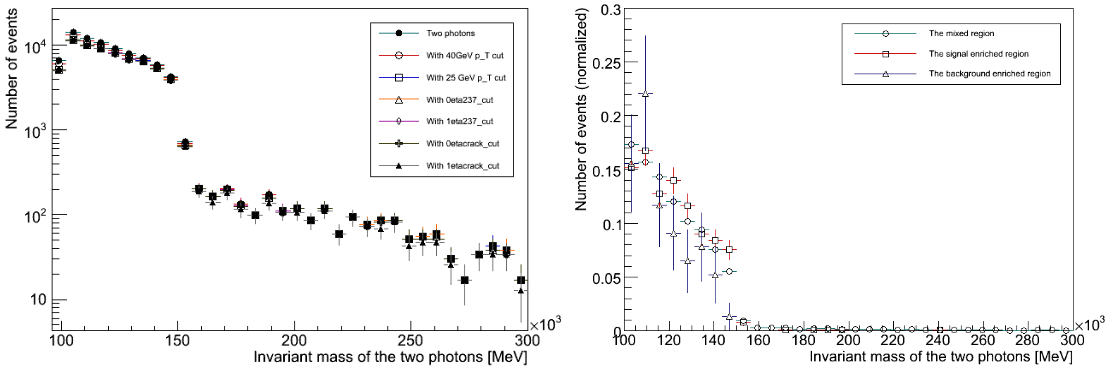

Figure B.2: Invariant mass for the dataset *AAj* using 14 TeV full simulations. To the left: the effect on the invariant mass of applying the cuts, one at a time. To the right: the invariant mass in the three selected regions according to Figure 6.17.

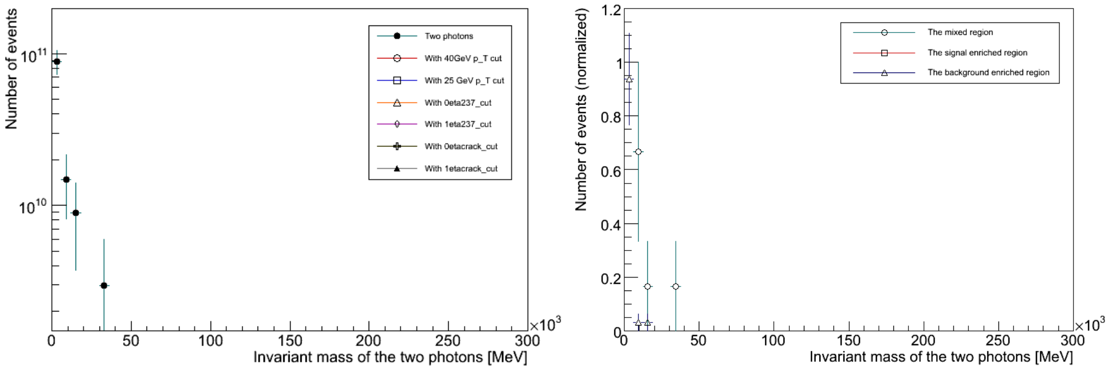

Figure B.3: Invariant mass for the dataset *J0* using 14 TeV full simulations. To the left: the effect on the invariant mass of applying the cuts, one at a time. To the right: the invariant mass in the three selected regions according to Figure 6.17.

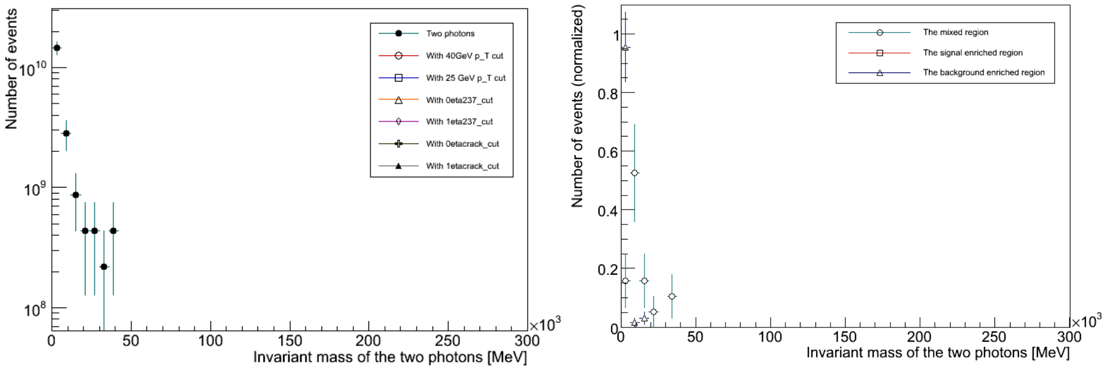

Figure B.4: Invariant mass for the dataset *J1* using 14 TeV full simulations. To the left: the effect on the invariant mass of applying the cuts, one at a time. To the right: the invariant mass in the three selected regions according to Figure 6.17.

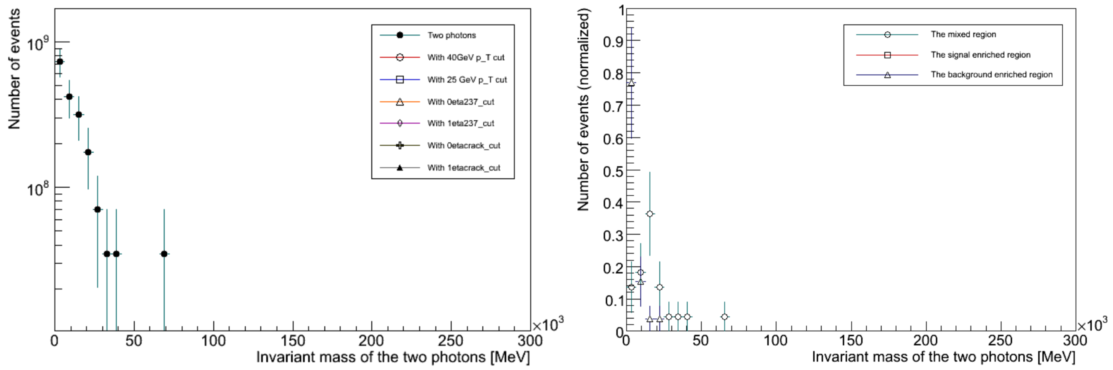

Figure B.5: Invariant mass for the dataset *J2* using 14 TeV full simulations. To the left: the effect on the invariant mass of applying the cuts, one at a time. To the right: the invariant mass in the three selected regions according to Figure 6.17.

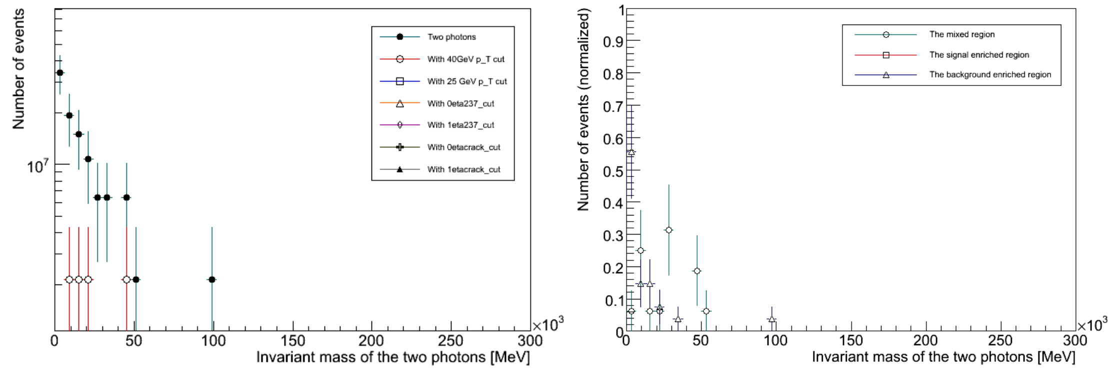

Figure B.6: Invariant mass for the dataset *J3* using 14 TeV full simulations. To the left: the effect on the invariant mass of applying the cuts, one at a time. To the right: the invariant mass in the three selected regions according to Figure 6.17.

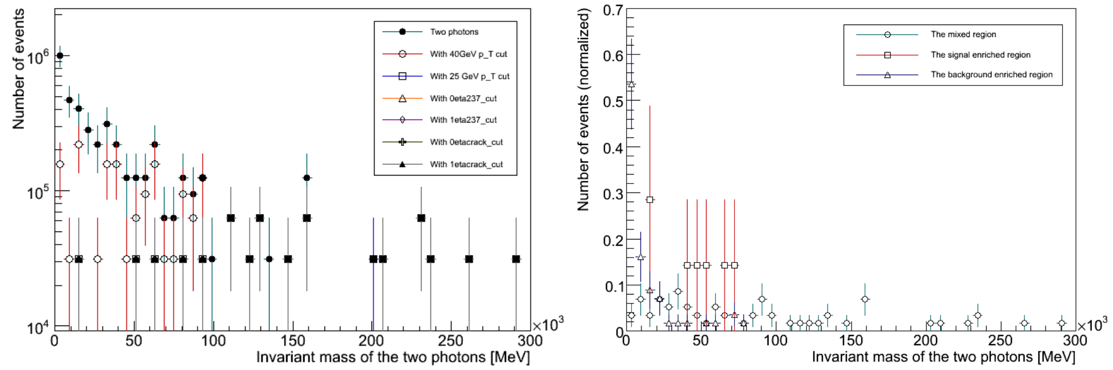

Figure B.7: Invariant mass for the dataset *J4* using 14 TeV full simulations. To the left: the effect on the invariant mass of applying the cuts, one at a time. To the right: the invariant mass in the three selected regions according to Figure 6.17.

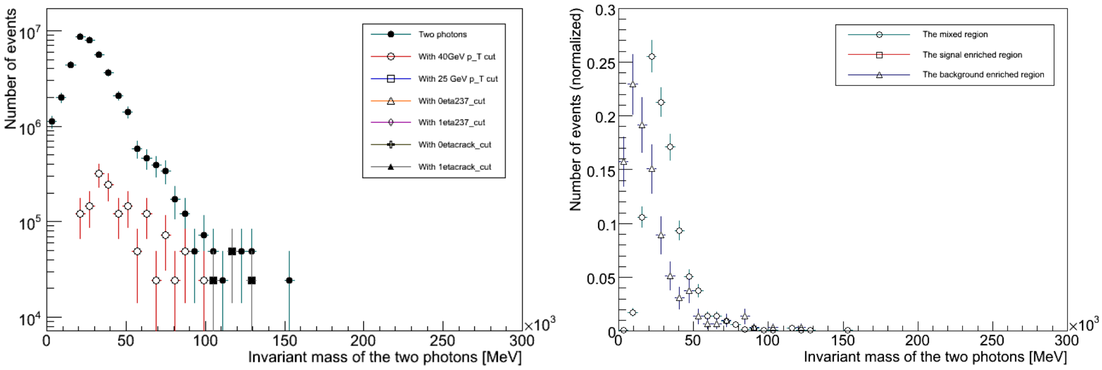

Figure B.8: Invariant mass for the dataset *PhotonJet1* using 14 TeV full simulations. To the left: the effect on the invariant mass of applying the cuts, one at a time. To the right: the invariant mass in the three selected regions according to Figure 6.17.

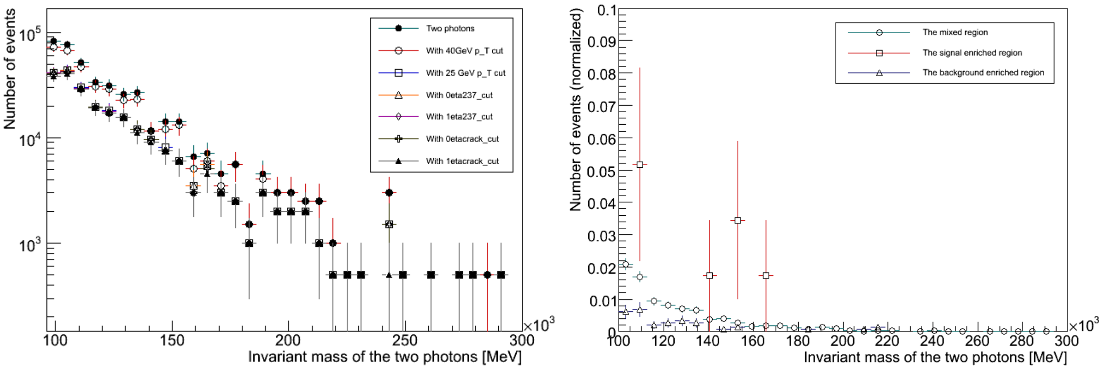

Figure B.9: Invariant mass for the dataset *PhotonJet2* using 14 TeV full simulations. To the left: the effect on the invariant mass of applying the cuts, one at a time. To the right: the invariant mass in the three selected regions according to Figure 6.17.

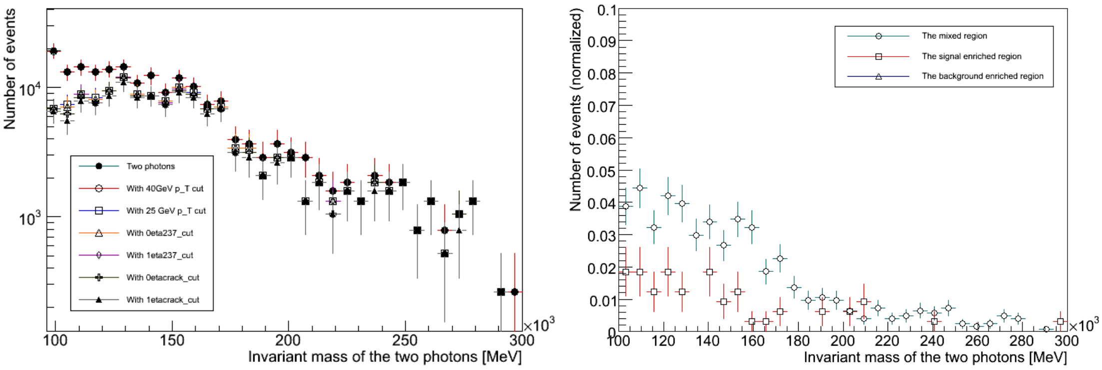

Figure B.10: Invariant mass for the dataset *PhotonJet3* using 14 TeV full simulations. To the left: the effect on the invariant mass of applying the cuts, one at a time. To the right: the invariant mass in the three selected regions according to Figure 6.17.

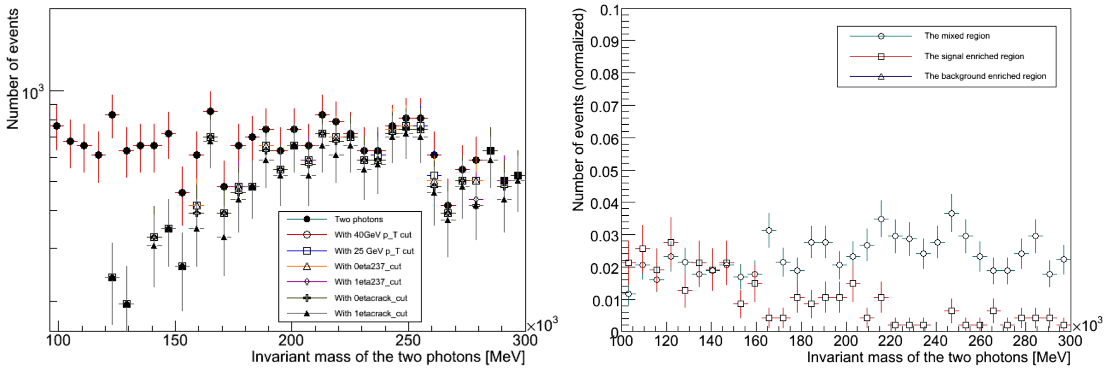

Figure B.11: Invariant mass for the dataset *PhotonJet4* using 14 TeV full simulations. To the left: the effect on the invariant mass of applying the cuts, one at a time. To the right: the invariant mass in the three selected regions according to Figure 6.17.

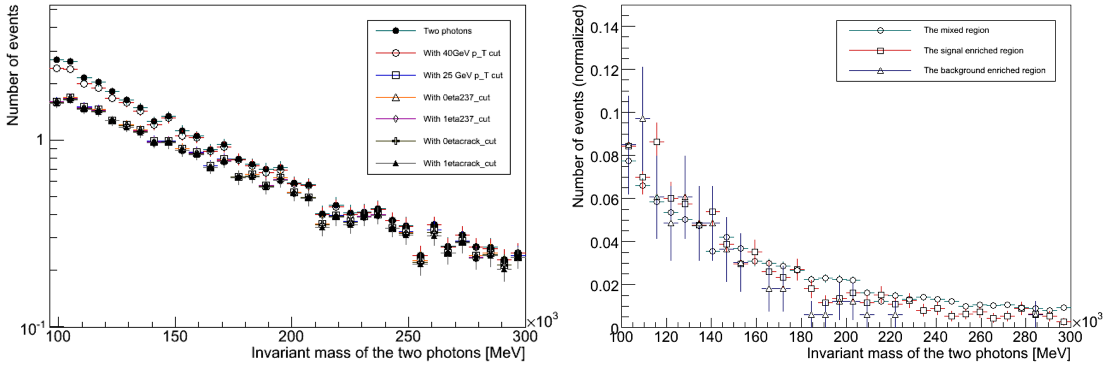

Figure B.12: Invariant mass for the dataset *WplAA_lnu* using 14 TeV full simulations. To the left: the effect on the invariant mass of applying the cuts, one at a time. To the right: the invariant mass in the three selected regions according to Figure 6.17.

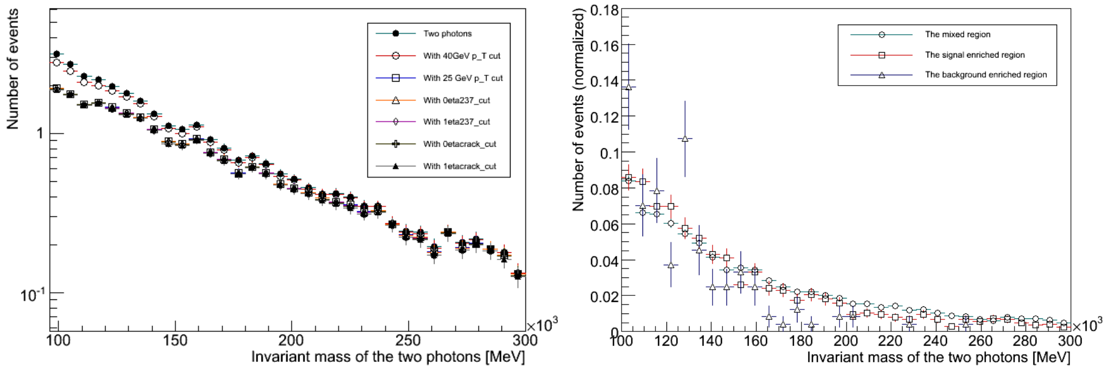

Figure B.13: Invariant mass for the dataset *WminAA_lnu* using 14 TeV full simulations. To the left: the effect on the invariant mass of applying the cuts, one at a time. To the right: the invariant mass in the three selected regions according to Figure 6.17.

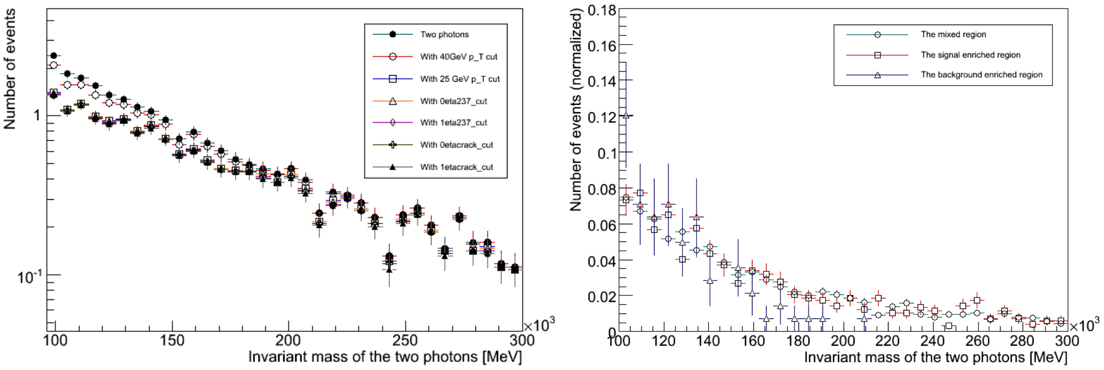

Figure B.14: Invariant mass for the dataset *ZAA_ll* using 14 TeV full simulations. To the left: the effect on the invariant mass of applying the cuts, one at a time. To the right: the invariant mass in the three selected regions according to Figure 6.17.

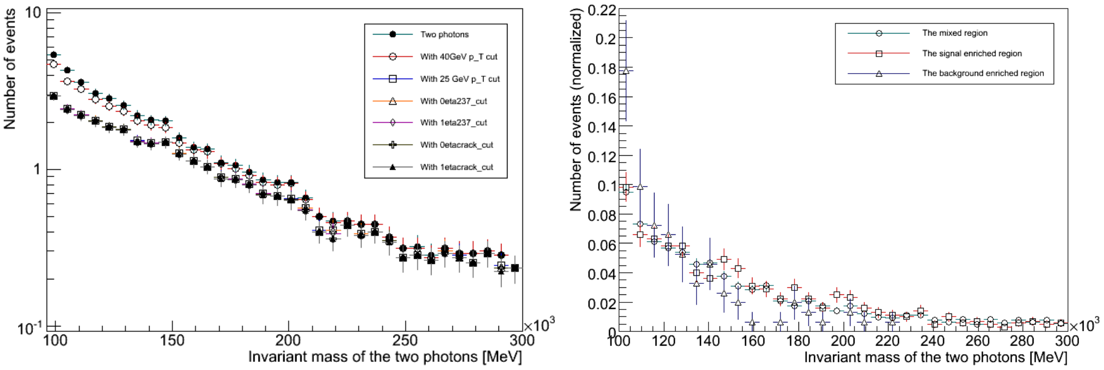

Figure B.15: Invariant mass for the dataset *ZAA_nunu* using 14 TeV full simulations. To the left: the effect on the invariant mass of applying the cuts, one at a time. To the right: the invariant mass in the three selected regions according to Figure 6.17.

# List of Figures

# List of Tables

# Bibliography

[1] ATLAS Collaboration. Expected Performance of the ATLAS Experiment, Detector, Trigger and Physics. Chapter: Prospects for the Discovery of the Standard Model Higgs Boson Using the $H \to \gamma\gamma$ Decay with the ATLAS Detector. *Geneva, to appear*, 2008.

[2] http://press.web.cern.ch/press/pressreleases/releases2008/pr10.08e.html.

[3] Accelerators and Beams Department. LHC Design Report Volume I - The LHC Main Ring. Technical report, CERN, 2004.

[4] P. Jenni. ATLAS welcome, LHC schedule, and goals of the week. ATLAS Overview Week, July 2008.

[5] F. J. Sciulli M. K. Gaillard, P. D. Grannis. The Standard Model of Particle Physics. *Rev.Mod.Phys. 71 (1999) S96-S111, arXiv:hep-ph/9812285v1*, 1998.

[6] F. Mandl and G. Shaw. *Quantum Field Theory, Revised Edition*. John Wiley & Sons, 1993.

[7] Ben M. Gripaios Guy D. Coughlan, James E. Dodd. *The Ideas of Particle Physics - An Introduction for Scientists*. Cambridge University Press, third edition, 2006.

[8] W. N. Cottingham and D. A. Greenwood. *An Introduction to the Standard Model of Particle Physics*. Cambrigde University Press, second edition, 2007.

[9] Cliff Burgess and Guy Moore. *The Standard Model A Primer*. Cambridge University Press, 2007.

[10] Donald H. Perkins. *Introduction to High Energy Physics*. Cambrigde University Press, $4^{th}$ edition, 2000.

[11] Heidi Sandaker. *ATLAS SemiConductor Tracker Development and Physics Simulation*. PhD thesis, University of Oslo, September 6 2008.

[12] C. Quigg. The electroweak theory. TASI lectures on Electroweak Theory hp/0204104, 2002.

[13] S. Pokorski. Gauge field theories. Cambridge University Press, (1987) 2000.

[14] Peter W. Higgs. Broken Symmetries and the Masses of Gauge Bosons. *Phys. Rev. Lett.*, 13(16):508–509, Oct 1964.

[15] F. Englert and R. Brout. Broken Symmetry and the Mass of Gauge Vector Mesons. *Phys. Rev. Lett.*, 13(9):321–323, Aug 1964.

[16] G. S. Guralnik, C. R. Hagen, and T. W. B. Kibble. Global Conservation Laws and Massless Particles. *Phys. Rev. Lett.*, 13(20):585–587, Nov 1964.

[17] John Ellis. Beyond the standard model with the LHC. *Nature*, 448:297–301, July 2007.

[18] Abdelhak Djouadi. The Anatomy of Electro-Weak Symmetry Breaking. II: The Higgs bosons in the Minimal Supersymmetric Model. *arXiv:hep-ph/0503173v2*, 2005.

[19] University of St Andrews Press Office. The end to a mystery? http://www.st-andrews.ac.uk/news/Title,18940,en.html, January 2008. Ref: Dark Matter 310108.

[20] Howard Baer and Xerxes Tata. *Weak Scale Supersymmetry - From Superfields to Scattering Events*. Cambridge University Press, 2006.

[21] Abdelhak Djouadi. The Anatomy of Electro-Weak Symmetry Breaking. I: The Higgs boson in the Standard Model. *arXiv:hep-ph/0503172v2*, 2005.

[22] Michael Kirby. Searches at the Tevatron for a High Mass Standard Model Higgs Boson. *arXiv:0810.3747v1*, October 2008.

[23] LEP Collaborations: ALEPH Collaboration, DELPHI Collaboration, L3 Collaboration, OPAL Collaboration, the LEP Electroweak Working Group. Precision Electroweak Measurements and Constraints on the Standard Model. *arXiv:0712.0929v2*, Dec 2007.

[24] André Sopczak. Complete LEP Data: Status of Higgs Boson Searches. *arXiv:hep-ph/0112082*, 2001.

[25] http://public.web.cern.ch/public/en/about/global-en.html.

[26] S.Eidelman et al. Particle physics booklet. Physics Letters B592, http://pdg.lbl.gov/, 2004.

[27] G. Aad et al. The ATLAS Collaboration. The ATLAS Experiment at the CERN Large Hadron Collider. Technical report, JINST 3 S08003, August 2008.

[28] http://public.web.cern.ch/public/en/lhc/atlas-en.html.

[29] ATLAS Collaboration. ATLAS detector and physics performance, Technical Design Report. Technical Report Volume I, CERN-LHCC-99-014, May 1999.

[30] ATLAS Collaboration. ATLAS Calorimeter Performance Technical Design Report. Technical report, CERN/LHCC 96-40, January 1997.

[31] http://atlas.web.cern.ch/atlas/groups/upgrades/.

[32] Eirik Gramstad. Search for the lightest MSSM Higgs boson in cascades of supersymmetric particles in ATLAS. Master's thesis, University of Oslo, June 2008.

[33] ATLAS Inner Detector Community. ATLAS Inner Detector Technical Design Report, Volume II. Technical report, CERN/LHCC/97-16,, April 1997.

[34] C. Amsler et al. (Particle Data Group). Review of Particle Physics. *Physics Letters B667*, page 54, 2008.

[35] ATLAS Collaboration. ATLAS Technical Proposal for a General-Purpose pp Experiment at the Large Hadron Collider at CERN. Technical report, CERN, December 1994.

[36] M Bettinelli, L Carminati, M Consonni, and F Tartarelli. Analysis of the inclusive $H \rightarrow \gamma\gamma$ channel with DC1 samples. Technical Report ATL-PHYS-PUB-2006-016. ATL-COM-PHYS-2005-056, CERN, Geneva, Sep 2005.

[37] https://twiki.cern.ch/twiki/bin/view/Atlas/EventFilter.

[38] Dan Green. *High $P_T$ Physics at Hadron Colliders*. Cambridge University Press, 2005.

[39] ATLAS Collaboration. Cross-sections, Monte Carlo simulations and systematic uncertainties. Technical Report ATL-COM-PHYS-2008-194, CERN, Geneva, Oct 2008. This is a CSC note - an introductory one containing general features.

[40] Vincent Tisserand ATLAS Collaboration. The Higgs to two photon decay in the ATLAS detector. *ATLAS Internal Note*, July 1996.

[41] John F. Gunion, Howard E. Haber, Gordon Kane, Sally Dawson. *The Higgs Hunter's Guide*. Perseus Publishing, 1990.

[42] ATLAS Collaboration. Expected Performance of the ATLAS Experiment, Detector, Trigger and Physics - Electron/Photon CSC Chapter. CERN-OPEN-2008-020, Geneva, 2008, to appear.

[43] ATLAS Collaboration. ATLAS detector and physics performance, Technical Design Report. Technical Report Volume II, ATLAS TDR 15, CERN/LHCC 99-15, May 1999.

[44] H. Baer et al. Les Houches Guidebook to Monte Carlo Generators for Hadron Collider Physics. *arXiv:hep-ph/0403045v1*, 2004.

[45] Torbjörn Sjöstrand, Patrik Edén, Christer Friberg, Leif Lönnblad, Gabriela Miu, Stephen Mrenna, Emanuel Norrbin. High-Energy-Physics Event Generation with PYTHIA 6.1. October 2000. http://home.thep.lu.se/~torbjorn/Pythia.html.

[46] M.L. Mangano, M. Moretti, F. Piccinini, R. Pittau, A.D. Polosa. ALPGEN, a generator for hard multiparton processes in hadronic collisions. May 2003. http://mlm.home.cern.ch/mlm/alpgen/.

[47] T. Stelzer and W. F. Long. Automatic Generation of Tree Level Helicity Amplitudes. arXiv:hep-ph/9401258, January 1994. http://madgraph.physics.uiuc.edu.

[48] Geant4 Collaboration. G4–a simulation toolkit. Nuclear Instruments and Methods in Physics Research Section A: Accelerators, Spectrometers, Detectors and Associated Equipment, 2003.

[49] Geant4 developments and applications. IEEE Transactions on Nuclear Science, 2006. 53 No. 1 (2006) 270-278.

[50] The ATLAS Metadata Interface Portal Page. http://ami.in2p3.fr/opencms/opencms/AMI/www/.